UNIVERSITY OF CAPE TOWN
IYUNIVESITHI YASEKAPA • UNIVERSITEIT VAN KAAPSTAD

Department of Mechanical Engineering

BLAST IMPACT & SURVIVABILITY RESEARCH UNIT

BISRU

Study of a simplified bumper system subjected to offset impact loading

Christiaan Jan Opperman

2012

Thesis presented for the degree of Masters of Science in Mechanical Engineering in the Department of Mechanical Engineering, University of Cape Town

Declaration

I, Christiaan Jan Opperman, hereby declare that:

> *I know the meaning of plagiarism and declare that all the work in the document, save for that which is properly acknowledged, is my own.*

_____

CJ Opperman

Abstract

In the last few decades there has been increased focus on the design and improvement of energy absorbers, particularly in the field of crashworthiness. These energy absorbers are aimed to absorb the energy of an impact in a predictable and controlled manner and thereby protect the occupants and cargo. More studies have been reported on single energy absorbers in the shape of thin-walled structures than complete systems comprising of several energy absorbing components.

This thesis reports on the behaviour of a simplified bumper system, with regards to energy absorbing characteristics. The simplified bumper system comprises of three components, the crossbeam and two longitudinal members. In the study, several parameters are altered to investigate the change in behaviour of the individual components as well as the bumper system. These parameters of the bumper system include:

- Wall-thickness of the crossbeam (1.0mm to 4.0mm in increments of 0.5mm)
- Two profiles of a crossbeam (straight and curved)
- Two longitudinal member profiles (straight and tapered)

Experiments are carried out to study the behaviour of the bumper system subjected a 40% offset impact loading condition. The dynamic load is applied by dropping the drop masses (301kg, 396kg and 491kg) unto the structure form a drop height of 4m (equivalent kinetic energies of 11.81kJ, 15.5kJ and 19.3kJ respectively).

The results of the experiments are also used to validate a finite element model developed for a numerical parametric study. The simulations are processed using the explicit LS-Dyna R4.2.1 solver using the well-defined and documented material model, Johnson-Cook. The material model incorporates the effects of strain-hardening and strain rates. The bumper system is modelled using a half-symmetry with quadrilateral Belytschko-Lin-Tsay shell elements. In the numerical parametric study, the wall-thickness of the crossbeam is varied from 1.0mm to 4.0mm in increments of 0.5mm with the drop mass kept constant at 500kg. Different profiles for the crossbeam (straight and curved) and longitudinal member (straight and tapered) are investigated.

Four common deformation modes occur in the experiments and are classified as:

- lateral flattening of the crossbeam at impacted end
- progressive buckling of the impacted longitudinal member
- local bending failure of the crossbeam
- plastic hinge formation of longitudinal member-crossbeam at non-impacted end

The results show for an increasing drop mass, there is an increase in crush distance of the longitudinal member at the impacted end. Lateral flattening of the crossbeam is only observed for wall-thickness of 1.6mm and 2.0mm.

In the parametric study the influence of the wall-thickness of the crossbeam is observed to extensively alter the deformation mode, extent of the crush distance and energy absorbing characteristics of the bumper system, in terms of key elements such as peak axial load, initiation of deformation and transient response. The profile variation of the crossbeam is observed to initiate buckling differently and produce dissimilar axial load. The modification of the longitudinal member profiles from straight to tapered show slight improvement in the energy dissipation of the bumper system.

The numerical prediction correlates very well with the experiments for the deformation modes, crush distance and transient response.

Table of Contents

List of Figures

List of Tables

Nomenclature

Acronyms and Abbreviations:

ADAC	Allgemeiner Deutscher Automobil-Club
CCB	Curved Crossbeam
CFS	Critical Failure Strain
EuroNCAP	Euro New Car Assessment Program
NHTSA	National Highway Traffic Safety Administration
ODB	Offset Deformable Barrier
SCB	Straight Crossbeam
SLM	Straight Longitudinal Member
TLM	Tapered Longitudinal Member

Symbols and characters:

A	Yield Stress material model parameter
A_i	Instantaneous area
A_0	Initial area
B	Coefficient of strain hardening material model parameter
B_m	Bending moment
C	Strain-rate hardening coefficient material model parameter
E	Young's Modulus
ε	Engineering strain
ε^*	Normalized strain-rate
ε_p	Equivalent plastic strain

ε_{eng}^{pl}	Engineering plastic strain
ε_{ln}^{pl}	Logarithmic plastic strain
F	Force
ΔL	Crosshead displacement
L_i	Instantaneous gauge length
L_0	Initial gauge length
m	Thermal softening exponent material model parameter
n	Strain hardening exponent material model parameter
σ_{eng}	Engineering stress
σ_f	Equivalent Flow Stress
σ_{true}	True stress
T	Absolute temperature
T^*	Homologous temperature
T_M	Melting temperature
T_R	Reference temperature

Acknowledgements

The author wishes to thank several members of the Blast Impact and Survivability Research Unit (BISRU), at the Department of Mechanical Engineering of the University of Cape Town, for their continual support and assistance. Special thanks go to the following members:

- Dr S. Chung Kim Yuen for his patience during testing, continual discussion and special support in completing this thesis. Many thanks to him, my supervisor.
- Prof G. N. Nurick for his guidance, general discussion and being allowed to study at this esteemed research lab.
- Mr C. Geretto for his assistance with the initial training of LS-Dyna and sacrificing many of the servers for my simulations.
- Mr R. Govender for his constructive and general guidance and providing support with the Split Hopkinson Pressure Bar testing and data processing.
- Mr E. Pickering for his general discussion and humorous chit-chat.
- Mr G. Newins for his patience and help with test specimens and test rig component preparation.
- Mr D.B. Percival for his continued support.

The author's thanks and acknowledgement also goes to the financial support provided by Blast Impact and Survivability Research Unit (BISRU), National Research Foundation of South Africa (NRF) and Armaments Corporation of South Africa (ARMSCOR).

Many thanks to all.

1. Introduction

1.1. Automotive passive safety

Crashworthiness investigation in the automotive industry has been of particular interest in the last few decades. Since the establishment of several programmes, there has been an increase in investment from automotive firms to meet the requirements of the standardized crash tests. Three recognised programmes are:

- EuroNCAP (*Euro New Car Assessment Program*) [1]
- ADAC (*Allgemeiner Deutscher Automobil-Club*) [2]
- NHTSA (*National Highway Traffic Safety Administration*) [3]

Automotive passive safety can be divided into three regions, that are:

i. Rigid passenger safety cell
ii. Energy absorbing systems
iii. Supplemental restraint systems

The effective combination and design of these three regions results in a crashworthy vehicle, providing adequate protection for the occupants. The passenger safety cell surrounds the occupants and is designed with focus on high strength and rigidity, while minimising compartment intrusion and prohibiting the collapse of the vehicle frame to increase the survival zone of the passengers. The current Volvo S60 safety cell shown in Figure 1.1 is predominately constructed from metal with yield strength of at least 800MPa. Surrounding the rigid passenger safety cell are energy absorbing systems; these generally consist of thin-walled structures designed to absorb the kinetic energy during an impact. Energy absorbing systems can consist of beams, crash boxes and elongated tubular members. Extensive investigation has been conducted on the deformation modes of thin-walled structures and will be discussed in the Chapter 2. Supplemental restraint systems (SRS) are in place to reduce the force exerted directly on the occupants in a safe, controlled manner. On standard vehicles these systems consist of seatbelts, pretensioners and force-limiters for the seatbelts, various airbags and interior components designed to collapse under impact.

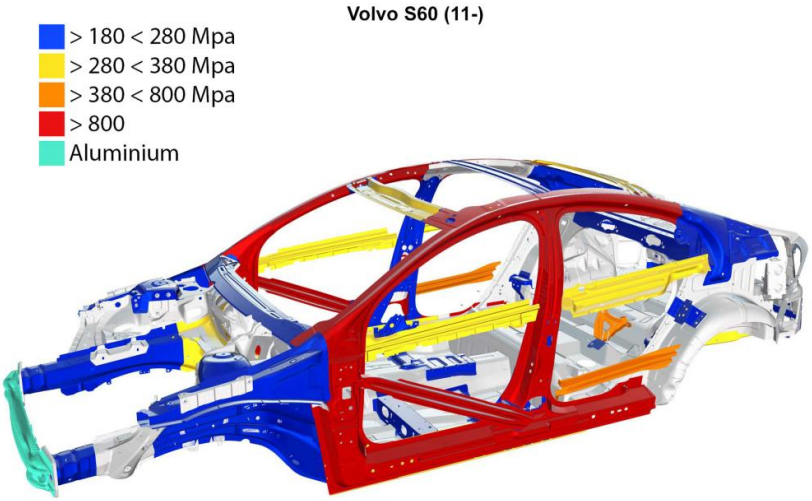

Figure 1.1: Design of Volvo S60 chassis frame [4]

1.2. Automotive offset impact scenario

In the developing world, car production and congestion is on the increase resulting in an increase of transport accidents in various forms, from minor crash with little structural damage to more serious impact involving life changing injuries and loss of life. Frank and Gruber [5] stated that the majority, about 48.1%, of real-world severe accidents occur in an offset impact situation and also account for the highest portion of fatalities. Stucki and Hollowel [6] presented an analysis of crash data, from the USA market, using the National Automotive Sampling System (NASS) and the Fatality Analysis Reporting System (FARS). The data is grouped into four 'general' test conditions: full barrier, left and right offset, and other impact modes. Injuries are bucketed on two levels: moderate and more severe injuries (MAIS 2) and serious and higher injuries (MAIS 3).

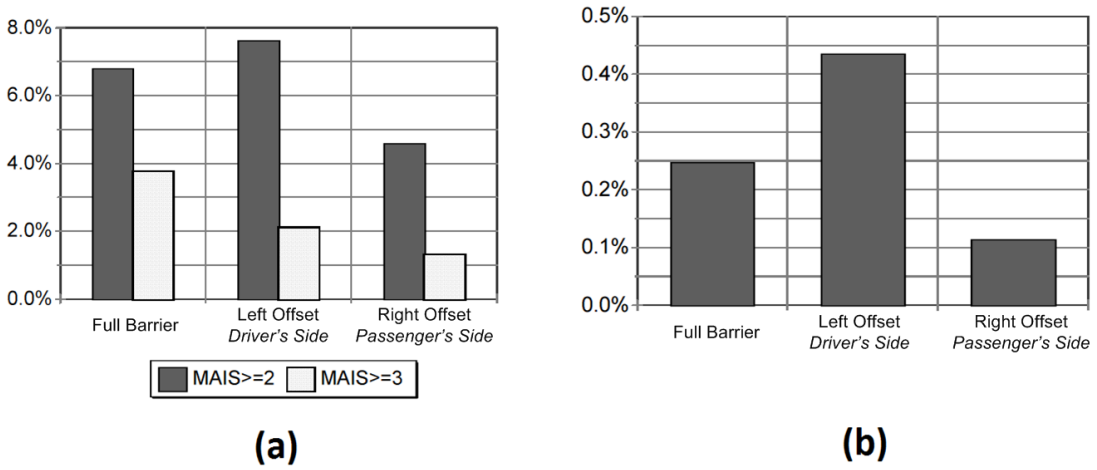

Figure 1.2: Injury risk (a) and fatality risk (b) by test condition [6]

The results, shown in Figure 1.2, indicate that the risk for moderate injury (MAIS) is slightly higher from vehicle crash data associated with left offset, i.e. driver's side, than the full barrier (7.6% and 6.8% respectively) whereas the risk for serious injury (MAIS 3) is the highest for full barrier (3.8%). The left and right offset groups have a lower serious injury risk rate of 2.1% and 1.3%. The fatality rates were based on limited observations; however the left offset, i.e. driver side, had a much higher risk of fatality (0.43%) than the full barrier condition (0.25%). From the crash data that represents actual crash configurations, the left offset condition showed the highest frequency and risk of 'serious to fatal injury' [6].

EuroNCAP [1] is an independent assessment program dedicated to provide motoring consumers with realistic safety performance on the most popular cars sold in Europe. Established in 1997, they have continuously evaluated and adapted their testing procedures and protocols, and over the years have implemented improved assessments, such as the whiplash test introduced in January 2009 [1]. The frontal impact crash procedure is based on the method developed by European Enhanced Vehicle-safety Committee, according to legislation. The test procedure involves the vehicle being propelled at 64km/h (40mph) into a deformable barrier at a 40% overlap with relation to the widest part of the vehicle, as illustrated in Figure 1.3.

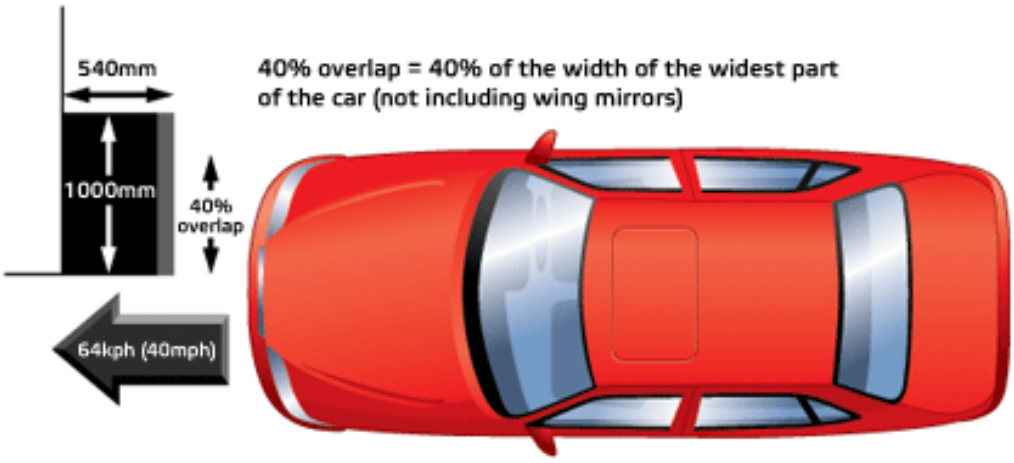

Figure 1.3: EuroNCAP frontal impact test procedure [1]

The deformable barrier is a honeycomb structure mounted to a rigid barrier with dimensions of 1000mm x 540mm. In an ODB (*Offset Deformable Barrier*) test the barrier absorbs some of the energy, depending on the vehicle structure and interaction with the honeycomb face [7].

As offset impact scenarios are considered the highest risk, with respect to fatalities and probability, they are the primary focus in frontal impact tests from independent assessment programmes. The investigation into the impact scenario is essential for further understanding and improvement of energy absorbing systems.

1.3. Thin-walled structures

The use of thin-walled structures is evident in many designs and constructions; where common application is in structural components of sea, land and air transport vehicles [8]. These structures consist of common shapes which include circular tubes, square tubes, fustra, struts, honeycombs, and sandwich plates. Due to the economic benefits and ease of implementation thin-walled structures are used as the energy absorbers in automotive passive safety design.

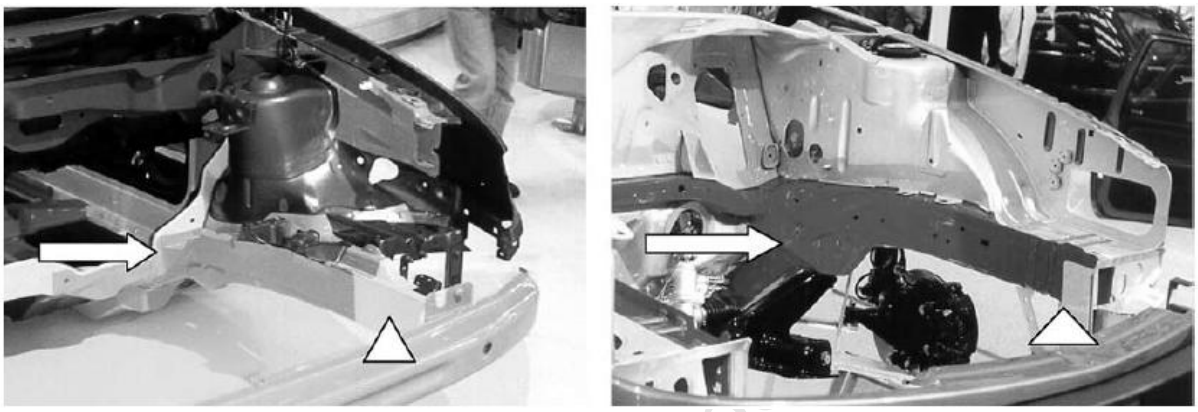

Figure 1.4: Energy absorbing structures in the front of an automobile. Arrow indicates 'S' frame and triangle indicates crash-box [8]

The controlled manner of the dissipation of kinetic energy is a key issue in the determination of the crashworthiness of a vehicle. Automotive safety regulations opened a new, demanding area of engineering analysis in the early 1960's that required thin-walled structures be designed to sustain abnormal loads - apart from the previously stipulated regulations focusing only on standard operating loading conditions [8]. Since then, many investigations into the field of structural crashworthiness have been undertaken and, consequently, several journal sources were founded. Examples of journals founded are *The International Journal of Mechanical Science* commenced publication in 1960, *The International Journal of Impact Engineering* founded in 1983, the journal of *Thin-Walled Structures* in 1983 and *The International Journal of Crashworthiness* in 1996. Alexander [9], Pugsley and Macaulay [10] were some of the first authors to investigate the deformation of circular tubes, in 1960. Abramowicz and Jones [11-14] investigated and overviewed the crush behaviour of mild steel circular and square tubes under quasi-static and dynamic axial loading conditions.

1.4. Thesis objectives and outline

This thesis presents the results of a study on one of the key energy absorbing structures in a vehicle: the bumper system both experimentally and numerically. The purpose of this investigation is to ascertain the influence of changing parameters on the behaviour of the simplified bumper system, shown in Figure 1.5, with focus on energy absorbing characteristics. The objectives of this thesis are to:

(1) Design and construct a simplified bumper system to be tested experimentally with different parameters (wall-thickness of crossbeam of 1.6mm, 2.0mm and 3.0mm respectively) to validate and calibrate a finite element model.
(2) Develop a numerical model to replicate a simplified bumper system.
(3) Compare the results to the numerical simulations with experiments in terms of the crush distances, deformation modes and transient response for validation.
(4) Numerically perform a parametric study to investigate the influence of the wall-thickness of the crossbeam and two distinct profiles the crossbeams (straight and curved) and longitudinal members (straight and tapered) respectively.
(5) Draw conclusions and recommendations based on the findings.

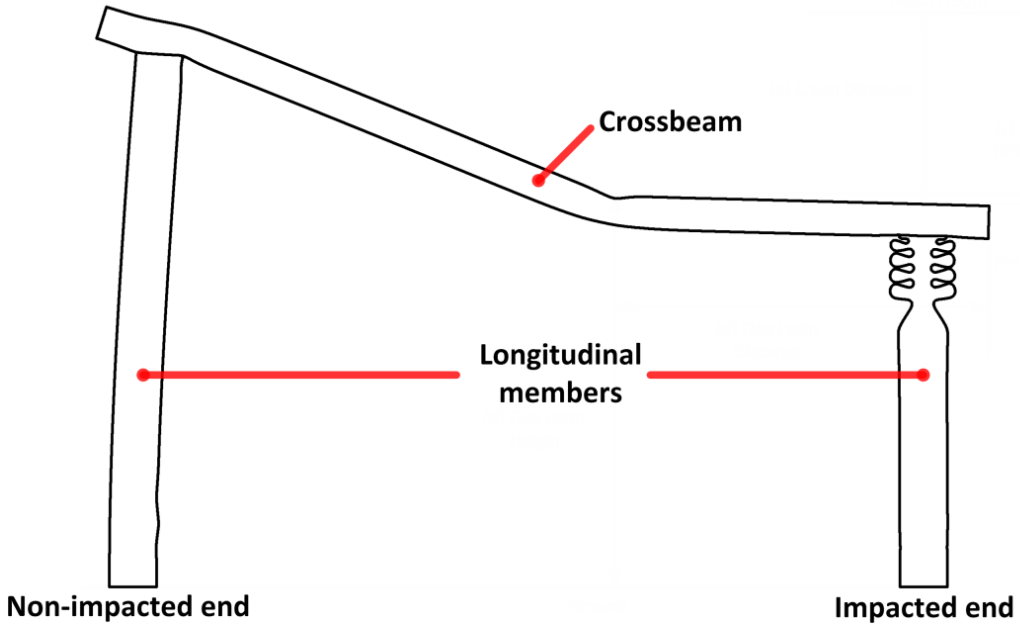

Figure 1.5: Schematic of a deformed simplified bumper system

A brief literature review on the deformation modes in bumper system studies is reported in Chapter 2. The experiments including the design and layout of the simplified bumper system are described with results in Chapter 3. The finite element model used is discussed thoroughly in Chapter 4 from the selection of material model parameters, contact algorithms and boundary conditions to the validation of the model. Chapter 5 lays out the numerical parametric study; including the setup and results. The results such as

deformation modes, energy absorbed, crush distances and axial force measurements are discussed and compared within the framework of the study. A discussion of the parametric study and an analysis of the behaviour mechanics of the simplified bumper system are elaborated in Chapter 6. Conclusions are drawn up and recommendations are proposed in Chapters 7 and 8 respectively.

2. Literature Review on Energy Absorbers

Energy absorbers are implemented, within context of this study, to transform the kinetic energy of an impact into other forms; predominately elastic and plastic deformation and slight heat and sound energy. Energy absorbers are designed to reduce the forces exerted on the occupants of the vehicle and promote the distribution of the impact energy around the passenger cell.

2.1. Structural impact mechanics

The mechanics of an impact depend on different influencing factors such as the impacting mass, striking velocity, material properties and geometry of components. The response of thin-walled structures differ greatly depending on the loading condition. Under quasi-static conditions the inertia effects (axial, lateral and radial) do not play a significant role in the behavioural response of the structure because the load is applied sufficiently slow. For dynamic loading, inertia effects and strain rate effects [15] influence the response of the structure. Structural inertia effects become more significant with increase in impact velocity, impact mass and strain rate effects of the material. The properties of some materials are observed to also vary with varying impact velocities as a result of *strain rate sensitivity* where the Yield Stress and Flow Stress of the material is sensitive to the strain rate being experienced [15]. Commonly for carbon based steel the Yield Stress and Ultimate Stress of the material tend to increase with increase in strain rates. This relates to an increase in the peak forces requirement of carbon based steel to fail, altering the deformation response of the structure especially at high impact velocities.

2.2 Modes of deformation

The deformation of thin-walled metallic structures is generally classified in the four modes of failure [16]:

1. Axial crushing
2. Axial Splitting
3. Lateral indentation
4. Lateral flattening
5. Axial Inversion

In the deformation characteristics of a bumper system, only several deformation modes that are common and are discussed in sections 2.2.1 to 2.2.3.

2.2.1 Axial crushing

Axial crushing of thin-walled structures is one of the more favoured failure modes since it has a comparatively high energy absorbing capacity and a good degree of repeatability under a widespread of loading conditions. Loading in the axial direction brings about several modes failure that depends greatly on geometric relations, impact velocities, impact mass, material properties and structural defects. These can be classified as:

i. Euler buckling
ii. Progressive buckling
iii. Dynamic progressive buckling

2.2.1.1 Euler buckling

Euler buckling, also termed global buckling, resembles the bending collapse of a long beam about a plastic hinge formed along the length. The mode is predominately dependent on certain geometric ratios and if an adequate axial compressive force is applied. Only local deformation occurs at the plastic hinge resulting in comparatively low energy absorption. An initial peak load is observed as a result of the formation of the plastic hinge and thereafter the load profile decays to a low, relatively constant force as the tube flexes around the plastic hinge. Thin-walled structures comprising of long and slender shells or tubes tend to buckle globally. A square tube that has failed in Euler buckling mode is shown in Figure 2.1. The specific square tube has a length-to-width ratio of 8 and a wall-thickness-to-width ratio of 0.006 [17]. These geometric ratios resulted in the preference of this mode of failure. Owing to the low energy capacity; the Euler buckling mode is seen as an undesirable crushing failure mode.

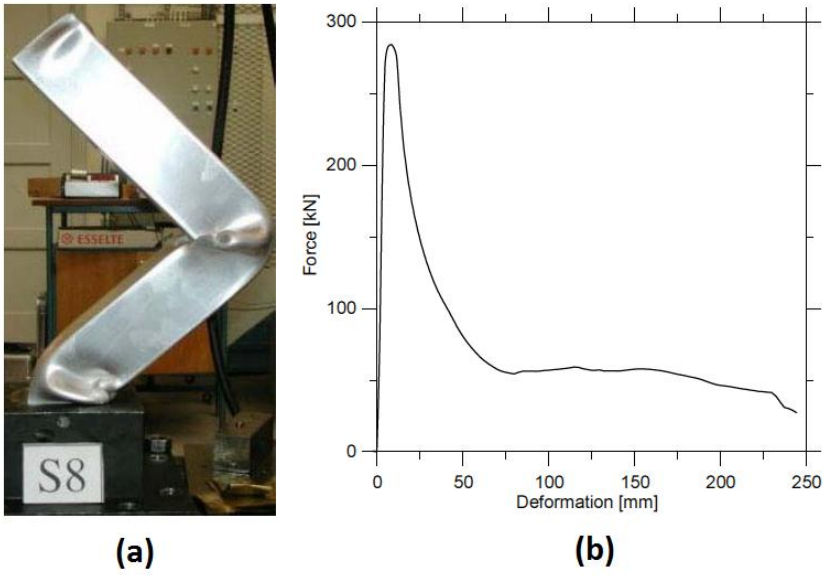

Figure 2.1: Illustration of a (a) square tube under Euler buckling mode and the (b) axial load-displacement profile [17]

2.2.1.2 Progressive buckling

The progressive buckling mode is distinct as repetitive lobes/buckles are formed longitudinally if a sufficient axial compressive force is continuously applied. The key aspect is that the thin-walled member remains predominately along the vertical axis during deformation not invoking mixed mode deformation. Circular, rectangular and square cross-sectioned tubes display variations of the progressive buckling mode with respect to lobe shapes and failure modes. Andrews *et al.*[18] classified the axial crushing of cylindrical tubes under quasi-static loading conditions into seven different categories based on their experimental observations. Abramowicz and Jones [11, 12] classified the progressive buckling of circular and square tubes into the following modes:

- **Cylindrical tubes:**
  1. Concertina Mode
  2. Diamond Mode
- **Square tubes:**
  5. Symmetric Mode
  6. Asymmetric Mode A
  7. Asymmetric Mode B
  8. Extensional Mode

The axial-load vs. displacement profile of progressive buckling mode has a general oscillatory trend. An initial high peak force is observed at the formation of the first lobe overcoming the yield strength of the material. The lobe is a plastic hinge where the walls of the tube fold around and extend at the hinges [19]. Thereafter a repetitive pattern is observed with the formation of consecutive lobes. The axial-load profile show regular oscillations about a mean force as shown in Figure 2.2.

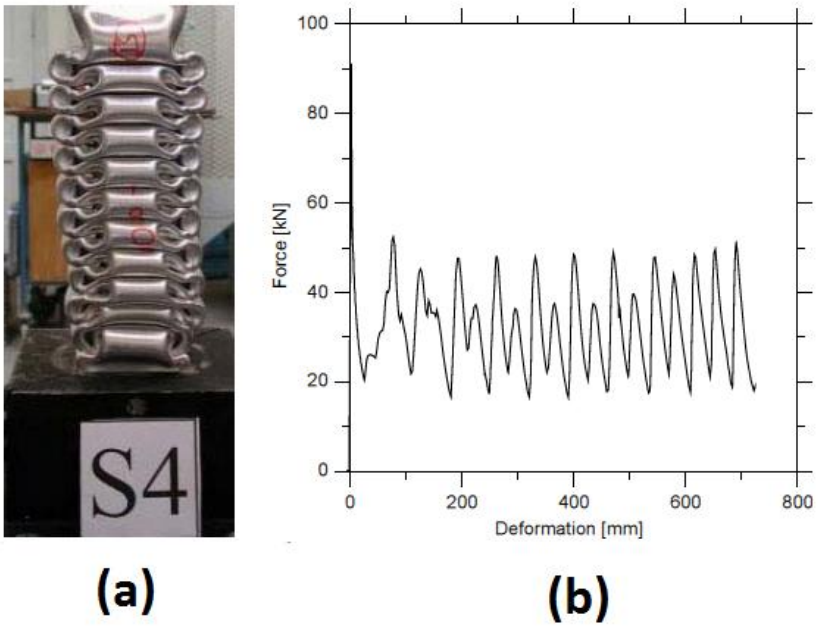

Figure 2.2: Illustration of progressive buckling mode (a) of a final deformed square tube and (b) the axial-force deformation profile

As there is more deformation of material from multiple lobe formation than that of other modes such as Euler Buckling, the energy absorbing capacity of the progressive buckling mode is regarded as favourable. In comparison to other deformation modes, progressive buckling has high energy absorption and stroke length per unit mass. For example, the specific energy absorbing capacity of a tube is 10 times greater undergoing progressive buckling compared to lateral compression. This attribute accounts for the frequent use of tubes designed to deform in this manner in energy absorbing systems.

2.2.1.1 Transition from progressive to Euler buckling

Extensive investigation has also been undertaken to formulate and understand the transition between Euler and progressive buckling by Andrews *et al.*[18], Abramowicz and Jones [20] and other authors [21-23]. It was observed that the transition between the two distinct modes depends on geometry, boundary conditions and the material of the thin-walled structure; these include length, cross-section, strain rate and strain-hardening. Abramowicz and Jones [20] also reported that Euler buckling may or may not coincide with the maximum load-carrying capacity of the structure.

The transition under dynamic impact loading conditions has been investigated experimentally [20, 22, 23] and numerically [24, 25] for circular and square tubes; subjected to axial impacts with initial velocities up to 20m/s. It was shown that the critical tube length has a tendency to increase with increase in impact velocity, although under certain conditions the counter-intuitive is observed and no distinct critical length could be defined. Jensen *et al.*[22] performed a numerical study of the dynamic buckling transition of aluminium alloy square tubes and noted that the critical tube length varied depending on the width-to-thickness ratio and impact velocity. Karagiozova and Alves [24] established the major parameters that govern the dynamic buckling transition of aluminium alloy circular tubes. The experimental study showed that the impact velocity, i.e. inertia effects, is a key influential factor. The material characteristics are shown to be a parameter as well, especially the material hardening characteristics. Karagiozova and Jones [26] further investigated the transition under dynamic impact loadings and remarked that the transition is dependent on multi-dimensional space parameters and simple curve-fit dependence is not plausible. Their study did show that dynamic buckling transition is not a random phenomenon. It was demonstrated that the variation of each known parameter did influence the tube response in a predictable manner. The suggestion of a trigger (geometric imperfection or altering material properties strategically) could promote the initiation of progressive buckling. It was shown that at large impact energy the initiated progressive buckling later changes to global bending, producing a mixed buckling mode.

2.2.2 Lateral flattening

Lateral flattening is described as the compression of a tube longitudinally between rigid platens. An experimental sample of a three-tube system undergoing lateral flattening is shown in Figure 2.3. Olabi *et al.*[16] distinguished that 3 analytical theories that have been formulated. The first theory, termed 'Limit Analysis', was carried out by DeRuntz and Hodge [27] for the flattening of mild steel tubes under quasi-static lateral loading to observe the failure response. A rigid perfectly-plastic material model was used to predict the load-deformation response and a geometrical component of stiffening is implemented into a theoretical model. The omission of material strain hardening show an under-estimation of the actual load-displacement response. The second theory, termed 'Plastic Theory', by Reid and Reddy [28] further examined the effects of strain hardening under dynamic loading conditions. The theoretical model produced is based on a rigid linear strain hardening material model and is the most accurate to date; according to Olabi *et al.* [16]. Sherbourne and Lu [29] used the proposed model, third theory termed 'Moving Hinge Method' introduced additional boundary conditions, to analyse theoretically the lateral flattening of tubes under rigid platens. The model is based on a rigid-perfectly plastic material model and an attempt was made to include strain hardening. The resulted model did show a good agreement with the experimental data.

Figure 2.3: Initial and final stages of lateral flattening of three-tube system [30]

2.2.3 Lateral Indentation

The application of a point load centrally on the lateral side of a tube, i.e. transverse loading, produces local denting that progress into global buckling of the whole tube; shown in Figure 2.4. Sowerby *et al.* [31] are one of the first to analyse the diametric compression of circular rings by point loads. Watson *et al.*[32] studied the local loadings of tubes laterally to investigate an automobile bumper. It was observed that a method of energy calculation that correlated agreeably with the experimental data. Johnson and Walton [33, 34] investigated 10 different automobile bumpers and experimentally determined the load-deflection curves. The results show that the investigated bumpers can withstand a maximum impact velocity of 10km/h. Jing and Barton [35] investigated the response of square tubes under quasi-static and dynamic lateral loading focusing on the collapse mechanisms and the relationship between energy absorption and deflection. Little difference between the modes of deformation of tubes tested quasi-statically and dynamically was observed. The results suggest that the energy absorption capacities could be predicted using quasi-static methods.

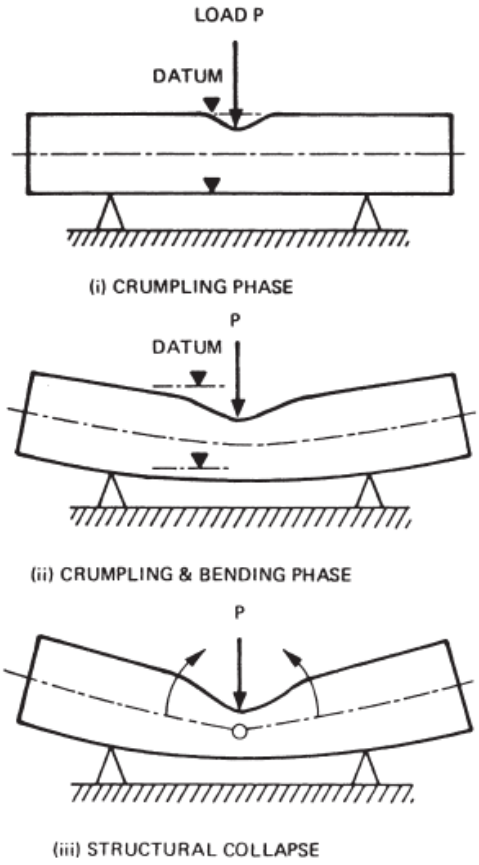

Figure 2.4: Lateral indentation of simply supported beam [34]

2.3 Buckling initiators

The inclusion of buckling initiators, also termed triggers, may change the behaviour of a thin-walled structure when undergoing impact loading conditions. The thin-walled structures could include buckling initiators such as imperfections, variation in material composition, fillers and pre-existing deformation to initiate a different response in the structure [36]. The use of initiators define the location of deformation initiation and the mode by constructing a weak or high stress concentration region. The resulting benefits are, for example, a desired form of deformation mode, reduction in peak loads experienced or a required force profile. A sample of axial force results is shown in Figure 2.5 where the inclusion of through-hole discontinuities reduced the initial peak force by up to 35.4kN. In Figure 2.5 the inclusion of 2 pairs of holes (A4_d25) with diameter decreased the peak force to 110.6kN; the test with 3 pairs of holes (A6_d25) decreased the peak force to 104.5kN and the test with 4 pairs of holes (A8_d25) reduced the peak force to 104.6kN. In all cases the inclusion of through-hole discontinuities reduced the initial peak force.

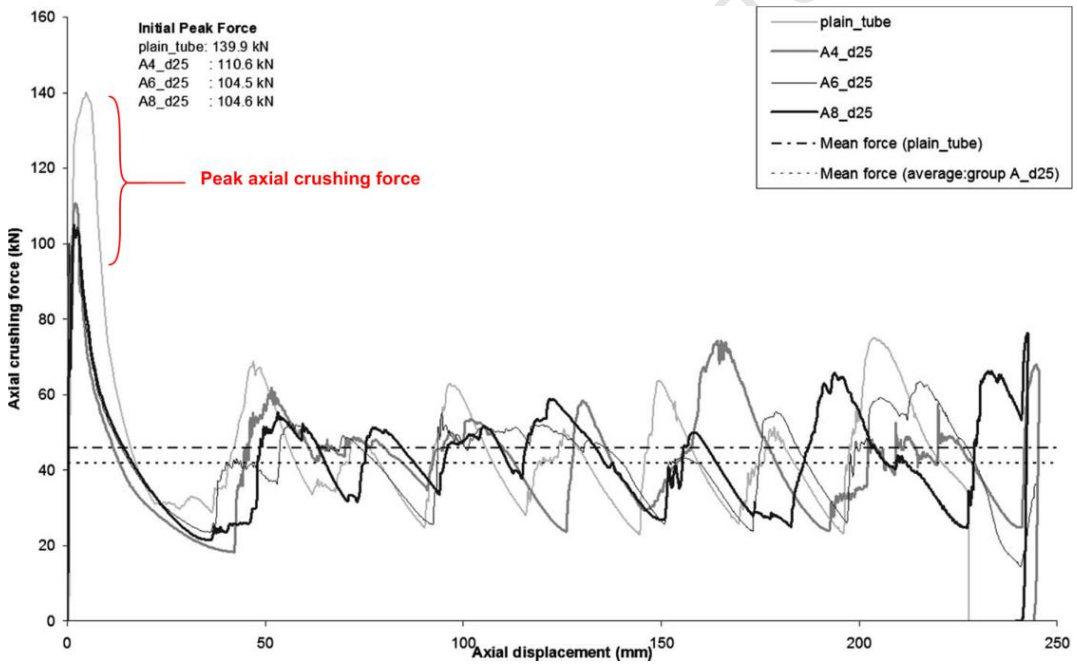

Figure 2.5: Axial crushing force vs axial displacement profiles of plain tube and tubes with several pairs of through-hole discontinuities [37]

2.4 Bumper system investigations

Thin-walled structures are extensively used in the application of Automotive Passive Safety in the form of energy absorbers and structural members; where the modes of deformation can be selected and designed. It is therefore of particular interest to investigate the behaviour of the individual components; and likewise their influence in a complete system. As the system may be exposed to asymmetrical load conditions and produce additional lateral and/or bending loads through the components; the response of the individual energy absorbers may differ from their independent behaviour.

A typical bumper system, in a conventional automobile shown in Figure 2.6, consists of a lateral crossbeam *(blue)*, two main longitudinal members *(grey)* and crash-boxes *(green)* connecting them. One of the main purposes of the bumper system is to provide adequate absorption of kinetic energy during a crash to minimise the load transferred to the subsequent passenger cell.

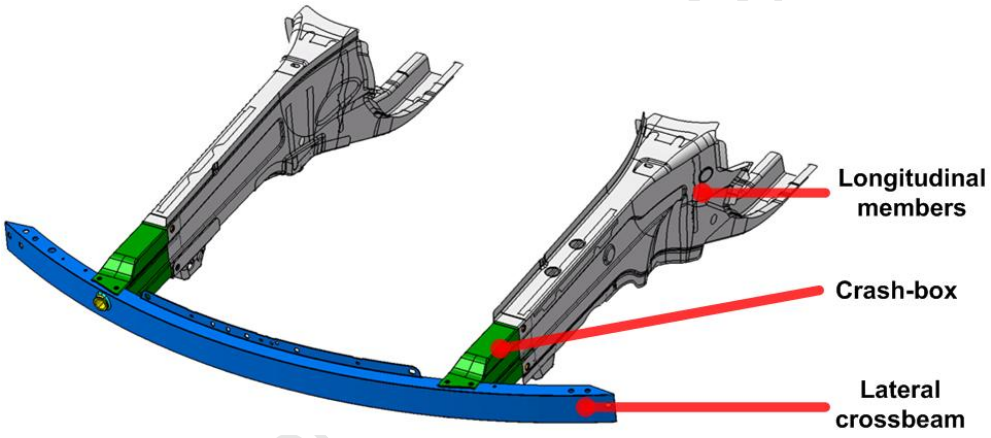

Figure 2.6: Bumper system of the Mercedes-Benz C-Class with inserted crash-boxes [38]

The majority of early bumper investigations [39] - [40] focus on the structural performance at low-velocity impact, local damage and material variation. Studies on more comprehensive bumper systems subjected to severe dynamic impact scenarios appear to be minimal and diverse with their primary objectives. Choen *et al.* [41] reported on a new composite bumper made from glass fabric epoxy with two end pads illustrated in Figure 2.7. The pads are designed to impact the front tyres of the car after the brackets collapse during a collision. The end pads have a tapered section to absorb energy by progressive buckling and improve the energy absorption characteristics. Their optimal cross-sectional dimension and thickness of the composite bumper beam were determined to be 40mm x 40mm and 5.4mm thick. The static bending test conducted revealed that the composite bumper prototype weighed 30% less than the equivalent steel bumper beam without sacrificing on the static bending strength.

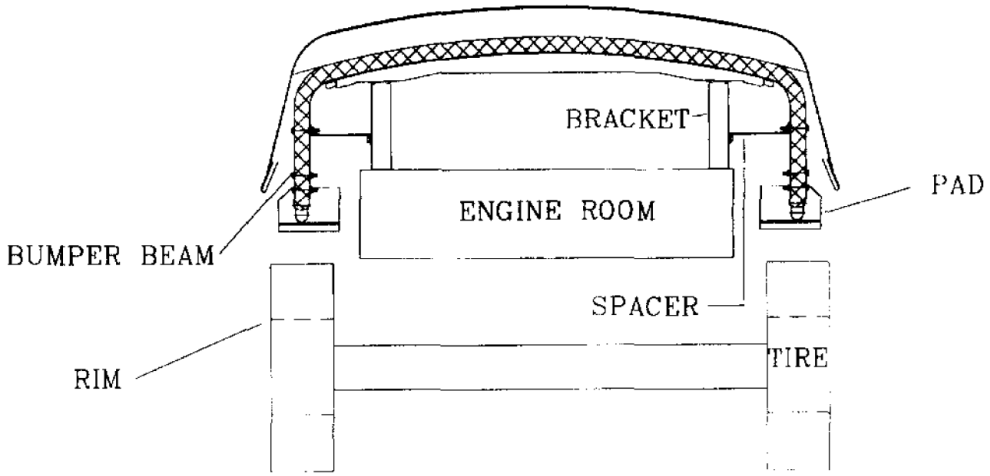

Figure 2.7: Configuration of the bumper beam with two pads [41]

Hosseinzadeh *et al.* [40] further studied automotive composite bumper beams subjected to low-velocity impacts with focus on low damage. Three main design factors for the structure were studied: shape, material and impact conditions. A commercial bumper manufactured from *Glass Mat Thermoplastic* (GMT) was primarily studied and characterised by impact modelling using LS-DYNA ANSYS 5.7. The results were compared with conventional materials steel and aluminium. The aforementioned factors were characterised and a high strength *Sheet Metal Composite* (SMC) was later proposed. Figure 2.8 shows the impact layout of the composite bumper beam.

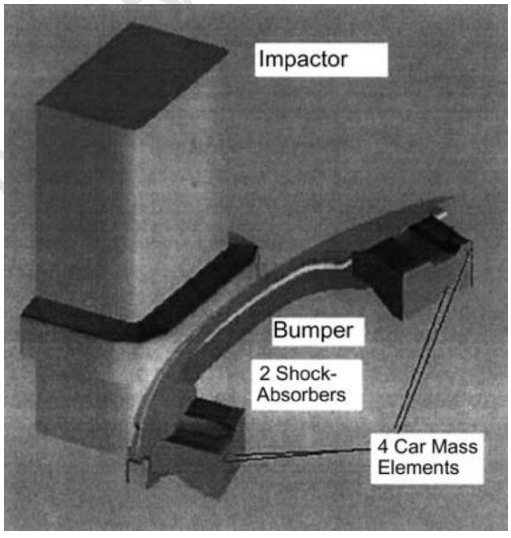

Figure 2.8: Impact layout of composite bumper beams subjected to low-velocity impact [40]

The impactor, mass of 1100kg, travelled at 4km/h and impacted the bumper beam perpendicularly. The car mass elements had a total mass of 1500kg. *The* shock absorbers were semi-cubic *Plastic Polypropylene* (PEP) holders of thickness 4mm. The bumper beams consisted of steel, aluminium, GMT and SMC; with a thickness of 2.5mm for the SMC and

3.5mm for the other material. The GMT bumper beam was strengthened by ribs in special areas to form a more rigid and stable structure. The metal bumper beams failed during the test (past elastic range) and had a weight increase of 500% and 100% for steel and aluminium in comparison to the GMT selection. Certain nodal regions in the SMC bumper beam were further strengthened with an increase in thickness to 4mm to prevent failure. The maximum deflections observed ranged in 30-55mm. The conclusion drawn is that the SMC material selection with the modified thicknesses in certain areas proved the most suitable proposal to meet the three characterization factors.

Simon and Beggs [42] carried out a comparative numerical study of a dual-phase steel and aluminium alloy bumper bar system. The impact is conducted into a central rigid pole of 180mm diameter at 16km/h towards the centre of the bumper bar; shown in Figure 2.9. Severe bending of the bar beam was observed with induced bending moments on the connected crash cans due to the beam end rotation. The equivalent mass comparison between the steel and aluminium, by adjusting the wall-thickness to 1.37mm and 4.0mm respectively, was a focal point of the investigation. The system consisted of a simple 1100mm rectangular cross section bumper bar beam made from dual-phase steel (DP600) or two aluminium alloys (Al6061T6 and Al7108T6) connected by two bolts to two 130mm long crash cans with 3 buckling initiators on either side. Rigid rear end plates were attached to the crash can end faces which represent the vehicle's inertia and mass of 1040kg. The equivalent bumper bar system had a consistent mass of 5.75kg throughout the three materials after the adjustment of the wall-thicknesses.

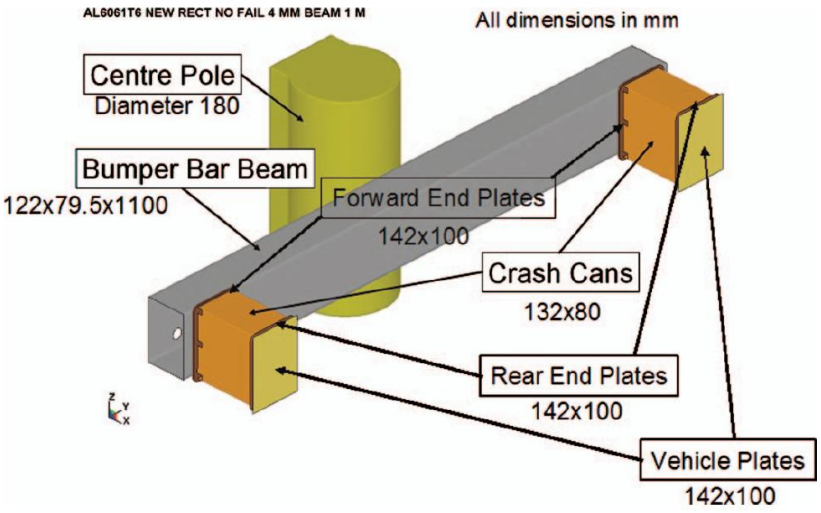

Figure 2.9: FE model setup of simple bumper bar system [42]

A simple material model using isotropic elastic plastic material behaviour was implemented with a simple *critical failure strain* (CFS) criterion varying from zero CFS (*Critical Failure Strain*) to 0.119 (DP600), 0.180 (Al7108T6) and 0.206 (Al6061T6) respectively. The outcome was that the light metal aluminium alloys outperforms the higher-strength steel based on the same weight restriction. The Al70108T6 alloy outperform the Al6061T6 alloy which showed greater energy absorption over a smaller crush distance. The alloy lessened the bending of the bumper bar beam and introduced a greater loading on the *crash cans* that deformed more at an earlier stage.

2.4.1 Crossbeam strengthening

Jenefeldt [43] performed a numerical parametric study focusing on frontal car-to-car impact scenario investigating the effects of strengthening the crossbeam of one of the vehicles. The objective of the study was to investigate how the strength of the crossbeam affects the compatibility potential of the two cars; modified and unmodified. All the simulations were carried out with a Ford Taurus FE-model using the LS-DYNA solver. The output measurements form the simulations included accelerations, compartment intrusions, absorbed energy and the forces. Three accelerometers were placed, one in the A-pillar region, transmission tunnel and one near the rear axle where no deformation is reported.

A total of 135 simulations are carried out at 56km/h for the modified vehicle. The crossbeam strength of the modified vehicle ranged from 50%, 100%, 200%, 400% and 1000% where the yield point was scaled accordingly. The crash test orientation included offset scenarios of 35%, 50% and 65% with rotation of one vehicle of ±15° for further oblique conditions. Certain tests also included ride height differences of ±60mm to further investigate crash compatibility. A set of simulations is shown in Figure 2.10.

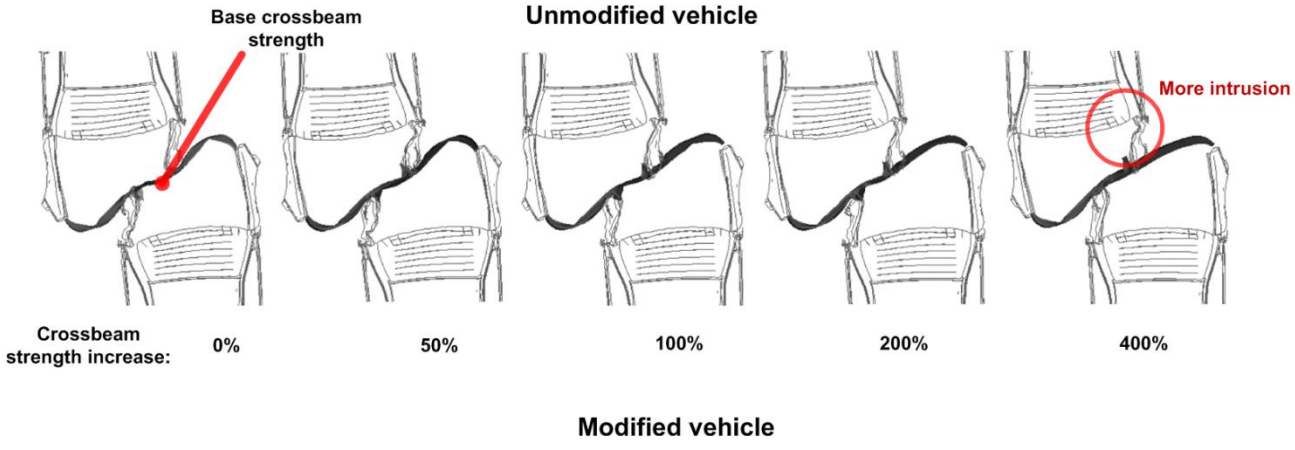

Figure 2.10: Deformation of the five different crossbeam strengths for the 50% overlap and no ride height adjustment (Modified vehicle is at the bottom throughout) [43]

The deformation decreased on the modified crossbeam with increased strength as expected; shown in Figure 2.10. The energy absorption of the strengthened crossbeam tends to increase except for the highest strength modification, i.e. 1000%, since it deformed less than the 400% modified crossbeam. The higher crossbeam strength vehicles forced the opposing unmodified vehicles to absorb a larger part of the kinetic energy. The energy distribution of the two vehicles are shown in Figure 2.11.

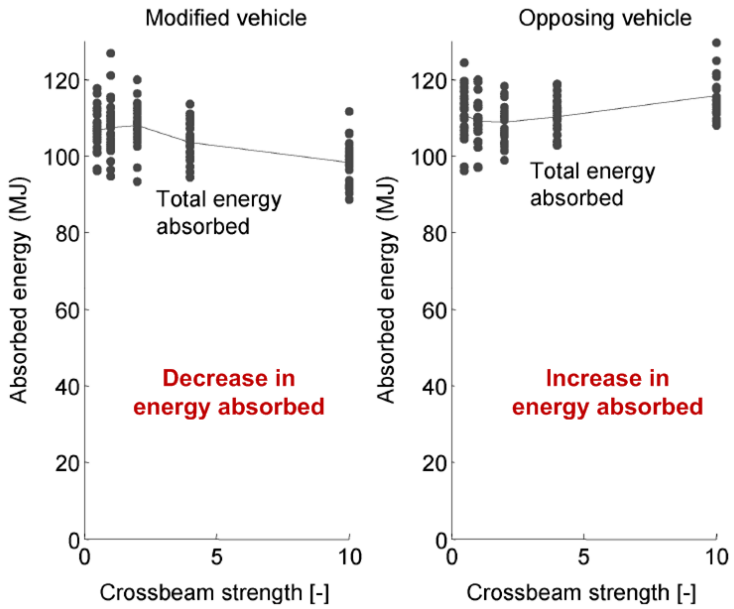

Figure 2.11: Absorbed energy vs. crossbeam strength increase for all simulations of the modified and opposing vehicles [43]

The energy absorbed by the modified crossbeam stagnates after the 400% increase and no more energy was absorbed by the modified vehicle. The modified vehicle total energy absorption peaked at the 200% crossbeam strength at which stage the unmodified vehicle energy absorption increased thereafter. In all test configurations, there was a general increase in compartment intrusion of the unmodified vehicle. The increase in strength of the crossbeam improved the deployment of the restrain systems, since it produces a higher acceleration peak in the early stage of the impact. Overall a compromise was in order to optimise the design goals of compatibility and energy absorption.

2.4.2 Bumper system with tapered members

Nagel [44] investigated experimentally and numerically straight and tapered tubes in a vehicle bumper system as comparable energy absorbers based on the energy absorbing performance. Quasi-static experimental work was carried out to validate the finite element model of the system. The model is later used to analyse the response of the system under quasi-static and dynamic impact loading. Figure 2.12 shows the components in the bumper system.

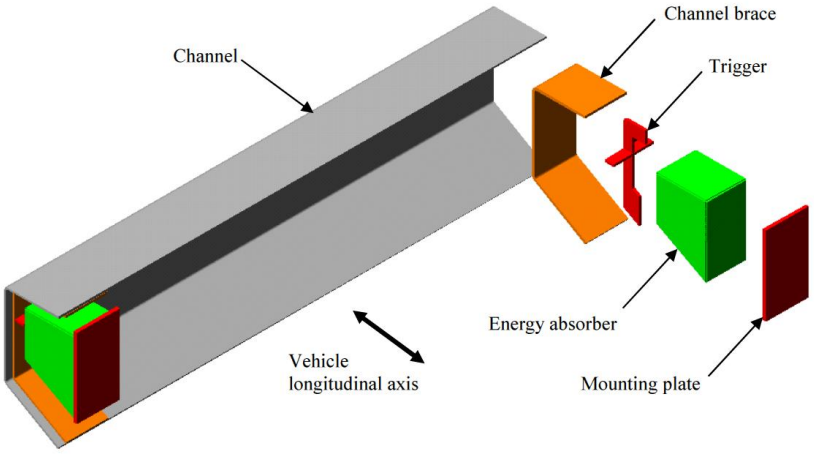

Figure 2.12: Bumper system with tapered rectangular tubes [44]

A trigger component is incorporated to reduce the peak load and to provide a relatively stable load response. All components were made from mild steel with the following thicknesses: 3mm for channel, 4mm for channel brace and trigger, 1.6mm for the energy absorber and 8mm for the mounting plate. The components are welded together using fillet welds. The validation of the FE model involved comparing the load-deflection response of the system and the stresses and strains at various regions of the system where rosette strain gauges are placed, where highest stress levels are expected. For the dynamic simulations the wall-thickness of the energy absorbers are increased to 2mm to improve the maximum energy absorption capacity.

ABAQUS/Explicit version 6.3 is used to perform the modelling with shell elements of type S4R and using the Cowper-Symonds constitutive equation to include strain rate effects under dynamic loading with constants $D=6844s^{-1}$ and $q=3.91$. The welded connections are treated as tied constraints.

The parametric study of the bumper system involved straight and tapered tubes for the energy absorbers at varied oblique loading scenarios. Different impact velocities and masses are investigated, namely 5-20km/h in 5km/h increments and 1000kg, 1500kg and 2000kg. The wall-thickness of the main channel is 3mm or 6mm to observe the change in the response of the bumper system.

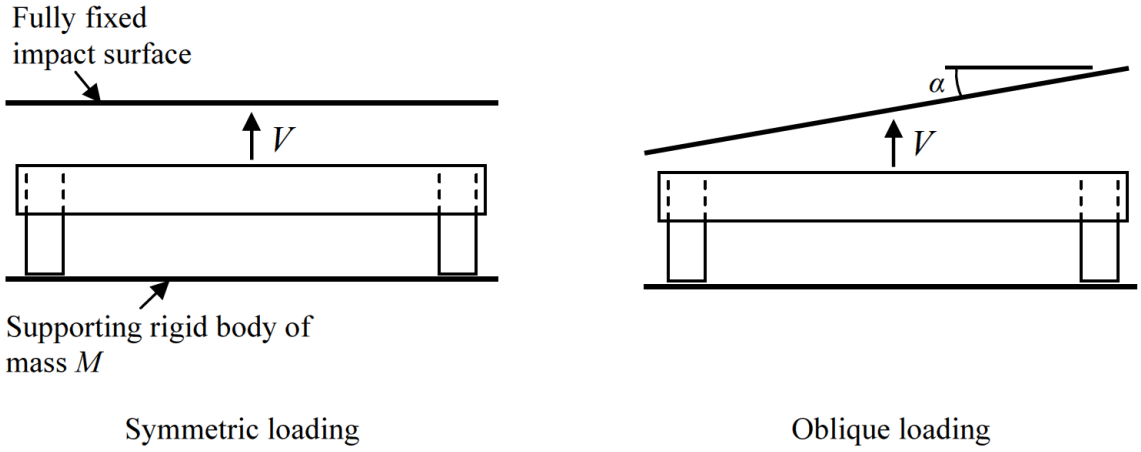

Figure 2.13: Dynamic loading conditions for the bumper system [44]

The angle α of the oblique loading condition varied from 0° to 40° in increments of 5° as illustrated in Figure 2.13. The structural properties of the channel centre become more important under oblique loading conditions as this member effectively becomes the loading path between the two energy absorbers. The mean load up to a given deflection was observed to decrease with an increase in load angle. The selection of straight and tapered tubes did not have a significant difference in response. A critical load angle was identified to be between 30° and 35° where there is a transition from progressive buckling to global bending collapse of the energy absorbers. It was observed that the mean load response on either side of the transition region did not vary between the straight and tapered tubes, which was in contrast to the response of individual tubes under oblique loading. Nevertheless the mean load was observed to be steady over the transition region for the tapered tube as the energy absorber.

The channel wall-thickness had no significant effect on the mean load when either progressive buckling or global bending collapse dominated the response. However, the mean crush load had a lower reduction with the tapered tubes near the critical transition angle. The buckling of the channel was most significant before the critical load angle for transition, angles of 25° and 30°. It is observed that the bumper system with a tapered tube as the energy absorber is less sensitive to the wall-thickness of the channel.

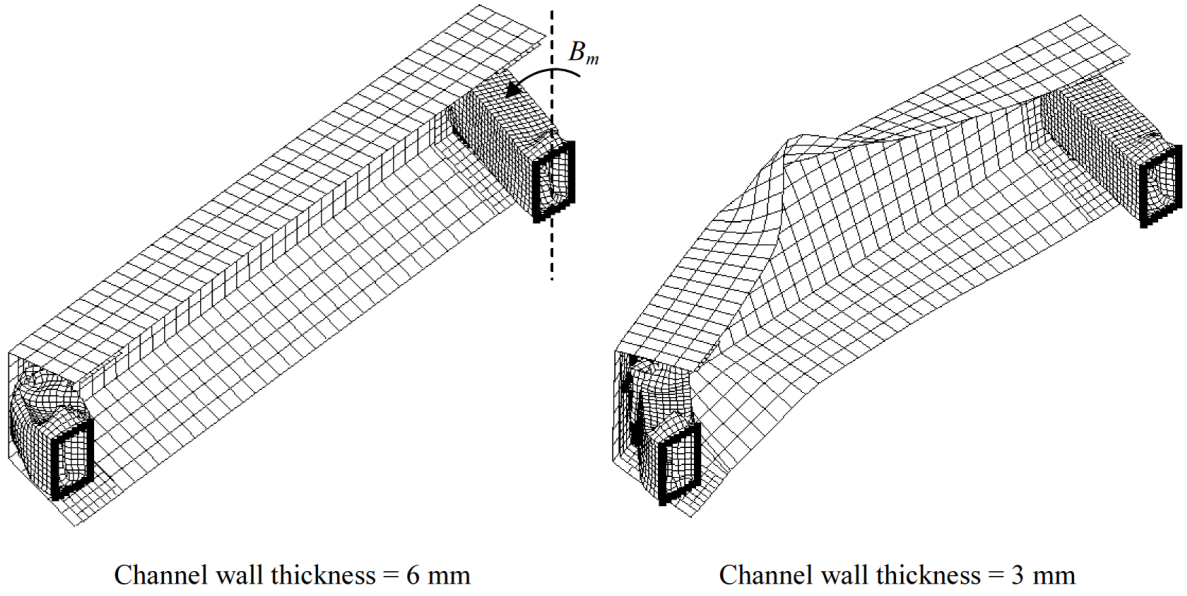

Figure 2.14: Bumper system deformation responses with varied channel wall-thickness under 30° oblique loading [44]

Decreasing the wall-thickness of the channel affects the stiffness of the load-bearing path and reduces the likelihood of progressive buckling of the energy absorbers. The non-impacted energy absorber provides a bending moment, B_m, which opposes the acting bending force due to the oblique/offset loading condition, shown in Figure 2.14. This bending moment and the stable loading path, created by a stiffer central channel member, provide lateral support for the impacted energy absorber. A decrease in the wall-thickness of the channel, reduced the lateral support for the energy absorber and promoted global buckling. The stiffness of this load-transferring member must hence remain sufficient to favourably promote progressive buckling. It was noted that the tapered tube system was less susceptible to the change in the wall-thickness of the channel at a critical load angle.

The tapered tube was observed to reduce the inertia and hence respond more controllably under dynamic loading conditions of the bumper system with high deflections. The use of tapered rectangular tubes as opposed to straight rectangular tubes as the primary energy absorbing component is more likely to maintain the energy absorption capacity of the system under oblique loading conditions.

2.4.3 Offset impact scenario

Hanssen *et al.* [45] experimentally and numerically tested a demonstrator car bumper system consisting of a transversal cross beam connected to two square columns with aluminium foam filler. The crossbeam was made from high strength aluminium alloy AA7108 with minimum Yield Stress of 400MPa and UTS of 440MPa. The square columns, acting as the energy absorbers termed crash boxes, were extrusions of the alloy AA6060T6 with outer dimensions 79.5mm x 79.5mm and wall-thickness of 1.5mm. The foam filler

consisted of $AlSi_8Mg$ base alloy with targeted density of 0.18g/cm^3 and a corresponding plateau stress of 1.5MPa. The bumper system was subjected to dynamic loading conditions under a drop hammer rig with 100% full contact and a non-symmetric 40% overlap, shown in Figure 2.15.

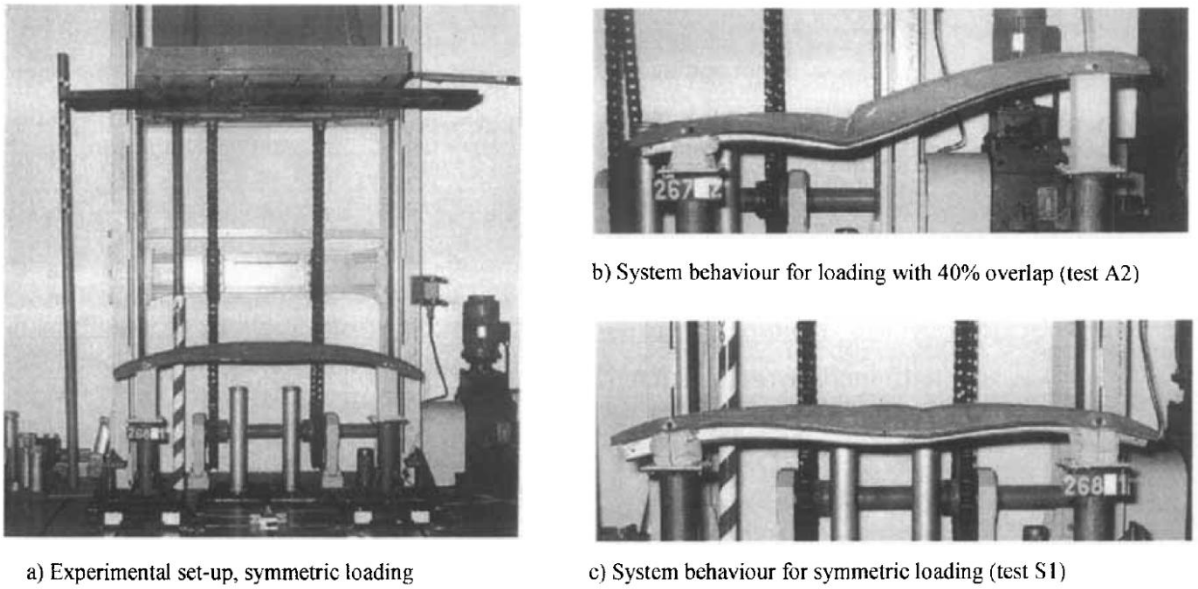

Figure 2.15: Drop hammer testing equipment (a) and typical system behaviour under (b) 40% offset and (c) full contact loading [45]

The hammer drop head velocity and mass for all tests were 17.7km/h and 576kg for 40% overlap; and 22.6-24.0km/h and 620kg for 100% overlap. In the 40% overlap test, the non-symmetric type of loading produced a global in-plane bending mode in the active crash box in addition to the progressive buckling. The large axial stiffness of the crossbeam and large rotations were also observed to cause the top of the active crash box to move inwards. In the 100% overlap tests, the crossbeam introduce a loading condition that cause an overturning moment, resulting in out-of-plane bending coupled with progressive buckling. To improve the performance and reduce the global effect of the crossbeam structural influence, horizontal and vertical slot are machined at the connection interface between both the crash boxes and crossbeam. Despite the scatter of the foam density of the experimental work, the mean forces were predicted within ±10% of the analytical formulae [46].

A numerical analysis was performed with LS-DYNA non-linear explicit solver using a piecewise linear curve to represent the aluminium alloys and a bi-linear material model for the foam. Both material models incorporate the isotropic hardening and isotropic yield criterion. The numerical results were in good agreement with the experimental force-displacement profiles as shown in Figure 2.16.

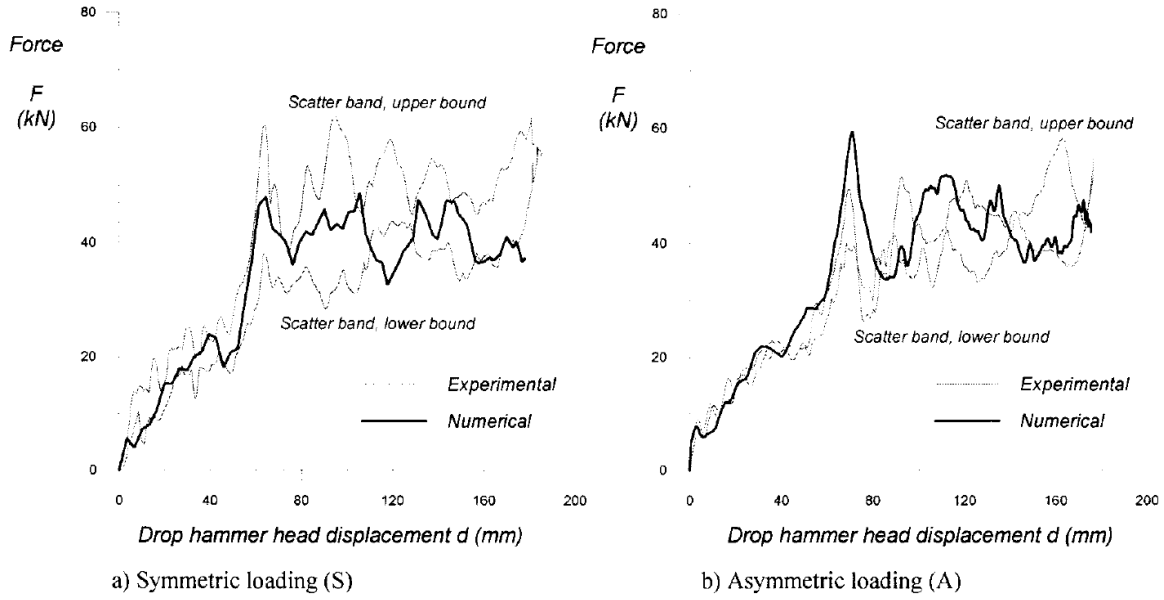

Figure 2.16: Comparison of load-displacement profiles of the experimental and numerical results under both loading conditions [45]

The numerical analyses somehow underestimate the global bending mode observed in the experiments; but did not affect the energy absorption of the crash boxes significantly. The force measurement at the inactive crash box was far below the maximum elastic strength and thereby had no permanent deformation.

Investigations by Kokkula [47-50] focused on a bumper system subjected to offset impact loading where experimental and extensive numerical work was performed; improving the physical understanding of the different phenomena that takes place during an offset impact of an automotive bumper beam-longitudinal system. The investigation included the effects of the alloy and tempering conditions of the longitudinal members, the trolley (impactor) arrangement and the impact velocities have on the response of the bumper system. The numerical work involved verification of a user-defined elasto-plastic material model, simulation of the forming process of the crossbeam to the required curvature and validation of the complete FE-model of the system.

The bumper system setup is shown in Figure 2.17. The trolley had a constant mass of 794kg, tested at two impact velocities 10m/s and 15m/s, using the Kicking Machine [51] were performed. The crossbeam material consisted of a single alloy AA7108-T6; whereas the longitudinal members material were varied with two alloys and two temper conditions, AA7003-T79, AA7003-T1 and AA6060-T1 were selected. The longitudinal members had a constant wall-thickness, span length and cross-section of 3.2mm, 650mm and 95x80mm^2 respectively

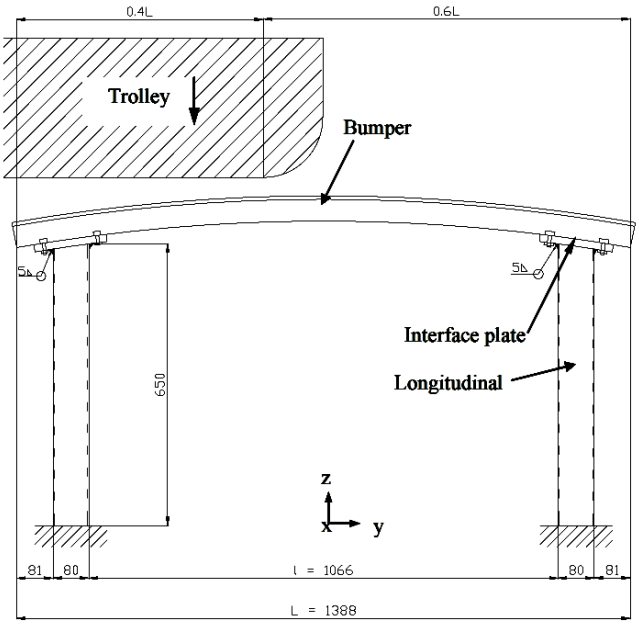

Figure 2.17: Configuration of the bumper system at 40% offset impact [48]

The true stress-plastic strain properties of the materials are shown in Figure 2.18. . Extensive material characterisation were carried out to obtain more accurate yield criterion, strain-rate hardening and fracture criterion. The three series of bumper systems investigated varied by the material used in the longitudinal members, as follows:

- **Series A**: AA7003-T79
- **Series B**: AA7003-T1
- **Series C**: AA6060-T1

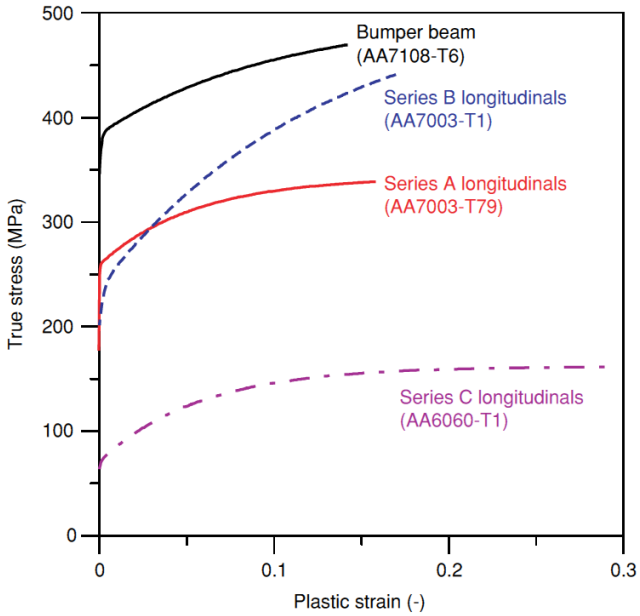

Figure 2.18: Stress-strain curves identified from uniaxial tensile tests along extrusion direction for the varies aluminium alloys and tempering [48]

Four custom made load-cells are placed at the fixtures of the longitudinal members and the head of the trolley. Additional crash boxes are placed on the reaction wall to keep the total displacement constant throughout the tests conducted. The experiments show that **series A** utilised the total impact energy more effectively compared to **series C**, having the lowest Yield Stress. The force-deformation profiles of all three series are similar for all the specimens apart from in **series B** where the crossbeam, in certain tests, had severe tearing failure. The temper condition of **series B**, T1, had significant effect on the crash performance as there was a likelihood of transition from progressive buckling to global buckling of the longitudinal members.

The major forms of deformation seen throughout the series of tests is progressive buckling of the impacted longitudinal member, bending failure of the crossbeam and inward buckle and/or shear failure at the interface of the non-impacted longitudinal member. Other modes of failure that were common within a series is local buckling at the fixed end of the non-impacted longitudinal member, propagating tearing of the crossbeam and some weld failure at the interface plate of the non-impacted longitudinal member. These deformation modes are shown in Figure 2.19 for a **series C** sample.

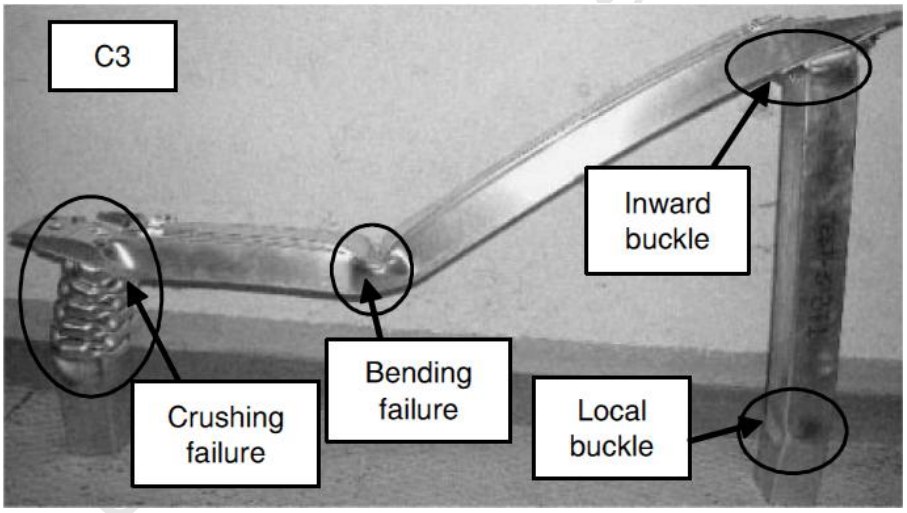

Figure 2.19: Common deformation modes observed in experiments [48]

Full-scale simulations were performed of the bumper system in LS-DYNA. The stretch-bending process of the curved crossbeam was undertaken, but only included the thickness variations of the component in the final modelling. Three different materials models were investigated for the longitudinal members and one material model for the crossbeam. Some tests included a CFS (*Critical Failure Strain*) fracture criterion. Figure 2.20 depicts the comparison of the load-deformation profiles of the experimental and numerical results.

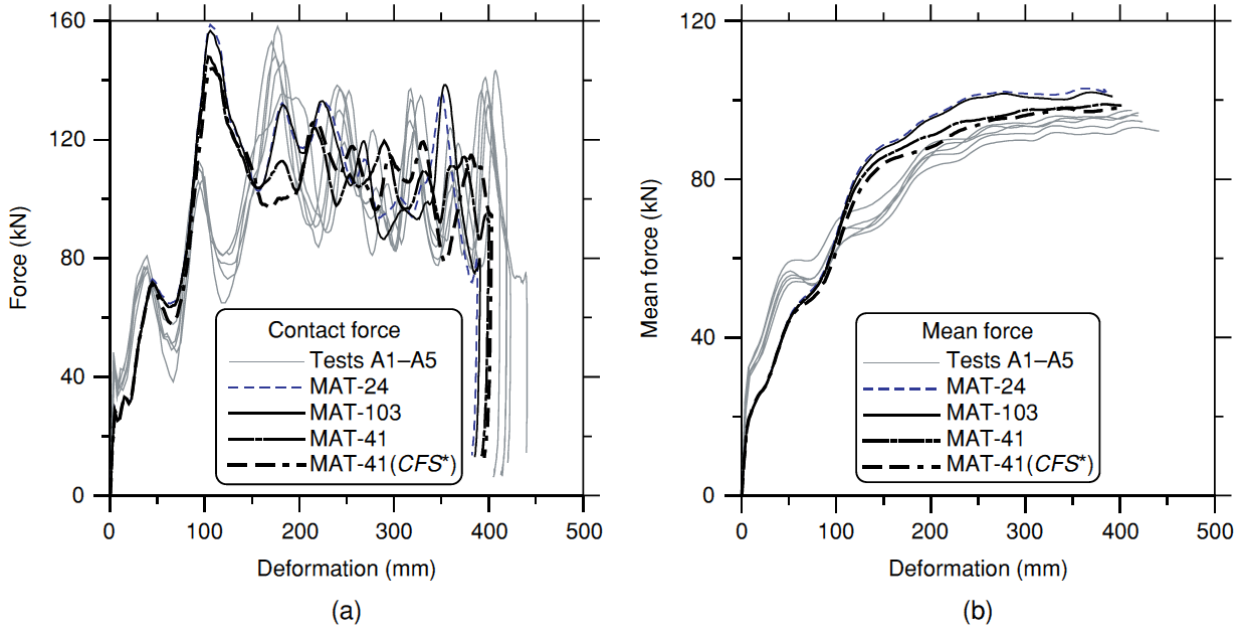

Figure 2.20: Comparison of (a) force–deformation and (b) mean force–deformation plots from the tests and simulations with different material models for test series A [48]

The force-deformation profiles showed an initial local peak force occurring at the failure of the curved crossbeam. Thereafter a maximum peak load was observed prior to the initiation of progressive buckling of the impacted longitudinal member. The cyclic profile after the peak force familiar with the formation of lobes in progressive buckling.

The energy dissipation, shown in Figure 2.21, of the impacted longitudinal member only initiated after a deformation of 100mm for **series A** and **series B;** once the curved crossbeam has collapsed and absorbed some impact energy. **Series C** showed energy dissipation of the impacted longitudinal member at a deformation of 50mm because the crossbeam material being stronger with higher Yield Stress than the longitudinal member, shown in Figure 2.18. The energy dissipated by the non-impacted longitudinal member accounted for only 1% in **series A** and **series B**, and only 0.5% in **series C** with relation to the total impact energy. The formation of the plastic hinge(s) in the non-impacted longitudinal member varies from 2.04% to 2.89% of the energy dissipated. As expected the impacted longitudinal member accounted for majority of the energy dissipation, being around 73% for **series A** and **series B** and 42% for **series C;** indicating that these members are the key structural elements for dissipating the impact energy.

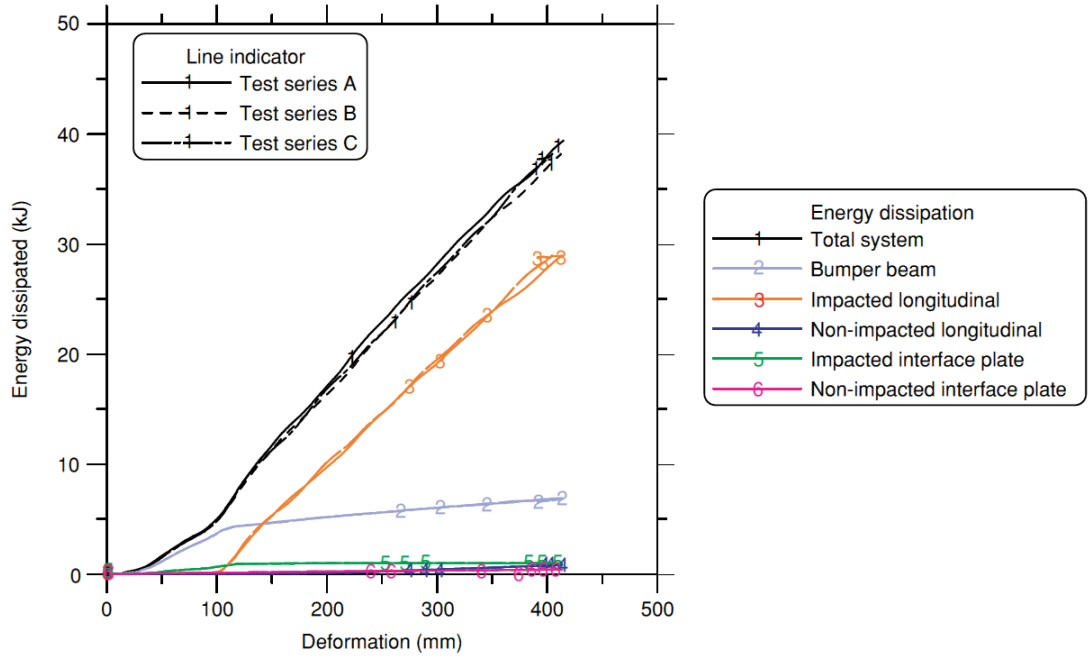

Figure 2.21: Energy distribution of the individual components of the bumper system for test series A,B and C [48]

Kokkula [47-50] further performed sensitivity studies to investigate the effects of different parameters numerically. These included:

i. Strain-rate effects
ii. Heat-affected zone size and exclusion
iii. Fracture criterion CFS and criterion due to Cockcroft and Latham [52]
iv. Self contact and dynamic shell thickness change
v. Different element formulation type
vi. Through-thickness integration points
vii. Mesh size and adaptive meshing

It was concluded that the AA7108, both tempers, provided the most significant anisotropy in strength, plastic flow and ductility in comparison to the other alloys. The robustness of the system was very dependent on the yield strength and temper condition of the longitudinals used. The user-defined material model represented the material behaviour accurately with respect to strength, strain hardening and strain-rate sensitivity. Some simulations failed to predict the deformation and fracture modes observed in the experiments, particularly in series B where extensive tearing occurred. The simulations failed to predict the complete bending failure of the crossbeam, which included cracking along the kinked edges.

2.4.4 Summary of bumper system investigations

Several studies have been is carried out to gain understanding on the behaviour of a bumper system to impact loading. The 40% offset impact scenario is well-known and employed in the crash test rating programmes. The investigation by Jenefeldt [43] showed that the strengthening of the crossbeam altered the energy absorbing capacity of the vehicle. Kokkula [47-50] carried out tests using several different materials for the longitudinal members only in an offset impact scenario. The response and energy absorbing characteristics of the bumper system was influenced to a significantly by the material selection of the components. Nagel [44, 53, 54] investigated a simplified bumper with varying the wall-thickness of the crossbeam and observed that an increase in the wall-thickness influenced the load bearing path between the longitudinal members, which promoted progressive bucking of the longitudinal members in certain cases. Tapered longitudinal members in the bumper system were also investigated and observed to be more favourable with oblique loading conditions and less susceptible to the variation of wall-thickness of the crossbeam.

.

3. Experimental Details

In this chapter, the details of the test setup, results and observations are discussed. A series of experiments is conducted with one parameter; the wall thickness of crossbeam members is varied. The effect of including through-hole discontinuities as buckling initiators in the longitudinal members is also investigated. Single tubes are also tested under the same impact test of the varied drop masses to compare the performance of the longitudinal members independently and within a bumper system. The experiments are carried out in the *High Strain Rate Laboratory* at the *Blast and Impact Survivability Research Unit* (BISRU), *University of Cape Town.*

3.1 Simplified bumper system

The bumper system tested in the series of experiments is simplified from an automotive bumper system, shown in Figure 3.1 (b), while maintaining the structural integrity. The simplified bumper system, shown schematically in Figure 3.1(a), consists of a crossbeam and two longitudinal members. In this study the crash box component of the bumper system is not included for simplification.

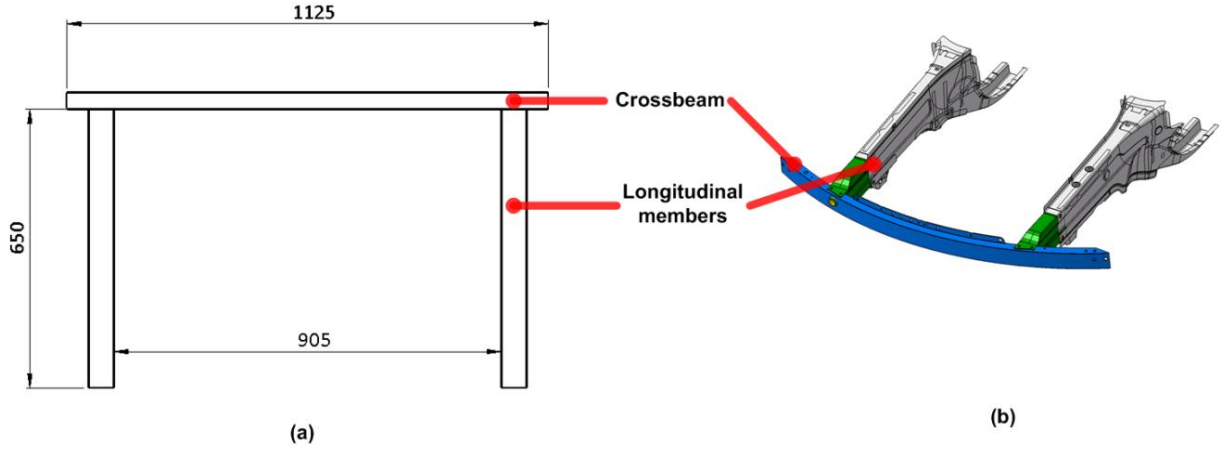

Figure 3.1: Illustration of (a) schematic of simplified bumper system and (b) a typical bumper system

The crossbeam has a cross-section of 60x40mm and is 1125mm in length. Three wall-thickness variations, 1.6mm, 2.0mm and 3.0mm, of the crossbeam are investigated. The longitudinal members are 650mm in length, have a cross-section of 60x60mm and a wall-thickness of 2.0mm. The single tube tests have equivalent dimensions as the longitudinal members. Investigating the response of including buckling initiators, the longitudinal members of one set include 3 pairs of through-hole discontinuities, 20mm in diameter, that are located 30mm longitudinally apart on alternating faces. The first pair of through-hole discontinuities is 60mm below the crossbeam-longitudinal member interface. The dimensions are chosen to initiate progressive buckling and to reduce the initial peak force,

as reported in Ref. [55]. The two longitudinal members are TIG welded to a crossbeam with a separation distance of 905mm. The material properties of the profiles are discussed in section 4.2.

3.2 Experimental test-rig and setup

The experiments are carried out in a drop tester that has a maximum drop height of 5m. The drop tester is a tower consisting of four steel channels extending vertically at each corner. Reinforcing steel members are connected to the main steel channels creating a rigid and robust tower. A trolley is situated between the main steel channels and moves freely along four guiding slots with negligible friction. The trolley allows for the adjustment of the drop mass by adding or removing slabs of steel. The impactor is fastened to the base of the trolley. The bumper system specimen is secured by clamping rigs to the foundation comprising of two large steel blocks (anvils) at both ends of the bumper system. The steel blocks within the drop tester are of mass 430kg while the steel blocks at the non-impacted end are approximately 110kg. The clamps, bolted to the steel blocks by means of four bolts, secure the lower 50mm of the longitudinal members. The test setup of the offset impact drop testing of the bumper systems is illustrated in Figure 3.2.

The placement of the bumper system is adjusted to achieve the 40% offset impact scenario with the impactor. The overall length of the impactor design is restricted to 500mm to fit safely within the drop tester during downward travel. The bottom contact plate of the impactor is made from mild steel of thickness 50mm with a curved end of 50mm radius. The impactor head is made from tool steel, to be durable, and is designed with a strengthening rib to compensate for the induced moments under the offset impact scenario. The anvil and clamping rig within the drop tester are aligned to ensure that the impactor strikes the longitudinal member centrally with respect to the width (60mm) of the member.

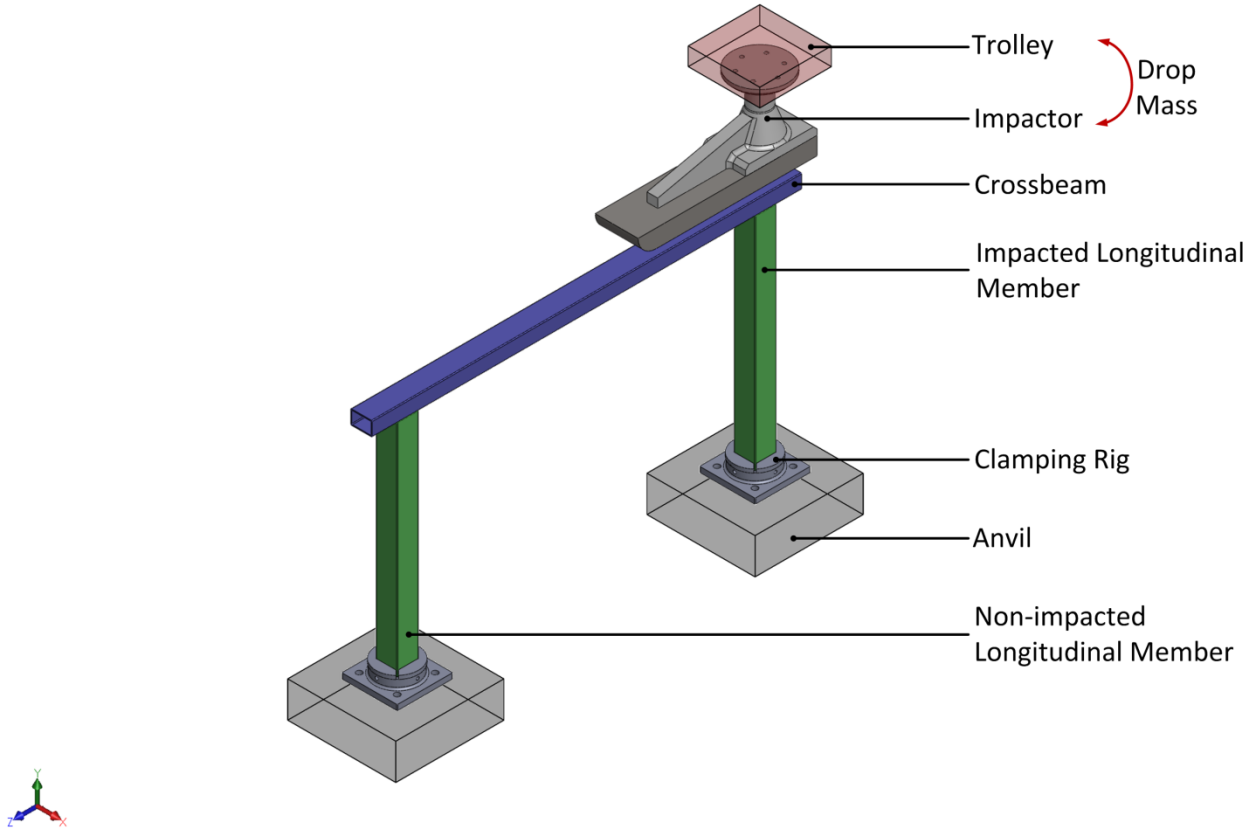

Figure 3.2: Schematic of the 40% offset impact scenario test setup

The experiments are carried out using 3 different drop masses, 301kg, 396kg and 491kg, released from a constant height of 4m above the top free surface of the crossbeam. The trolley is released with a pneumatic piston and accelerated by gravity, before impacting the top surface of the crossbeam. The bumper system absorbs the kinetic energy of the impactor and trolley assembly during the impact. Assuming no energy loss to friction and other forms, the energy absorbed equates to 11.81kJ, 15.5kJ and 19.3kJ respectively for the three drop masses investigated based on the conservation of potential energy. The series of experiments consist of 15 specimens and are summarised in Table 3.1.

Group	Crossbeam wall-thickness (mm)	Drop masses (kg)	Number of tests
B1	1.6	301, 396, 491	3
B2	2.0	301, 396, 491	3
B3	3.0	301, 396, 491	3
BD3	3.0	301, 396, 491	3
Single Tube	-	301, 396, 491	3

Table 3.1: Summary of experiments carried out

3.3 Experimental results

The observations from the parametric experimental study are presented in this section. The results are grouped on the basis of the wall-thickness of the crossbeam, and are labelled as follows:

B1-xxx	for the 1.6mm wall-thick crossbeam
B2-xxx	for the 2.0mm wall-thick crossbeam
B3-xxx	for the 3.0mm wall-thick crossbeam
BD3-xxx	for the 3.0mm wall-thick crossbeam with through-hole discontinuities

where '**xxx'** represents the drop mass of 301kg, 396kg or 491kg.

Between the groups, the responses of the bumper systems are similar, thus the results are arranged according to the deformations and behaviour, and not by the parameter.

3.3.1 Deformation modes between bumper systems

In general, the deformation modes observed from the impact test are recurring throughout the different groups of specimens. Four common deformation modes, shown in Figure 3.3, are observed:

- progressive buckling of the impacted longitudinal member
- lateral flattening of the crossbeam at impacted end
- local bending failure of the crossbeam
- plastic hinge formation at the interface of longitudinal member-crossbeam at non-impacted end

These modes of deformation are typical in thin-walled structures subjected to impact loading. The impact energy is predominantly absorbed by the impacted longitudinal member in a progressive buckling manner, showing more prominent deformation. All the single tubes deformed in progressive buckling mode where the crush distance and number of lobes increases with drop mass.

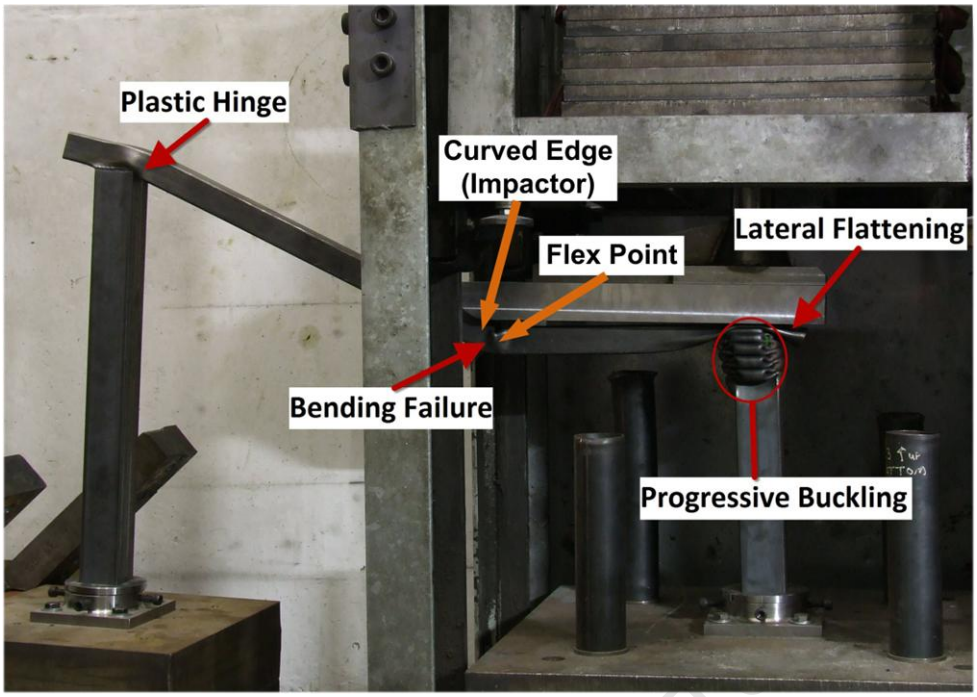

Figure 3.3: Deformation modes of *B1-491* bumper system subjected to 40% offset impact (shown in drop tester)

3.3.1.1 Thinner crossbeam specimens: B1 & B2

The response of the **B1** and **B2** bumper systems, shown in Figures 3.3 and 3.4, are similar in nature. The wall-thicknesses of the crossbeam and longitudinal members in the two groups are comparable and showed no apparent difference in the behavioural response. Typically, the crossbeam also acts as a load bearing path, transferring the impact energy to the longitudinal members. The lack of significant deformation observed at the non-impacted longitudinal member suggests that no substantial energy is transferred across the crossbeam.

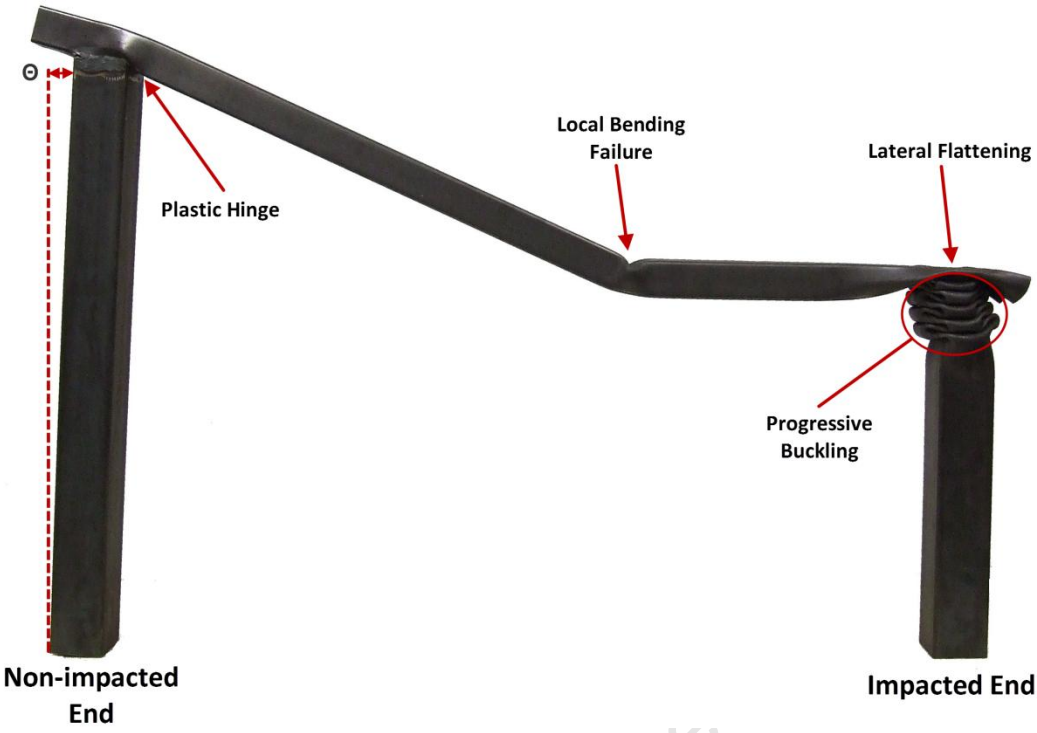

Figure 3.4: Deformation modes of *B2-491* bumper system subjected to 40% offset impact

The crossbeam is laterally flattened at the impacted end in the **B1** and **B2** group irrespective of drop masses. The progressive buckling of the longitudinal member is initiated; indicating that the force requirement to lateral flattening mode is less compared to the progressive buckling mode force requirement; even if the wall-thicknesses of the components are comparable.

The local bending failure of the crossbeam occurs at a similar distance from the free edge between all group tests. The 1.6mm and 2.0mm wall-thicknesses prove to be sufficiently low in load bearing capacity to generate a local bending failure in close proximity to the curved edge of the impactor. The bending failure is more prominent with larger crushing distances for both **B1** and **B2** groups. The bending failure is more excessive with a higher drop mass as more flexing occurs in the crossbeam with the higher travel distance of the impactor.

The crossbeam deforms in a local bend mode near mid-point as it is laterally constrained by the longitudinal members during the impact. This restriction causes the crossbeam to bend along the curved edge of the impactor, creating a flexing region. The flexing region does not coincide with the corners of the impactor bottom face. Further deformation is observed in the side-walls of the crossbeam as the tube side-walls fold outwards; which is typical behaviour in thin-walled structures. The flexing region and side-wall folding are shown in Figure 3.5.

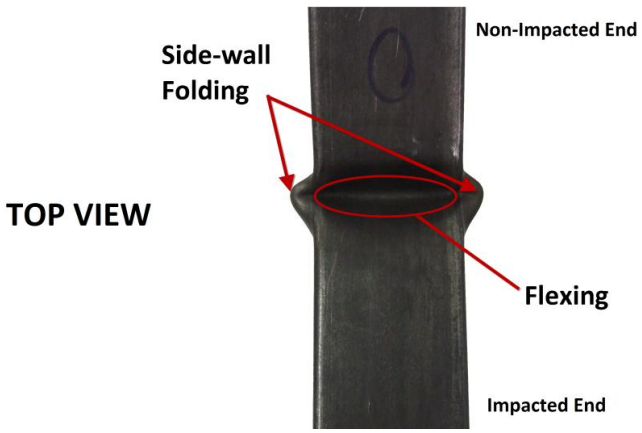

Figure 3.5: Bending failure of crossbeam of *B1-491* bumper system subjected to 40% offset impact scenario

With the increasing drop masses, the loading mechanism changes at the non-impacted end caused by the increased downward travel of the impactor. This subsequently increases the lateral force (*due to pull-in motion*) and downward force (*due to bending moment*) at the interface of the crossbeam and non-impacted longitudinal member, as shown in Figure 3.6. The crossbeam side-walls expand outwards with the increase in pulling motion and bending moment, folding along the plastic hinge as shown in Figure 3.7 as it is a high stress concentration region. The plastic hinge form at the inner side of the interface where the crossbeam and longitudinal member converge at 90° which is a high stress concentration area, termed *stress-concentrator*, and is largely influenced by the bending moment. This *stress-concentrator* causes an increase in deformation at this interface and decreases the stability of the non-impacted end. The amount of side-wall folding, i.e. the crush distance, is dependent on the wall-thickness of the crossbeam and the drop mass. The thicker walls are more robust, thus effectively transferring the load through the bumper system.

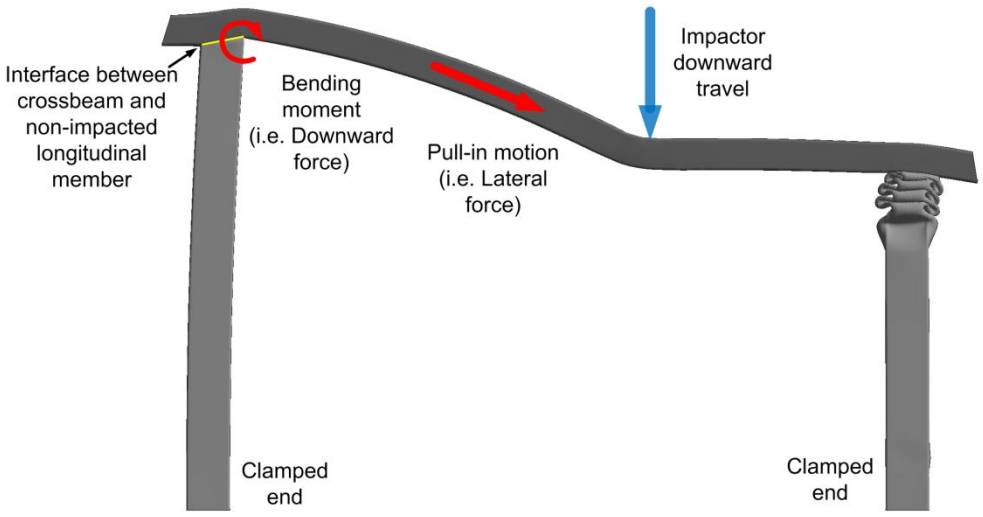

Figure 3.6: Schematic of force and moment acting at the non-impacted end

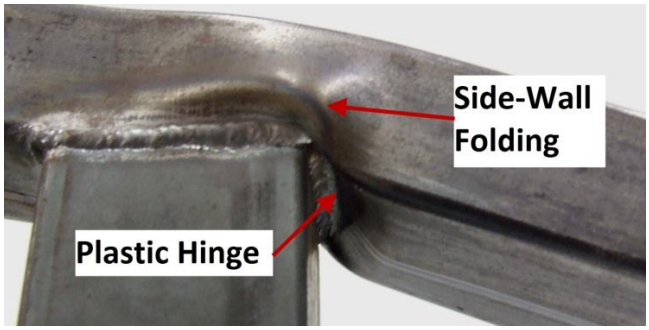

Figure 3.7: Plastic hinge and side-wall folding at non-impacted end

The vertical plane of the non-impacted longitudinal member is skew due to the release of the elastic strain at the plastic hinge, and minor deformation in the straightness of the profile. Upon examining of the bumper system after the impact, the non-impacted longitudinal member appears non-parallel to the impacted longitudinal member; shown in Figure 3.4 as **Θ**. The angle is apparent in thin crossbeam systems with major plastic hinges forming at the crossbeam-longitudinal interface. In systems with thicker crossbeams, the non-impacted longitudinal members remain straight, as only minor plastic hinges are formed by the crossbeams.

3.3.1.2 Thicker crossbeam specimens: B3 & BD3

The deformation modes observed for the bumper with thicker crossbeams is similar to that of thinner crossbeams (1.6mm and 2mm) apart from lateral flattening; shown in Figure 3.8. The thick-walled crossbeam has a higher loading requirement to collapse than the progressive buckling of the longitudinal members in this system configuration. The increase in wall-thickness increases the rigidity of the crossbeam, resulting in a small local bending failure near the curved edge of the impactor. The thick-walled crossbeam reduces the inward pulling tendency generated by the downward travel of the impactor and does not substantially alter the load transferring mechanism during the impact. A minor plastic hinge is formed at the interface of the crossbeam and non-impacted longitudinal member. The side-wall folding of the crossbeam is not excessive and, as such, is barely visible.

In all cases, the non-impacted longitudinal member is observed to have very little deformation. Minor local buckling of the outer faces at the clamped end of the non-impacted longitudinal member is observed. This mode only occurs with high drop mass and thicker crossbeam walls.

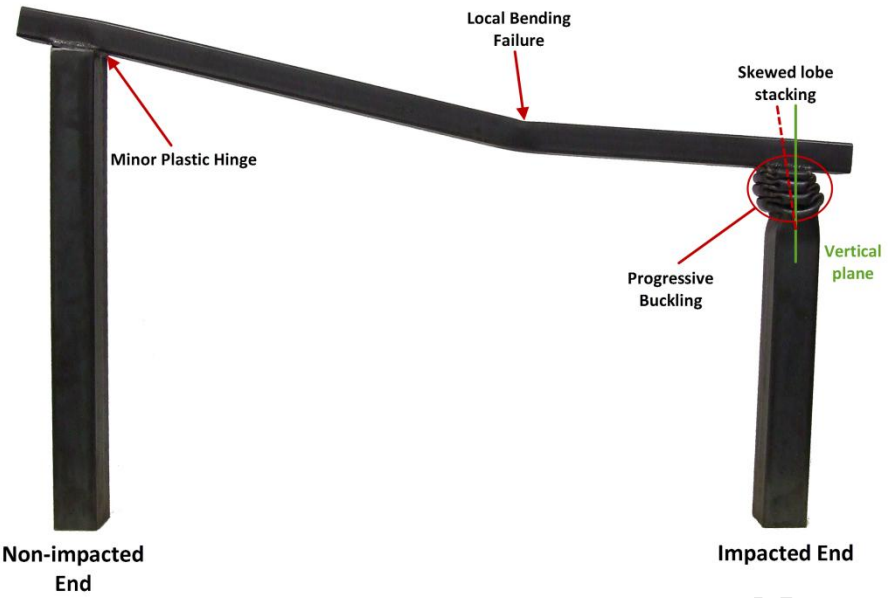

Figure 3.8: Deformation modes of *B3-396* bumper system subjected to 40% offset impact

The **BD3** bumper systems include through-hole discontinuities to investigate the effect of including triggers on the response of the simplified bumper system. The overall response is similar to the **B3** group. The deformation modes are common throughout the tests and are shown in Figure 3.9. The inclusion of the triggers alters the lobe formation stacking of the impacted member and is discussed in section 3.3.3.

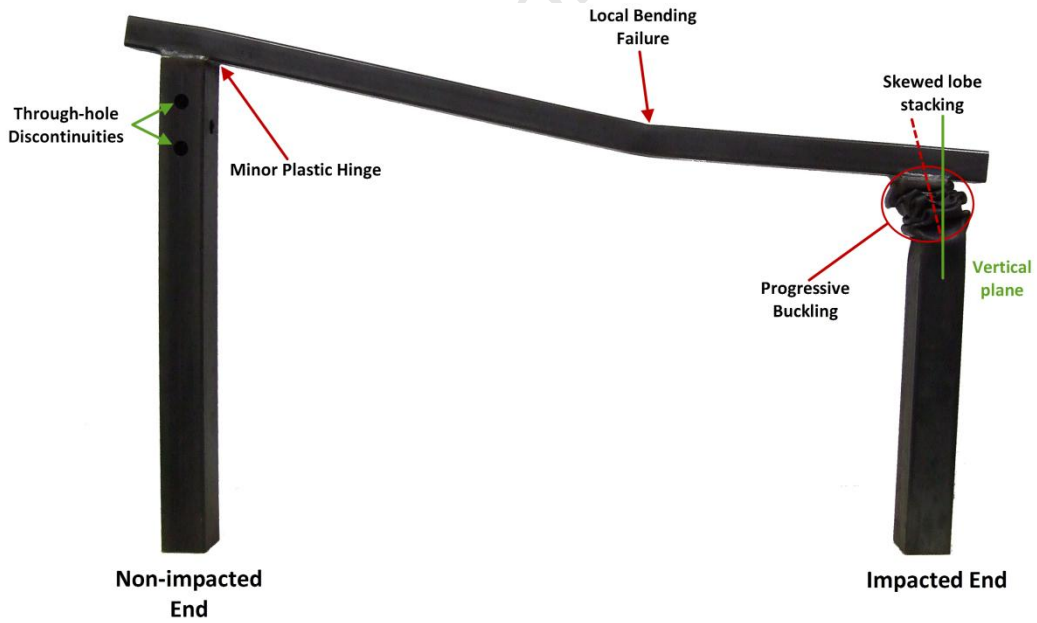

Figure 3.9: Deformation modes of *BD3-396* bumper system subjected to 40% offset impact

3.3.2 Deformation onset and response time

High-speed video footage was taken at the impacted end during the execution of experimental work to investigate the transient response of the crossbeam and impacted longitudinal member. The camera used is a Photron FASTCAM-APX RS 250K, recording at 12,000 fps using a resolution setting of 640x384 pixels and shutter speed of 1/20,000s. Upon impact, the crossbeam is the first component to interact with the impactor to transfer/absorb the impact energy is the crossbeam member. The time and relative distance travelled by the impactor is measured and calculated from the onset of impact till zero velocity. Standard video software was used to manually follow several chosen pixels of the impactor. Different wall thicknesses of the crossbeam result in different onset of deformation and therewith the response time of the major failure modes.

In the thinner-walled systems, i.e. 1.6mm and 2.0mm, the deformation modes initiate in the following sequence:

i. Lateral flattening of crossbeam at impacted end
ii. Local bending of crossbeam near impactor edge
iii. Progressive buckling of impacted longitudinal member
iv. Plastic hinge formation at interface of crossbeam and non-impacted longitudinal member

- **1.6mm**

Figure 3.10 shows the transient response of the simplified bumper system at the impacted end. For the **B1-396** case, the crossbeam is fully collapsed at 4.8ms in the interface region; before progressive buckling is initiated. The first fully developed lobe of the impacted longitudinal member is formed at 9.2ms. The impactor and trolley assembly reach zero velocity after 54ms, before rebound and elastic release occurs. The time to flatten the crossbeam is generally similar irrespective of drop mass. However the time to reach zero velocity differs. For drop masses of 301kg (specimen **B1-301**) and 491kg (specimen **B1-491**) the times are 37ms and 71ms respectively.

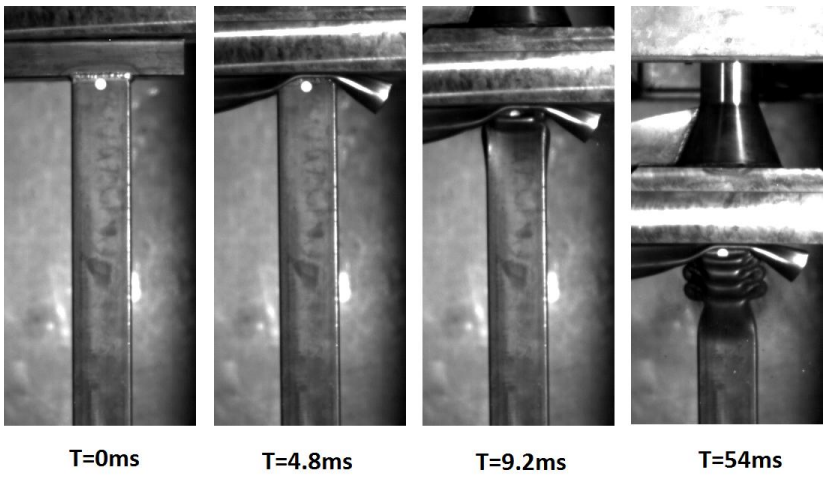

Figure 3.10: Deformation of impacted end of the *B1-396* bumper system at significant time instances

2.0mm

For **B2-396** case, shown in Figure 3.11, the crossbeam is fully collapsed in the lateral direction at a time of 4.3ms. The first fully developed lobe is formed at 7.7ms. Zero velocity of the impactor is recorded at 37ms for the **B2-301**, 45ms for the **B2-396** and 68ms for the **B2-491** bumper systems.

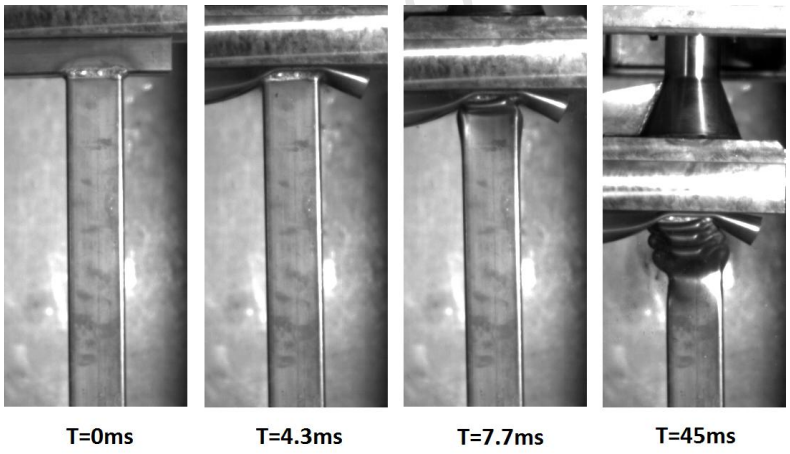

Figure 3.11: Deformation of impacted end of the B2-396 bumper system at significant time instances

- **3.0mm**

For the thicker-walled systems, crossbeams of 3.0mm, the deformation modes are initiated in the following sequence:

i. Progressive buckling of impacted longitudinal member
ii. Minor local bending of crossbeam near impactor edge
iii. Minor plastic hinge formation at interface of crossbeam and non-impacted longitudinal member

The first component in the **B3** and **BD3** bumper system to deform is the longitudinal member at the impacted end. For the **B3-396** case, Figure 3.12, shows that the first lobe of progressive buckling initiates and is fully developed at a time of 3.8ms. There is no indication of lateral flattening of the crossbeam throughout the **B3** and **BD3** group cases.

Figure 3.12: Deformation of impacted end of the *B3-396* bumper system at significant time instances

The initiation of progressive buckling differs for the **BD3** group due to the inclusion of triggers in the longitudinal members. The triggers are incorporated to initiate progressive buckling at a lower peak force. The spacing of the three pairs of through-hole discontinuity in the **BD3** bumper system produces earlier buckling of the member than the **B3** bumper systems. The triggers permit the lobes to 'pinch' more, which results in a flatter lobe formation at a time of 6.0ms. The time until zero velocity of the impactor is 44ms. The times for the impactor to reach zero velocity for the two thick-walled groups (B3 and BD3) are both 44ms, suggesting that the mean crush force may be similar.

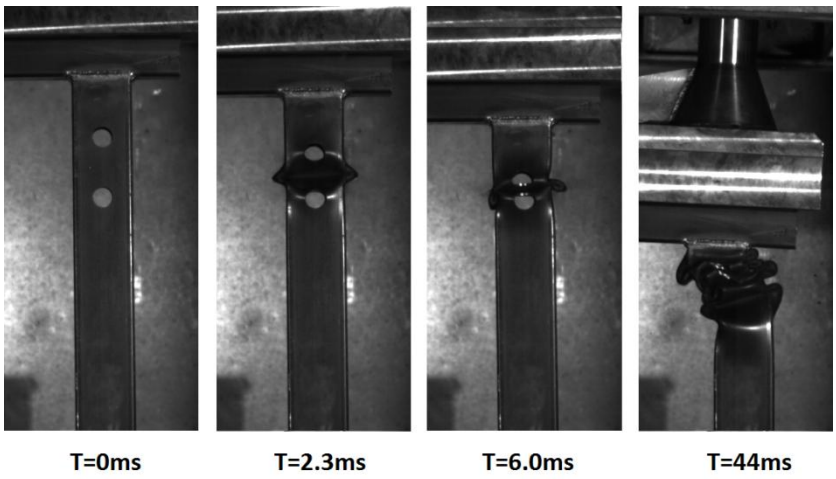

Figure 3.13: Deformation of impacted end of the *BD3-396* bumper system at significant time instances

3.3.3 Impacted longitudinal member response

The impacted longitudinal member is the main energy absorbing structure in the bumper system. The progressive buckling of the impacted member is favourable and results in high energy absorbing capacity. The deformation of the impacted longitudinal member is more substantial with a higher drop mass; resulting in the formation of additional lobes absorbing the increase in impact energy. The lobes are formed in an asymmetric mode and is defined when *two opposing walls move inwards while the other opposing walls move outwards, creating a single fully developed lobe*.

It is observed for the higher drop masses that lateral forces, as a result of the pull-in motion shown in Figure 3.6, are more influential on the formation of progressive buckling. The lateral forces increased with the increased crushing distance as the bending of the crossbeam is more substantial. The lateral forces affect the stacking of the lobes offsetting it from the vertical plane of the longitudinal member, as shown in Figure 3.8.

Figure 3.14 shows the lobe formations of the **B1** bumper system group, where fully developed lobes are numbered. A partially developed lobe is noticeable in the **B1-301** and **B1-491** bumper systems and labelled accordingly. The lobe formation absorbs the impact energy through plastic hinge formation and folding of the side-walls of the longitudinal member.

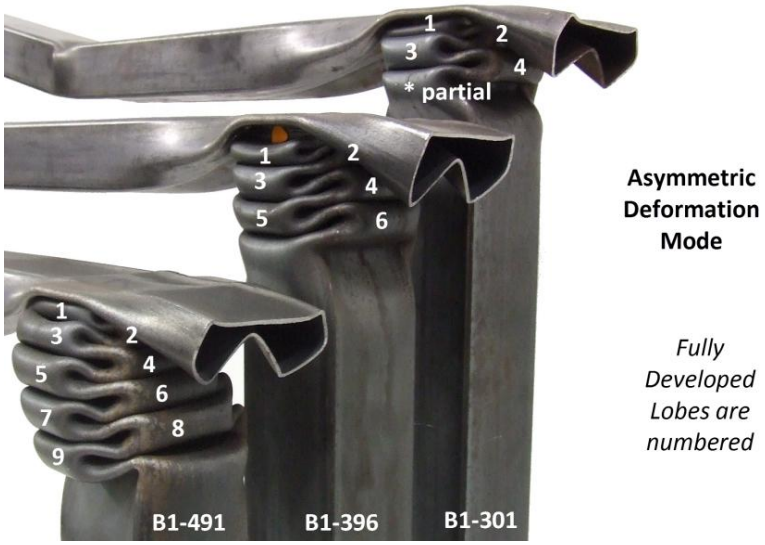

Figure 3.14: Comparison of the lobe formation in the *B1* bumper system group

The lobe formation in the **B2** group is similar to the **B1** group, showing a respectable trend. The number of fully developed lobes is shown in Figure 3.15 and demonstrates the asymmetric mode of the progressive buckling. Partial lobes are observed to be more prominent in the **B2-301** and **B2-396** bumper system tests.

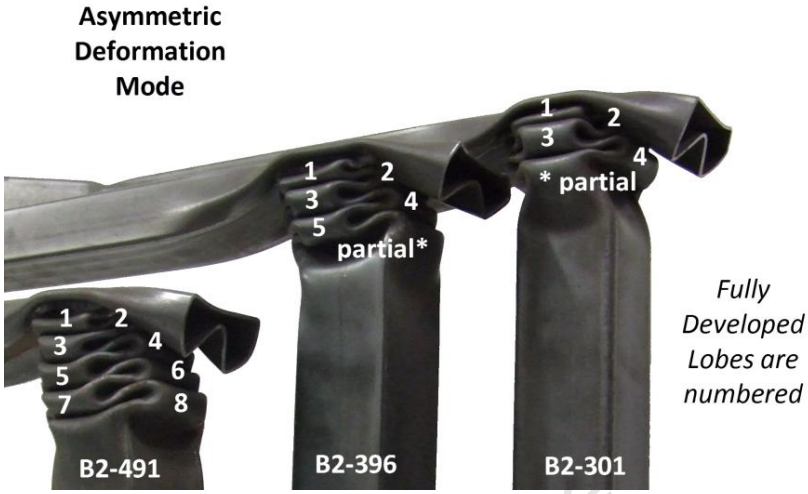

Figure 3.15: Comparison of the lobe formation in the *B2* bumper system group

The lobe formation of the **B3** bumper system tests are shown in Figure 3.16. Small lateral forces are generated from the crossbeam inward pulling motion due to the impactor. This causes the formation of the lobes to offset slightly towards the centre of the system, i.e. the direction of the pull-in. The lobe stacking is more offset with the higher drop mass as lateral forces are of greater magnitude.

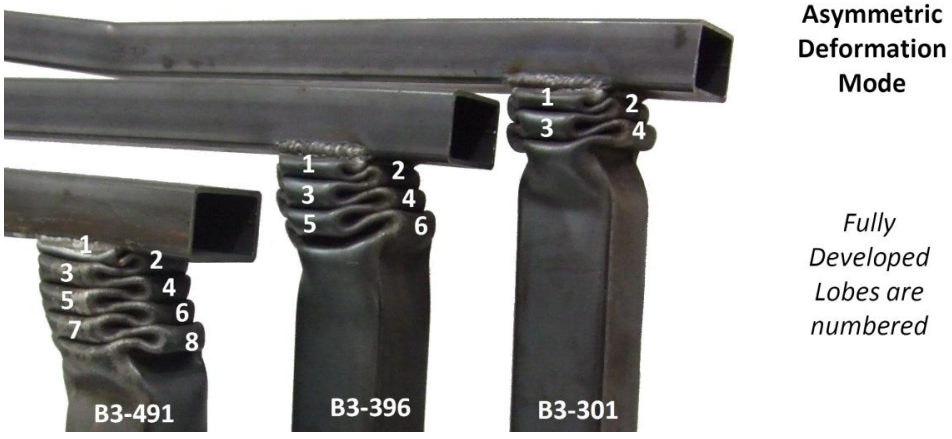

Figure 3.16: Comparison of the lobe formation in the *B3* bumper system group

Within the **BD3** group, the number of lobes formed is generally slightly greater, by one or a partial, than the **B3**, **B2** and **B1** groups. The presence of the discontinuites allowed the lobes to 'pinch' more during the formation, resulting in excessive compression of the lobe stacking. The bumper systems show less resilience to the lateral forces created by the pull-in motion of the crossbeam. This is evident in the unsymmetrical stacking of the lobes and the skew alignment to the impacted longitudinal member's vertical plane.

Figure 3.17: Comparison of the lobe formation in the *BD3* bumper system group

3.3.4 Crush distance at impacted end

There is a direct correlation between the increase in crush distance and increase in impact energy, which is induced by the increase of the drop mass. The crush distances of the bumper systems tested experimentally are illustrated in Figure 3.18. The crush distances of the **BD3** group is the lowest of all the groups and may be accounted for by the excessive compression and unsymmetrical stacking of the lobes formed due to the discontinuity.

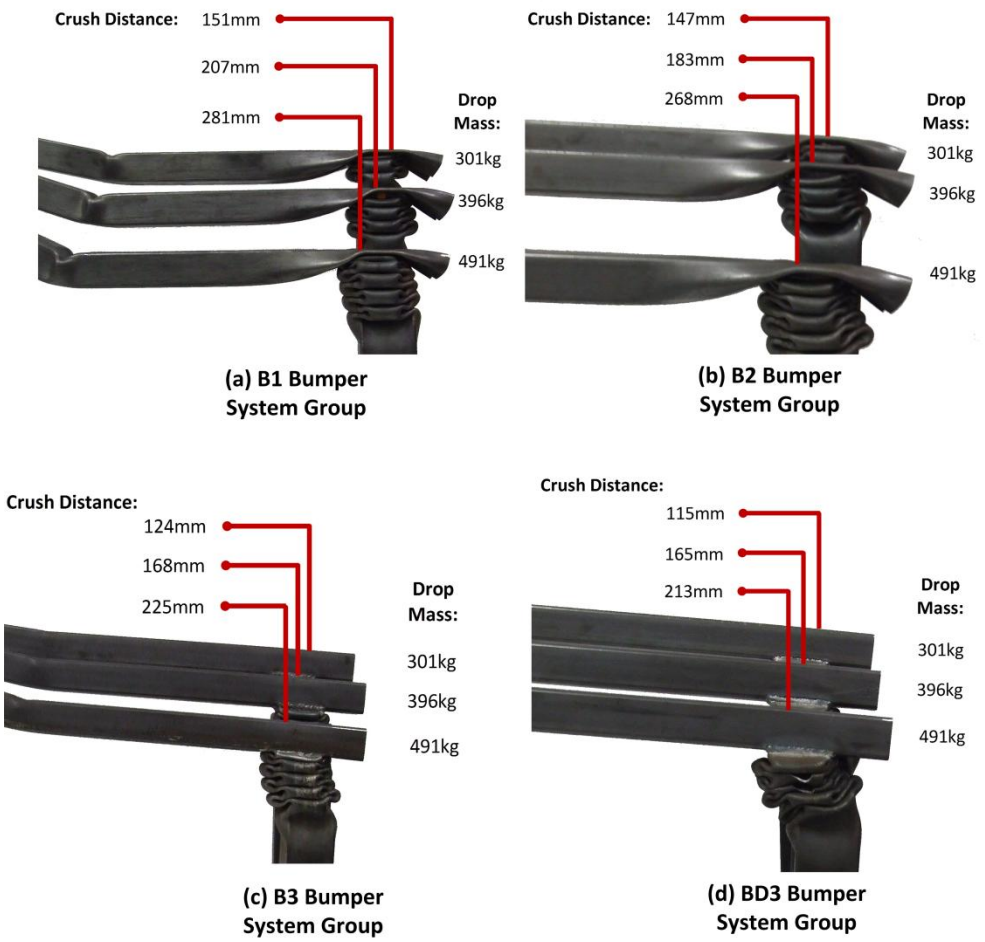

Figure 3.18: Comparison of crush distance at impacted end of bumper system groups

3.4 Analysis of experimental results

The wall-thickness of the crossbeam is the only parameter within the different bumper system groups. The alteration of the wall-thickness shows different responses concerning the deformation modes and the sequence of the initiation. Four deformation modes are common throughout the experimental investigation.

The three measurements, taken on the tested bumper systems, are illustrated in Figure 3.19. The crush distance is the difference between the initial and final height of the bumper system above the impacted longitudinal member central-line. The flex point height is the measurement taken from the ground to the inner kink within the local bend of the crossbeam. The flex point distance is taken from the free edge of the crossbeam at the impacted end.

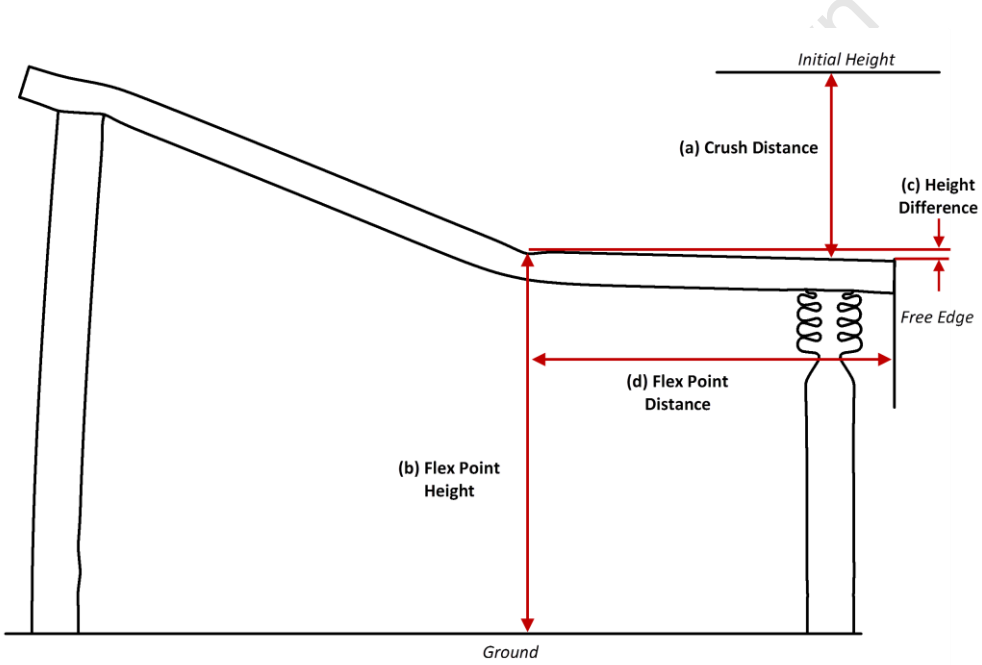

Figure 3.19: Schematics showing the location of experimental measurements of tested bumper system

3.4.1 Crush distance

The *crush distance*, shown in Figure 3.19 (a), is a function of the drop mass and drop height; namely impact energy. The increase in the drop mass or drop height increases the total impact energy required to be absorbed by the bumper system; resulting in higher crushing distance. The same result is observed for the single tube tests. The *crush distance* measurements of all bumper systems and single tubes tested experimentally are plotted in Figure 3.20. The results show that, for the range of tests carried out experimentally, there is a decrease in the crush distance of the longitudinal member with an increase in the wall thickness of the crossbeam. The crossbeam is the load bearing path of the bumper system. Increasing the wall-thickness of the crossbeam increases the rigidity of this path and thereby

enhances the transfer of the impact energy through the system; allowing more impact energy to be dissipated. In the case of an "infinitely rigid" crossbeam, the bumper system would behave differently and the deformation at the interfaces between the crossbeam and both longitudinal members would be far more significant. The crush distance results for the single tubes are greater than the bumper system results, implying that the impacted longitudinal members does not absorb all the impact energy but the bumper system dissipates the impact energy to an extent.

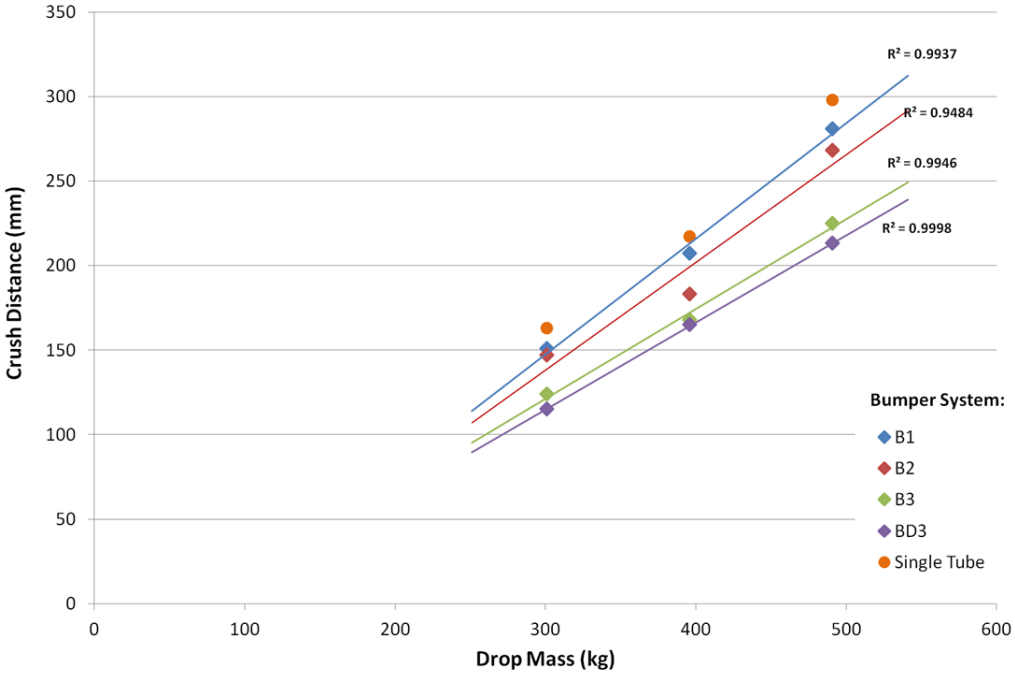

Figure 3.20: Graph showing the measured crush distance against drop mass for bumper systems tested experimentally

3.4.2 Flex point height and height difference

The *flex point height* is measured, as shown in Figure 3.19 (b), for additional comparison and validation of the numerical modelling. The height, Figure 3.21, shows a decreasing trend with the increase in the drop mass. The *flex point height* is directly related to the distance the bumper system is crushed. The result of the comparison between the flex point height and crush distance is plotted in Figure 3.22. The *height difference*, as shown in Figure 3.19 (d), is the difference between the *crush distance* and *flex point height*. The *height difference* is substantially larger with an increase in wall-thickness of the crossbeam. Of wall-thicknesses 1.6mm and 2.0mm, the *height difference* is greater by a factor of 2 or more. The same is experienced between the 2.0mm and 3.0mm groups. This increase in *height difference* substantiates the more elastic release and rebound occurred within the thicker-walled crossbeams; indicating that the thicker walled crossbeams absorb more energy during impact as less is transferred to the impacted longitudinal member. The thinner-

walled crossbeams deform past a toggle point in the bending failure, reducing the amount of energy that can be released.

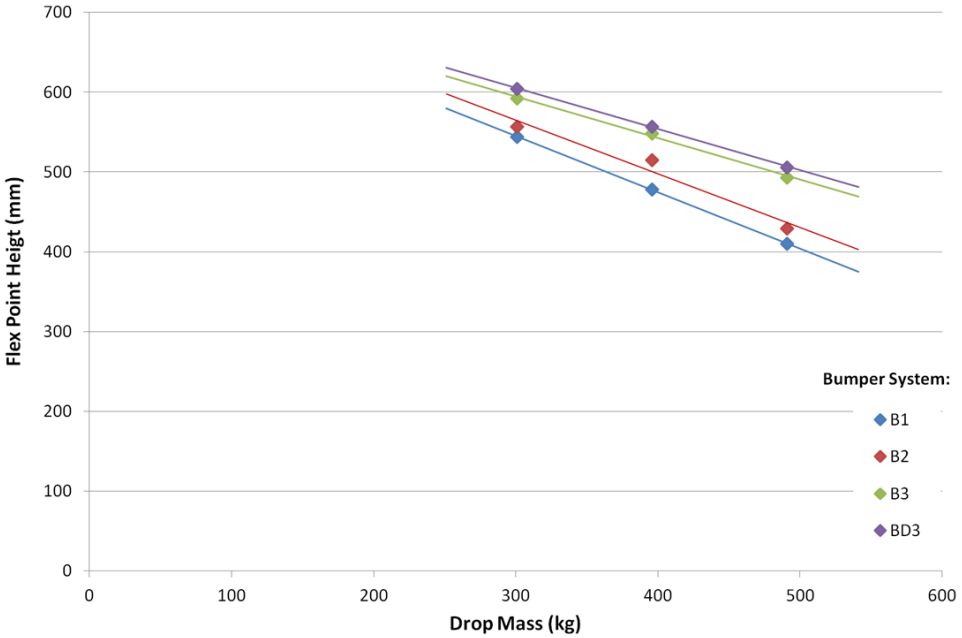

Figure 3.21: Graph showing the measured flex point height against drop mass for bumper systems tested experimentally

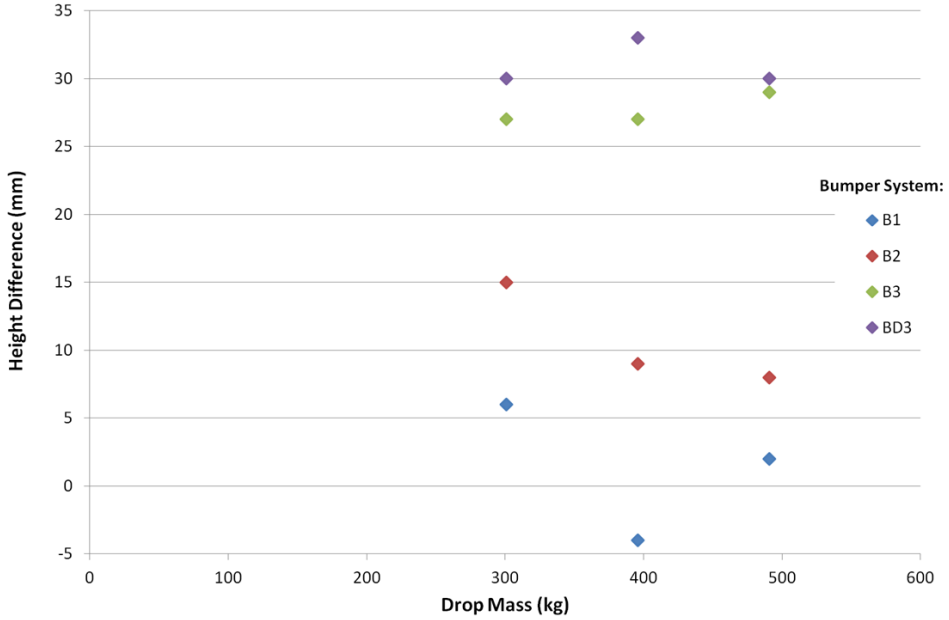

Figure 3.22: Graph showing the height difference against drop mass for bumper systems tested experimentally

3.4.3 Flex Point distance

The *flex point distance*, as shown in Figure 3.19 (d), measurements indicate that the tests conditions are consistent, occurring at similar location irrespective of the bumper system. This measurement is more a structural orientated result. The standard deviation of the measurements between the bumper system groups are 4.7mm, 2.6mm and 1.6mm at drop masses of 301kg, 396kg and 491kg respectively. It should be noted that the *flex point distance* does not coincide with the curved edge of the impactor, shown in Figure 3.3.

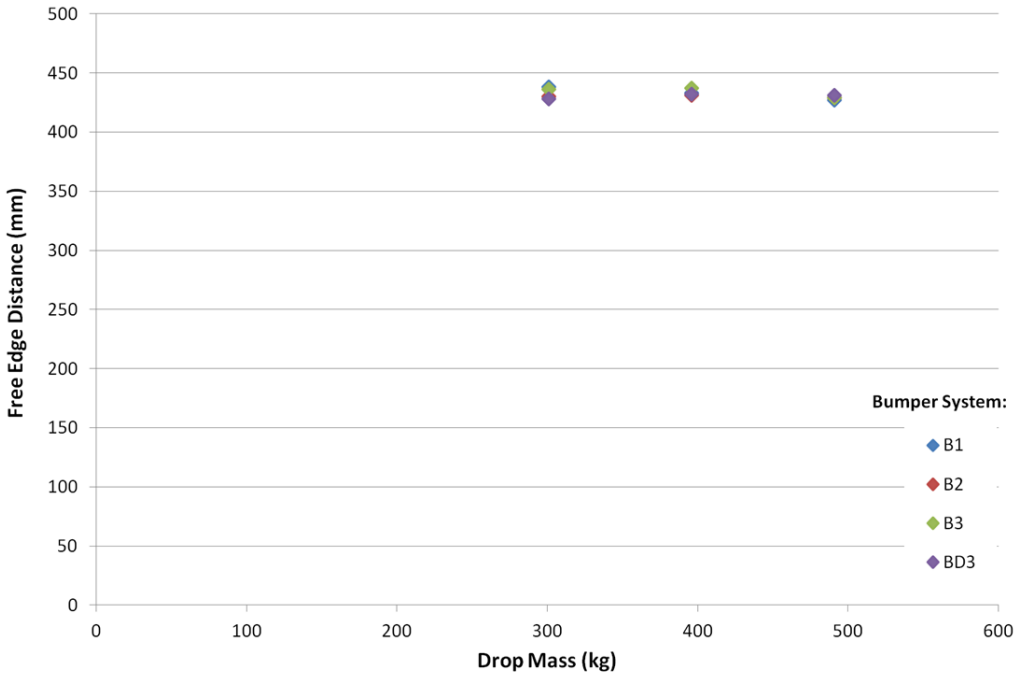

Figure 3.23: Graph showing the free edge distance against drop mass for bumper systems tested experimentally

3.4.4 Approximate mean force

Employing Newton's 2nd Law and equations of motions, the mean crush force is approximated using the footage from the high speed camera from first contact until zero velocity of the striker. The impact velocity (final velocity) of the impactor is approximated to be 8.85ms^{-1} using equation 3.1, where initial velocity, *u*, is 0ms^{-1} and the drop height, *s*, is 4m.

$$v^2 = u^2 + 2as \tag{3.1}$$

where v: Final velocity a: Gravitational acceleration constant of 9.8 ms^{-2}
u: Initial velocity s: Distance travelled

The deceleration of the impactor is determined by the time taken, Δt, from impact to zero velocity; using equation 3.2. The high speed footage is analysed by tracking the bottom face of the impactor from contact with the crossbeam till the impactor reaches zero velocity.

$$Mean\ Deceleration = Impact\ Velocity/\Delta t \tag{3.2}$$

Thereafter Newton's 2nd law is applied to determine the approximate force, given in equation 3.3, using the impactor mass (shown in Table 3.2) and the mean deceleration calculated using equation 3.2.

$$Force = Mass\ \times Acceleration \tag{3.3}$$

The approximate mean crush force is summarised in the Table 3.2.

Approximate Mean Crush Force (kN)				
Drop Mass	**B1**	**B2**	**B3**	**BD3**
301kg	66.8	65.8	82.3	83.9
396kg	64.4	72.4	80.0	80.9
491kg	59.7	64.0	76.6	81.7

Table 3.2: Approximate mean crush force in bumper systems tested experimentally

3.5 Discussions

The response of a simplified bumper system to the 40% offset impact scenario, similar to the study by Kokkula [48-50], is presented. The deformation modes observed are repetitive for all the tests carried out with different impact energies and wall thicknesses of the crossbeam. The results indicate that the highest energy absorbing mechanism of the bumper system is the progressive buckling mode observed in the longitudinal member at the impacted end. For the test range carried out, the non-impacted longitudinal members show little deformation, thus no categorised deformation mode is observed. This indicates that a crossbeam of this geometry is not a suitable or optimal load bearing path. A full, 100% offset impact scenario would result in buckling of both longitudinal members, however in the 40% offset impact scenario, additional load mechanisms within the bumper system are introduced with various modes of deformation. Other deformation modes observed include the local bending of the crossbeam, the plastic hinge formation at the interface of the crossbeam and longitudinal member, i.e the *stress-concentrator*. The inward pulling motion of the longitudinal member occurs at the non-impacted end as a result of the induced lateral forces. These forces are created by the local bending failure of the crossbeam and downward travel of the impactor. The skew lobe stacking of the impacted longitudinal member is also a result of the induced lateral forces. In all cases, the deformations of the bumper systems are stable and universal between the groups.

A favourable outcome is achieved with increased wall-thickness of the crossbeam and decreased crushing distance; demonstrating further potential for bumper systems to have higher capacity for energy absorption. An adverse outcome, however, is the increase in the mean crush force with the increase in wall-thickness. The mean crush force of the different bumper systems, listed in Table 3.2, shows an increase with a corresponding increase in wall-thickness of the crossbeam.

The presence of the through-hole discontinuities in the longitudinal members shows no significant difference in the deformation modes; however, the first lobe forms at an earlier stage suggesting a lower peak force is required to initiate progressive buckling [37]. This lower initial peak force is advantageous in energy absorbing structures. Consequently, the progressive buckling is more susceptible to other mechanisms involved in the behaviour of the bumper system. The pull-in motion generated by the bending crossbeam effected the symmetric stacking of the lobe formation. The longitudinal members show more instability in offset impact scenarios with discontinuities.

The behavioural response of the bumper system is consistent and repeatable in the 40% offset impact scenario. The experimental results are used to validate the finite element modelling.

4. Finite Element Model

4.1 Formulation of finite element model

The formulation of the simplified automotive bumper system model is discussed in detail for execution through the LS-Dyna R4.2.1 solver using a structured input deck. The input deck includes the element and nodal details of the geometries and necessary keywords describing the contact algorithms and boundary conditions applied. The validation of the model is accomplished by comparison with the experimental results and is discussed in section 4.3. The input deck and keywords are managed through LS-PrePost v3.1 which provides the facilities to build the finite element model and view the output. The technique and style of the input deck of the numerical model is in accordance with the recommendations proposed in the official LS-Dyna Keywords User's Manual [56]. In this section, key aspects are addressed in the development of the numerical model.

4.1.4 Geometry and element mesh properties

The numerical model, shown in Figure 4.1, replicates the experiments setup and dimensions. Half symmetry boundary conditions are applied on the Y-Z plane to reduce computational time. The components are discretised into a number of elements and are meshed with the default quadrilateral Belytschko-Lin-Tsay shell elements, that are computationally efficient for explicit calculations [57].

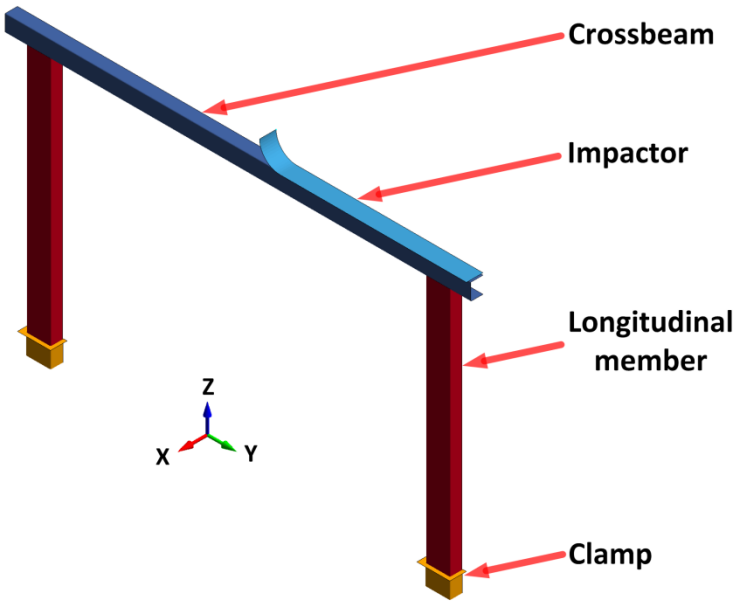

Figure 4.1: Finite element model setup of the bumper system (half symmetry)

Five integration points through thickness and one in-plane are chosen with a recommended shear factor of 0.833 [56, 57]; which scales the transverse shear stress. Hourglass control is based on the formulation of Belytschko and Tsay [56] using the Flanagan-Belytschko viscous form.

For the number of elements per part, Kokkula [47] uses 8,712 elements of size 5.0x5.0mm^2 for the longitudinal members and 9,577 elements of size 5.0x5.0mm^2 for in the respective bumper systems. In this study, separate sensitive crash simulations are carried out with varying element sizes for the longitudinal member and crossbeam to capture the appropriate deformation. The axial forces are used to test convergence of the varying sized elements. The longitudinal members are modelled with element sizes ranging from 2mm to 5mm. The details of the simulation results are summarised in Table 4.1.

Element Size (mm)	No. of Elements	Elapse Computational Time (*on 2 CPUs*)	Crush Distance (mm)	Peak Force (kN)	Mean Force (kN)	AVG Variation: 2.0mm	MAX Variation: 2.0mm
5.0	3 770	3h 11min	302.8	162.2	38.8	8.3%	14.9%
4.5	4 608	2h 40min	298.4	162.2	38.7	9.4%	20.9%
4.0	5 868	3h 19min	306.9	162.1	38.7	7.7%	18.6%
3.5	7 254	4h 41min	322.6	162.1	39.3	4.9%	12.7%
3.0	9 548	5h 59min	338.2	162.0	39.0	1.2%	5.8%
2.75	11328	4h 50min	340.8	161.9	38.8	0.6%	2.5%
2.5	13 520	7h 5min	338.9	161.9	38.8	0.6%	1.4%
2.0	19 825	10h 28min	341.8	161.9	38.8	-	-

Table 4.1: Summary of simulations of single longitudinal members with varying element sizes

The Peak crush force and Mean crush force are relatively constant with decreasing size of elements. However, the crush distance increases but converges around 340mm. The variation (*to the smallest element size of 2.0mm*) decrease rapidly after an element size of 3.5mm. The force comparison is shown in Figure 4.2, as moving average force vs. time of the varying element sizes. The element sizes 3.0mm, 2.75mm, 2.5mm and 2.0mm converge acceptably and the maximum relative error is below 10%. Consequently, the chosen element size for the longitudinal member is 2.75x2.75mm^2 as the computational time is similar to the larger element sizes with an average variation of 0.6% and a maximum variation of 2.5% compared to the smallest element size tested. A similar approach is carried out for the crossbeam and an element size of 5.0x5.0mm^2 is selected for accurate force/deformation results and efficient computational time.

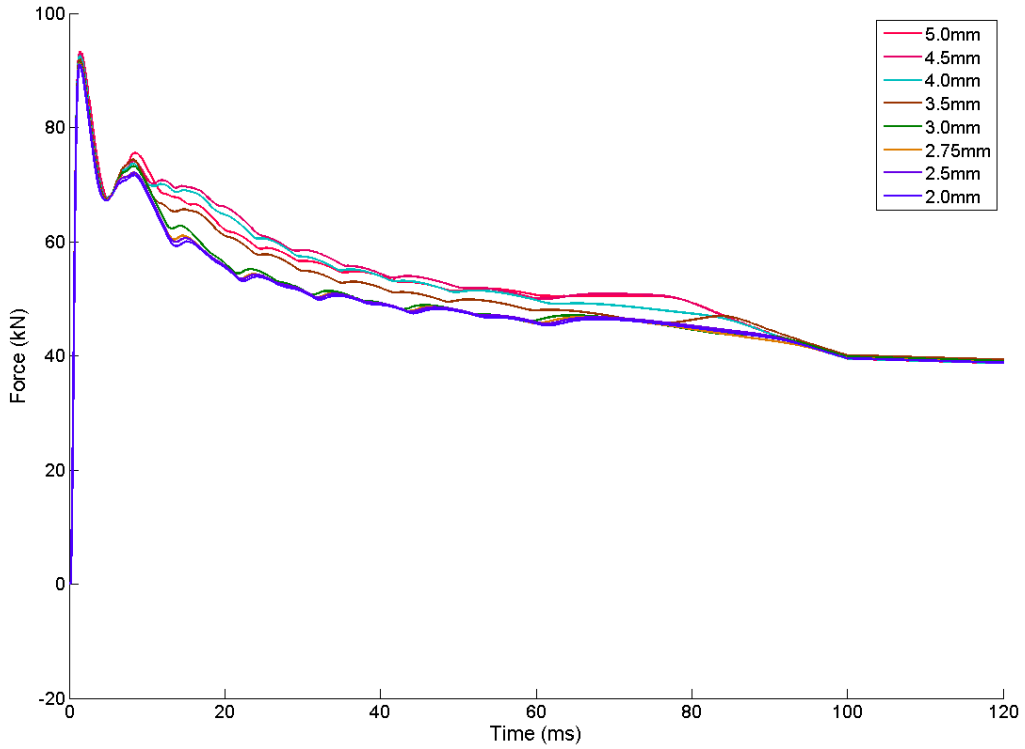

Figure 4.2: Moving average force vs time output of single longitudinal member with varying mesh size under impact load

Table 4.2 summarises the mesh details of the different components. The deformable components (crossbeam and longitudinal member) are modelled using the Simplified Johnson-Cook material model, discussed in section 4.2, and the non-deformable components (impactor and clamp) are modelled as rigid bodies.

Profile	No. of Elements	Approx. Element Size (mm^2)	Element Type	Material Model
Crossbeam	6 075	5.0 x 5.0	Shell	Johnson's Cook
Longitudinal member	11 328	2.75 x 2.75		
Impactor	16	-		Rigid body
Clamp	1 221	3.0 x 3.0		

Table 4.2: Mesh properties of bumper system components

The finite element (FE) bumper system is modelled using recommended keywords from the LS-Dyna library to best replicate the behaviour of the experimental setup. All simulations are executed with an initial time step of 0.001ms and a recommended scale factor of 0.9 [56, 57]. Axial force measurements and energy absorption is recorded at intervals of 0.01ms for later analysis and comparison of the geometric differences of the bumper systems.

4.1.5 Contact algorithms

In the bumper system model, various contact algorithms and boundary conditions are employed to ensure minimal penetration of parts and to avert any numerical instability. Four contact algorithms are applied in the numerical model and listed in Table 4.3 with the respective master and slave parts/surfaces.

Contact Algorithm Description	Master – to – Slave Part / Surface
Automatic Single Surface	All deformable parts (crossbeam & longitudinal members)
Automatic Surface to Surface	impactor – to – crossbeam
	crossbeam – to – longitudinal members
	longitudinal members – to – clamps
Tied nodes to surface	crossbeam – to – longitudinal members
Tied nodes to surface offset	Longitudinal members – to – clamps

Table 4.3: Details of contact algorithms per FE part

All the contact algorithms use the recommended static coefficient of friction value of 0.74 and dynamic coefficient of friction value of 0.57 for metallic materials [56]. The automatic single surface and surface-to-surface contact algorithms are selected to automatically adjust the parameters and allow the inside and outside walls of the various parts to be in contact whilst minimizing penetration with the application of penalty forces. Nodes in the slave part set are checked for contact with the parts in the master set. Figure 4.3 shows the contact algorithm of the upper edge nodes (slave) of the longitudinal member to the lower crossbeam surface (master). This constraint, *tied nodes to surface*, represents the welding region of the experimental bumper systems, which is not permitted to fail.

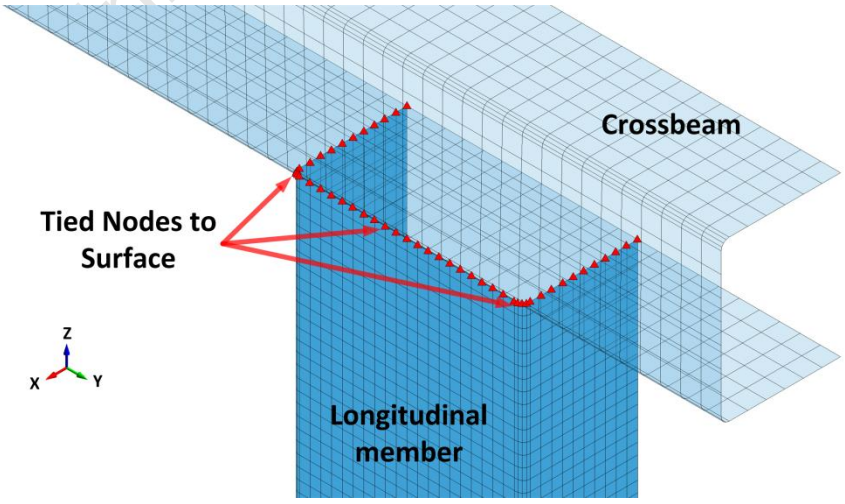

Figure 4.3: Tied nodes to surface contact between crossbeam and longitudinal member

The contact between the longitudinal members and the clamps is shown in Figure 4.4. The offset option is selected to accommodate the shell thickness of the clamp and longitudinal member, and to prevent initial penetration of the parts.

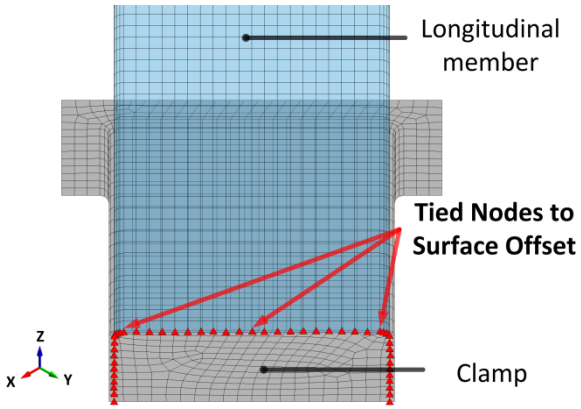

Figure 4.4: Tied nodes to surface offset contact between longitudinal members and clamps

4.1.6 Initial and boundary conditions

The respective mass of the impactor is applied to the finite element (FE) part as an elemental mass parameter in LS-Dyna with all nodes constrained in the X- and Y-axes; but not in the Z-axis to allow vertical motion of the rigid body representing the 'drop mass'. An initial velocity of 10m/s in the Z-axis is applied to all nodes. These initial conditions replicate the dynamic loading condition and mechanics of the dropping mass and impactor system in the experimental setup, shown in Figure 4.5. Gravitational load is applied to the impactor part.

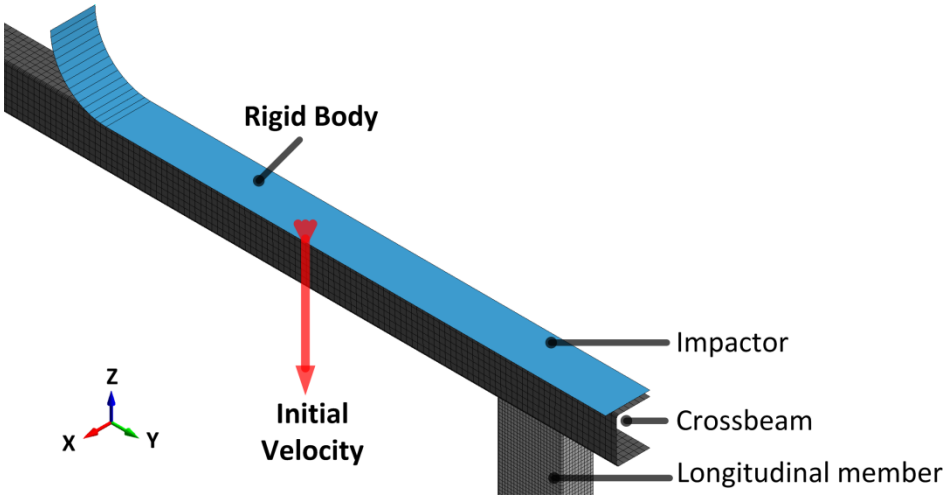

Figure 4.5: Initial velocity of impactor for dynamic loading condition

The bumper system, shown in Figure 4.6, is modelled using half symmetry in the Y-Z plane to improve computational time and the clamp end is restricted in all degrees of freedom, as it is defined as a complete rigid body.

.

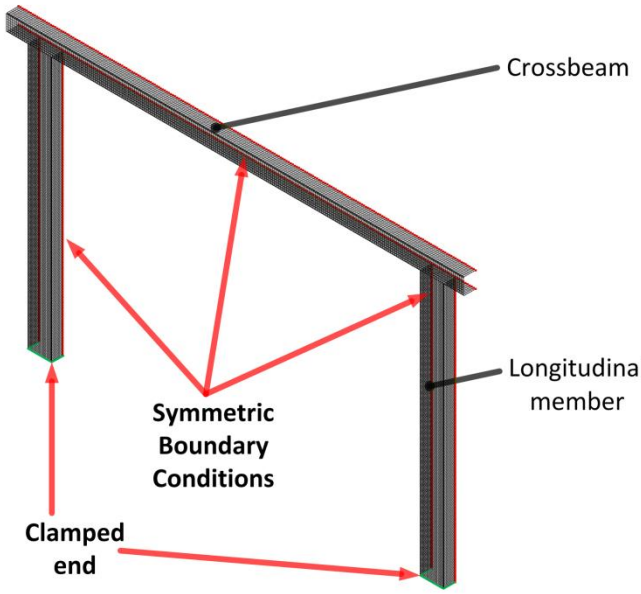

Figure 4.6: Symmetric boundary condition of FE bumper system

4.2 Material characterisation

One of the critical requirements of an accurate finite element model is the formulation of the appropriate material model. The ability of the material model being employed to replicate the behaviour of the material properties is paramount. A series of material tests are carried out experimentally under quasi-static and dynamic loading conditions to characterize the material behaviour. The data from these tests are used to characterize the constitutive Johnson-Cook material model [58] applied in the numerical simulation. This section describes the standard material testing conducted and the determination of the constitutive model parameters for each distinct tube profile.

4.2.4 Quasi-static tensile testing

Standard uniaxial tensile testing is conducted for the different tubular sections, see Table 4.4, namely the different square tubes and rectangular tube profiles. The tensile test specimens are extracted from the side-walls of the tubes using a CNC Milling machine; illustrated in Figure 4.7. From these tests material parameters, such as the yield strength, are determined.

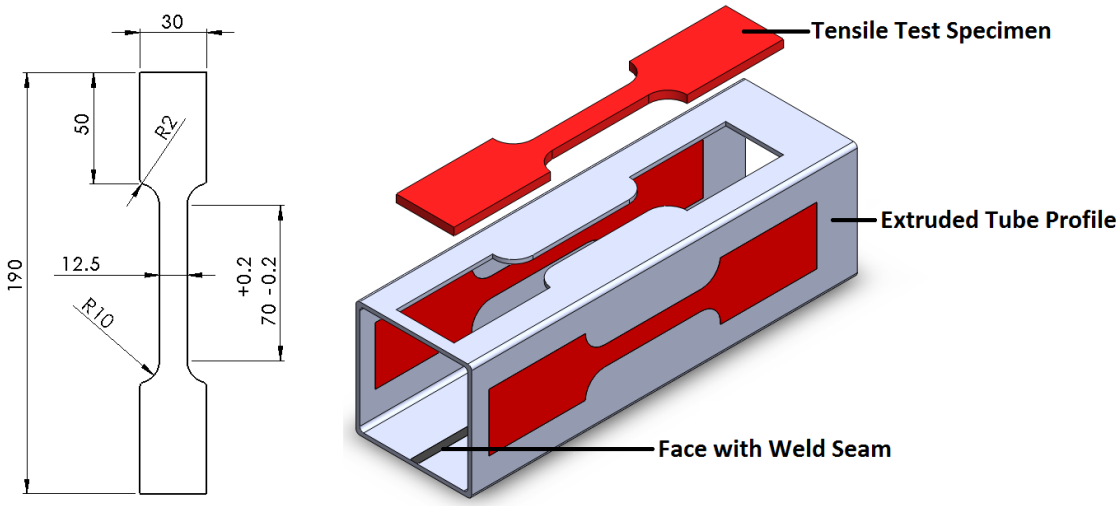

Figure 4.7: Tensile test specimen dimensions and extraction from the steel tube

Using a 200kN Zwick tensile test machine for the quasi-static tensile tests. The crosshead speeds (CHS) of the Zwick machine set at 1mm/min, 20mm/min, 50mm/min and 100min/mm, are equivalent to strain rates of $2.78\text{x}10^{-4}\text{s}^{-1}$, $5.56\text{x}10^{-3}\text{s}^{-1}$ and $2.78\text{x}10^{-2}\ \text{s}^{-1}$ for a gauge length of 60mm respectively.

The engineering stress σ_{eng} is calculated using the initial area, A_0, and the force measurement, F, determined from the Zwick machine.

$$\sigma_{eng} = \frac{F}{A_0} \tag{4.1}$$

The engineering strain ε is taken from the crosshead displacement measurement, ΔL, and the initial gauge length, L_0.

$$\varepsilon = \frac{\Delta L}{L_0} \tag{4.2}$$

The engineering stress-strain data from the quasi-static tests are shown in Figure 4.8 and Figure 4.9 for the rectangular 60x40x1.6mm and 60x40x3.0mm specimens respectively. In general, the results show good repeatability. For the 1.6mm test specimens, shown in Figure 4.8, the Yield Stress ranges from 347MPa to 368MPa and the strain at failure ranges from 0.28 to 0.36. For the 3.0mm tests, shown in Figure 4.9, the Yield Stress ranges from 424MPa to 453MPa and strain at failure ranges from 0.23 to 0.25.

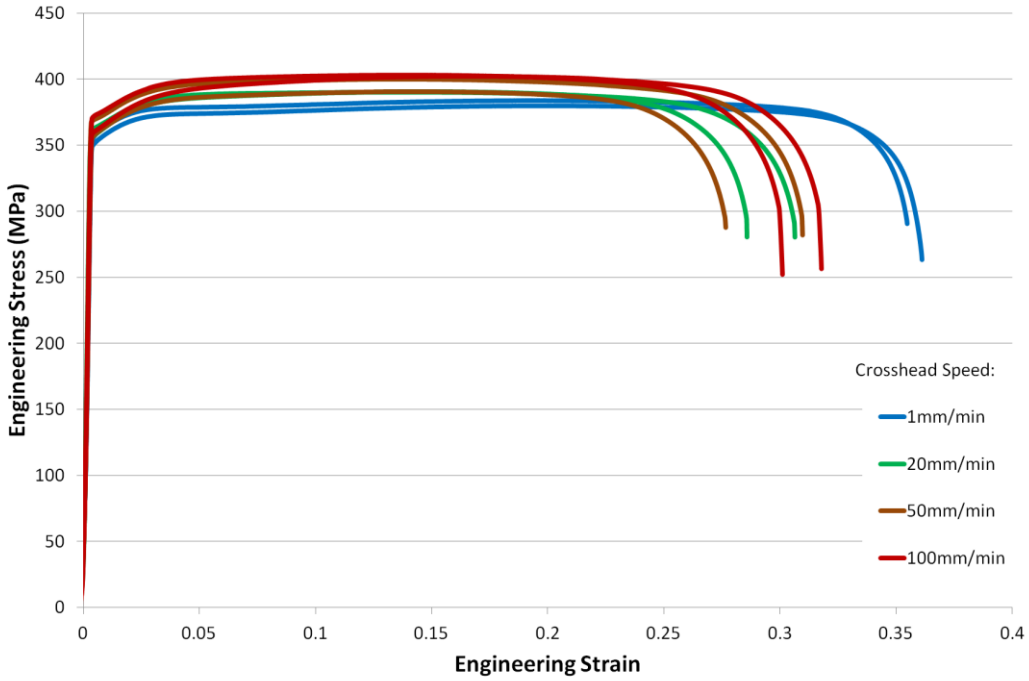

Figure 4.8: Quasi-static engineering stress-strain curves for tensile specimens cut from the 60x40x1.6mm extrusion profile

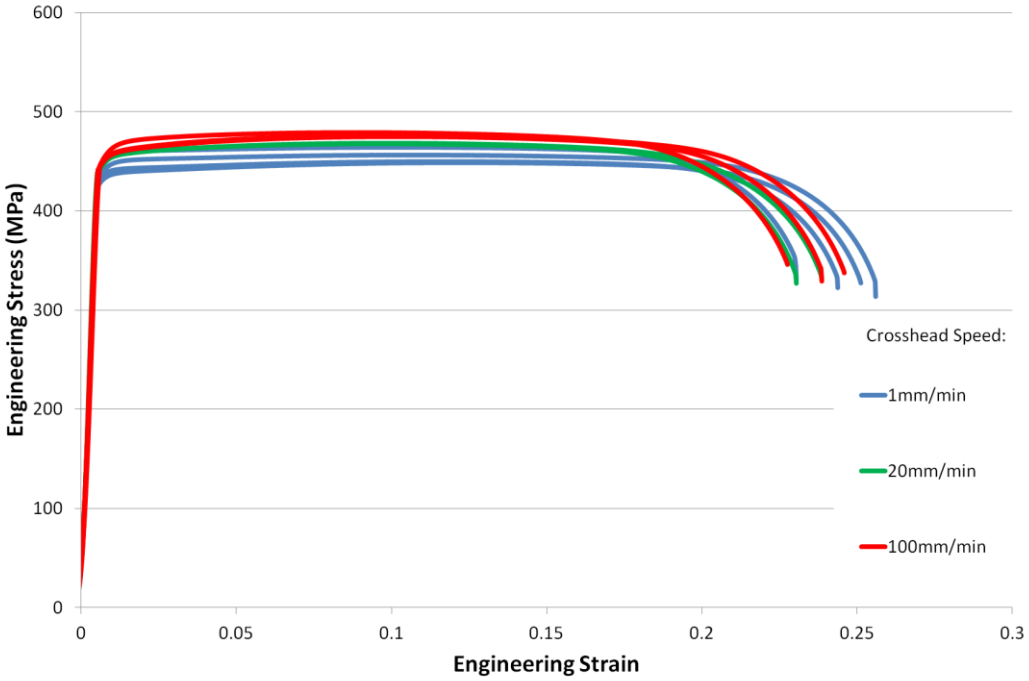

Figure 4.9: Quasi-static engineering stress-strain curves for tensile specimens cut from the 60x40x3.0mm extrusion profile

Generally, the tensile test specimens from the different tubes behave in a linear plastic material manner with a plateau region after the Yield Stress up to the point when necking occurs. The average engineering stress-strain curves for the four distinct tube profiles are shown in Figure 4.10. The responses from the tests of the square profile show some experimental variation as the specimens are extracted from three different tube stock lengths. The tensile specimens extracted from the square and rectangular 2.0mm tubes show more strain hardening in comparison to the 1.6 and 3mm specimens. Lüders bands are common in the tensile tests of the 2.0mm thick specimens. The average material properties for the individual tube profiles are summarised in Table 4.4.

Tube Profile and Thickness	Uniaxial Yield Stress (MPa)	Ultimate Tensile Strength (MPa)	Elongation Percentage at Breakage (%)
Rectangular @ 1.6mm	359.2	377.9	36.4
Rectangular @ 2.0mm	383.9	411.5	20.0
Rectangular @ 3.0mm	448.1	454.6	25.4
Square @ 2.0mm	352.7	405.2	33.3

Table 4.4: Summary of average material properties of the four distinct tube profiles

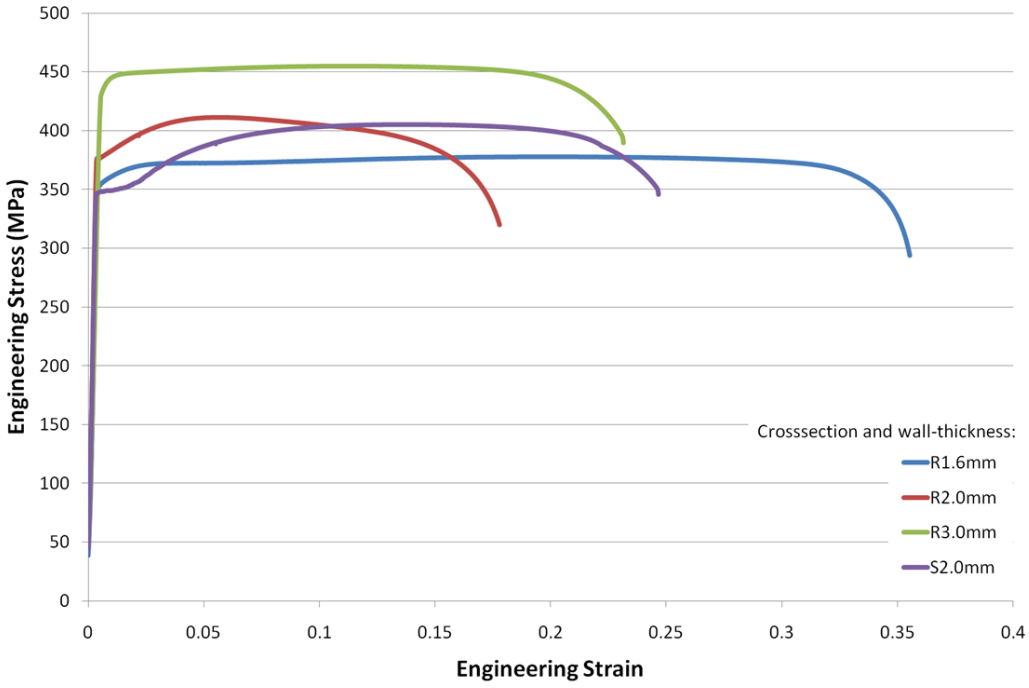

Figure 4.10: Quasi-static engineering stress-strain curves of the four distinct tube profiles

The Yield Stress is determined at the 0.2% offset intersection of the elastic-linear gradient as the majority of the results showed high ductility and no distinct point of yielding. True stress-plastic strain data are required to characterise the material accurately. The engineering stress-strain data use the constant initial area, A_0, assumption and not the instantaneous area, A_i, which is the true stress at that increment. The true stress is calculated from the engineering stress-strain data using equation 4.3 [59]:

$$\sigma_{true} = \frac{F}{A_i} = \frac{F}{A_0(A_0\ L_i)} = \sigma_{eng}\ \ \frac{L_i}{L_0}\ \ = \sigma_{eng}(1 + \varepsilon_{eng}^{pl}) \tag{4.3}$$

where σ_{true}: True stress L_i: Instantaneous gauge length

ε_{eng}^{pl}: Engineering plastic strain

For the plastic region, the logarithmic plastic strain is determined using equation 4.4 [59]:

$$\varepsilon_{ln}^{pl} = \ln(1 + \varepsilon_{eng}^{pl}) - {}^{\sigma_{true}}\!/_{E} \tag{4.4}$$

where ε_{ln}^{pl}: Logarithmic plastic strain E: Young's Modulus

Equations 4.3 and 4.4 are only valid up to the point of necking, the region where the strain can be assumed to be uniform over the gauge length. The point where necking is initiated is termed the Ultimate Tensile Strength (UTS). This is characterised by an increase in strain resulting from a decrease in axial load, known as the diffuse necking point. The average engineering stress-strain is taken from the entire set of tensile tests for each of the four tube profiles. The true stress-logarithmic plastic strain is calculated from the average engineering stress-strain data per group, up to the strain at UTS.

Figure 4.11 shows the material behaviour for the individual tube profiles, where '*R*' identifies *rectangular* cross-section and '*S*' the *square* cross-section. The curves show good linearity before the UTS point and are extrapolated further from the UTS up to the plastic strain where breakage of the uniaxial tensile test specimens occur. The curves from Figure 4.11 are used to determine the material model parameters under quasi-static conditions and are discussed in section 0.

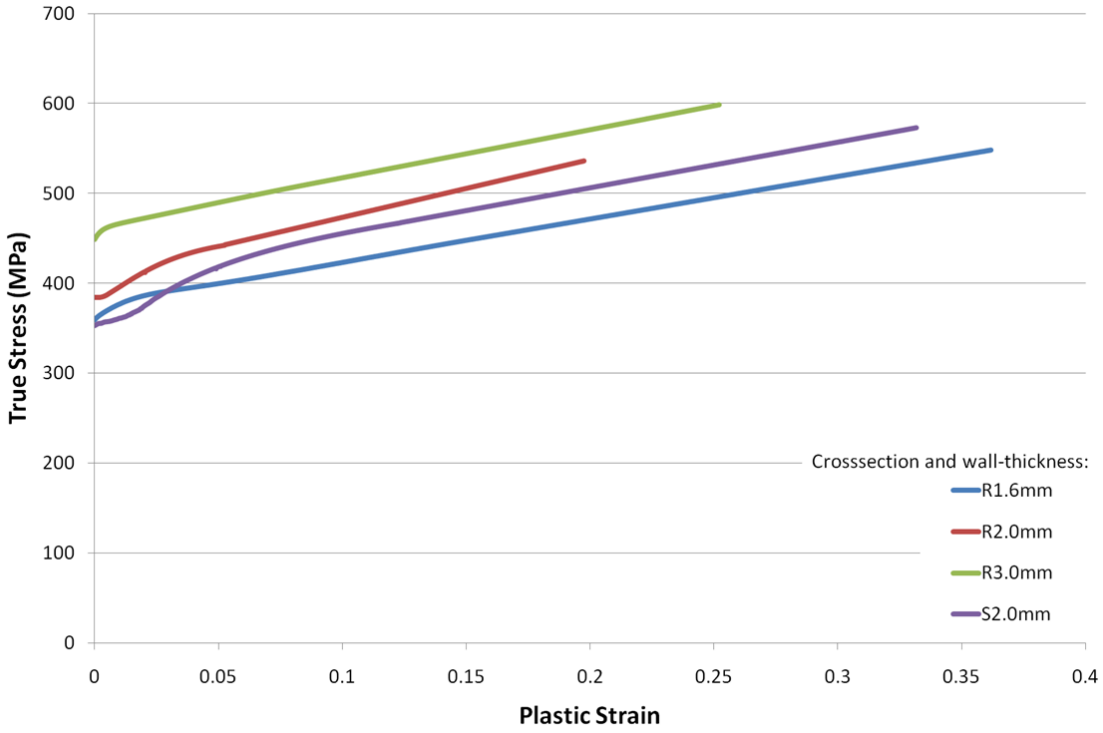

Figure 4.11: True stress-plastic strain curves from uniaxial tensile tests along the extrusion direction under quasi-static strain rates

4.2.5 Quasi-static and high strain-rate compression testing

Compression tests under quasi-static and dynamic conditions are performed to investigate the strain-rate sensitivity of the materials. The high strain rate test data also provides accurate data for the determination of the strain-rate parameter of the constitutive material model. For the compression tests, round discs of diameter 5mm are cut out of the side-walls of the rectangular 3.0mm thick and the square 2.0mm thick tube profiles. The flat surfaces of the specimens are finished with an 800µm grinding surface, to improve interface contact.

Quasi-static tests are carried out using the 200kN Zwick machine. The specimens are positioned between hardened blocks of a fine, flat finish. Adequate lubrication between the contact surfaces is applied to minimise barrelling of the specimen. The crosshead speed (CHS) of the Zwick is adjusted to replicate the same strain-rate in the tensile tests at a CHS of 1mm/min. The crosshead speed is thereby adjusted to 0.1mm/min for the 3.0mm thick specimens and 0.067mm/min for the 2.0mm thick specimens. The maximum displacement of the crosshead is set to 1mm and 0.67mm to allow maximum 25% percent strain of the specimen. The true stress-plastic strain curves of the quasi-static compression tests are shown in Figure 4.12. The 2.0mm thick specimens show far more strain hardening, steeper slope, and a lower Yield Stress, 345MPa, than 3.0mm, that yield at 390MPa.

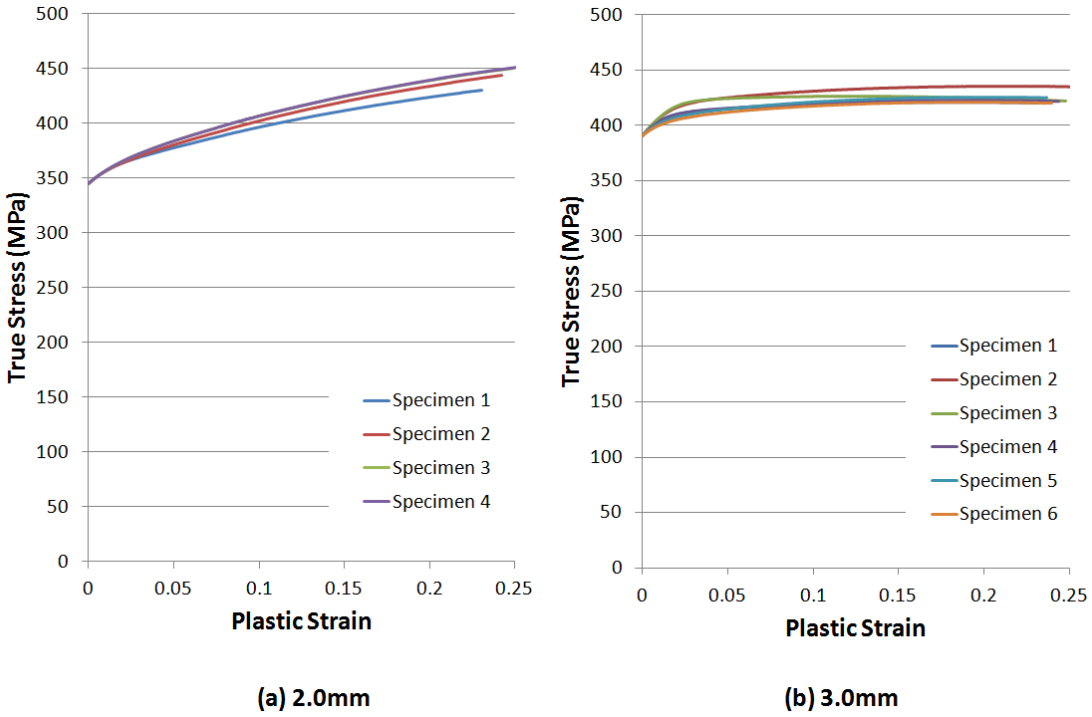

Figure 4.12: True stress-plastic strain curves from quasi-static compression tests of (a) 2.0mm and (b) 3.0mm thick specimens

The mechanical properties of steel vary with strain-rate, and the material model aims to replicate the dynamic behaviour as accurately as possible. High strain-rate compressive testing is conducted on a Split Hopkinson Pressure Bar (SHPB) to gain dynamic material behaviour at higher strain rates. Details and theory of the SHPB can be found in Marais [60].

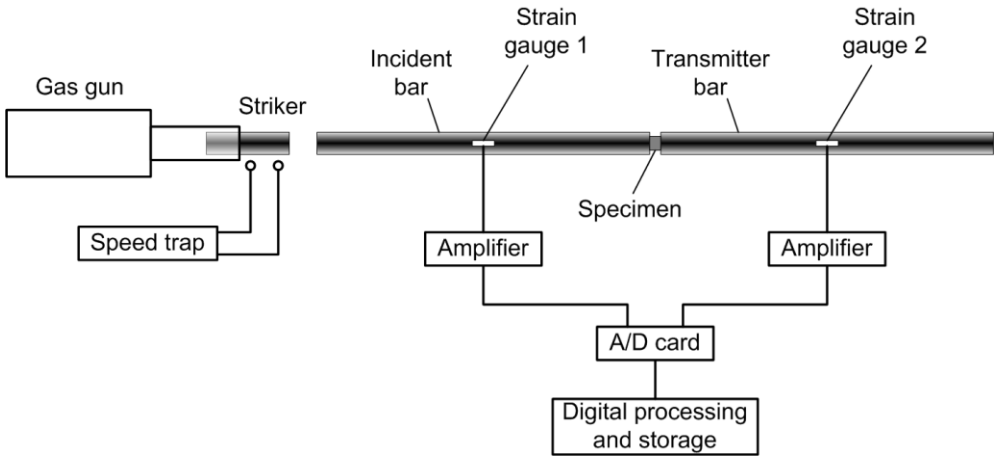

Figure 4.13: Schematic of the SHPB compression test setup [39]

The schematic of the test setup of the compression tests with a SHPB is shown in Figure 4.13. The gas gun is able to launch a striker at a specified velocity by adjusting the pressures in the barrel. The bars, incident and transmitter, and the striker are of similar diameter. The specimen is concentrically secured between the incident and transmitter bar with adequate lubrication to minimize barrelling. Strain gauges are placed on both bars from which the

voltages are recorded through an amplifier and connected to a PC for data acquisition. When the striker is launched, the stress waves in the incident and transmitter bars are recorded and analysed. The voltage signals are transformed to provide the stresses at both faces of the specimen.

A total of 21 tests are conducted with the SHPB. Fifteen of which are a thickness of 2.0mm. The other 6 specimens are of thickness 3.0mm, to investigate the strain rate behaviour of the rectangular 60x40x3.0mm tube profile as the material shows a far higher Yield Stress than the tube profiles.

A typical result from the SHPB for the 2.0mm thick specimen is shown in Figure 4.14 and for the 3.0mm thick specimen is shown in Figure 4.15. The Flow Stress of the 2.0mm specimen is at a relative constant stress of 650MPa. The maximum strain-rate experienced is $1457s^{-1}$; an order of $5x10^6$ larger in magnitude than to the quasi-static tests.

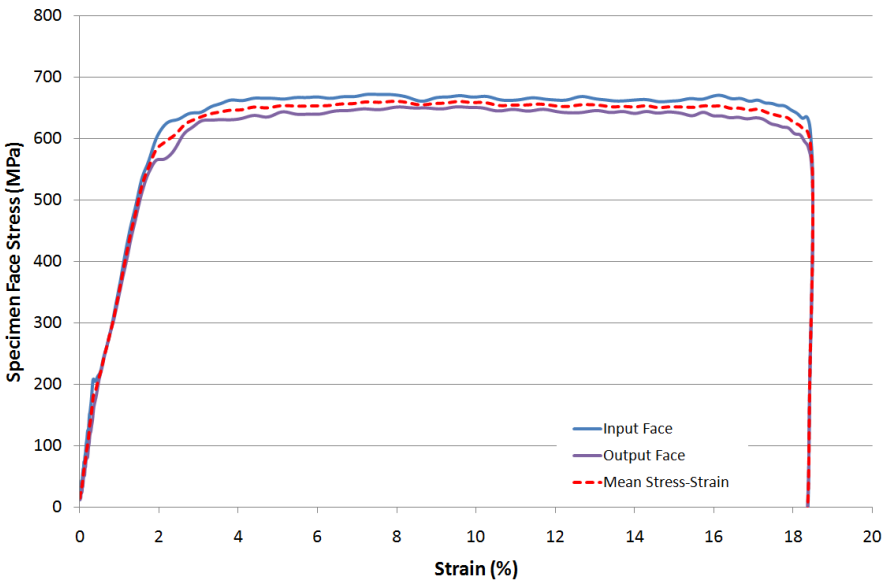

Figure 4.14: Stress-strain curve of a specimen 2.0mm thickness at high strain rates

Figures 4.15 and 4.16 show a typical stress-strain curve and strain-rate vs time obtained for 3.0mm thick specimen. The Flow Stress of the specimen is also relative constant at 670MPa. The maximum strain-rate achieved is $1807s^{-1}$; an order of $6.5x10^6$ larger in magnitude than the quasi-static tests. The strain-rate is not constant due to the thinness of the test specimens; thereby approximate plateau values are selected and averaged between the tests. The accumulative data at specific strains in the plastic region is used to determine the strain-rate parameter of the constitutive material model and is discussed in section 4.2.6. The data processing and analysis is performed using MATLAB code provided by Mr. R. Govender [61].

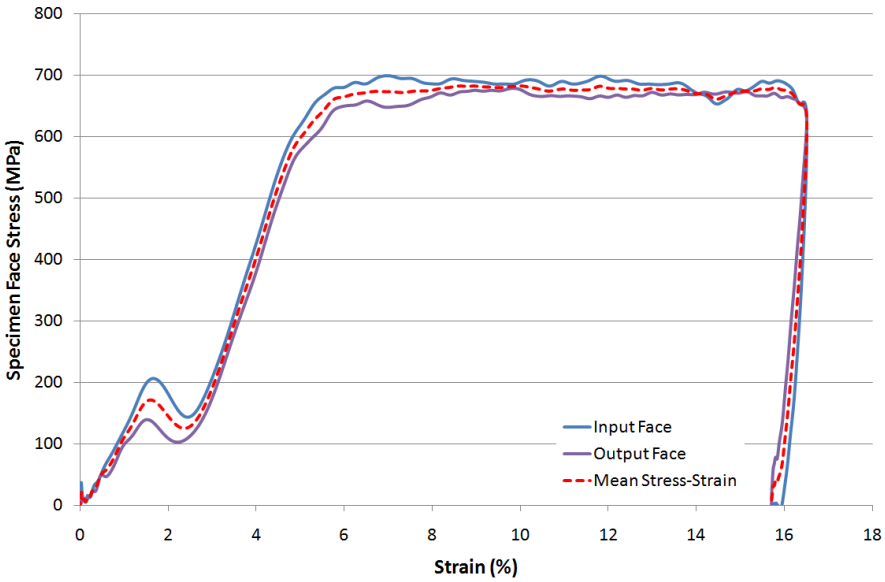

Figure 4.15: Stress-strain curve of a specimen 3.0mm thickness at high strain rates

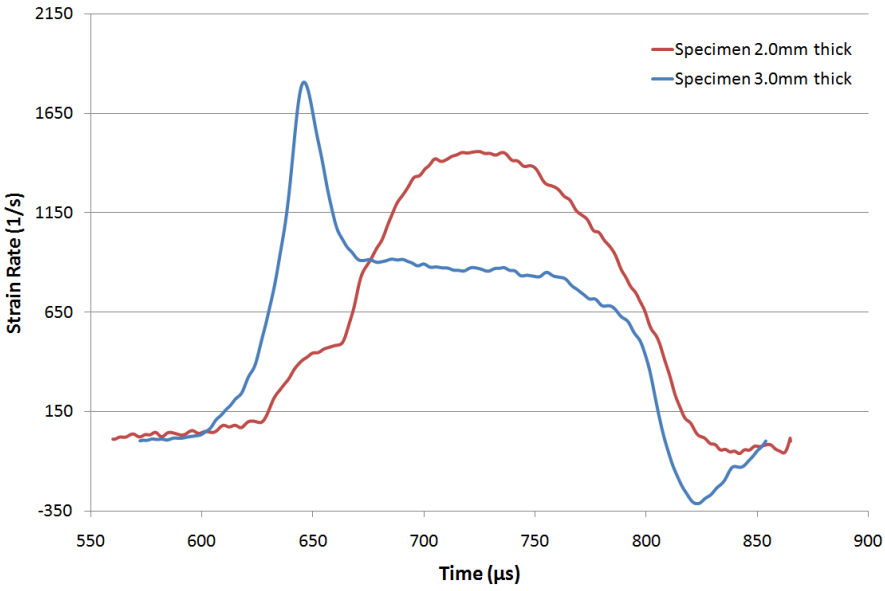

Figure 4.16: Strain-rate vs time plot of specimens of 2.0mm and 3.0mm thickness

4.2.6 Johnson-Cook material model

The Johnson-Cook constitutive material model [58] is incorporated throughout this study. The material model is chosen as it is one of the most widely used models because it takes on a simple, yet effective, form that includes strain hardening, strain-rate and temperature dependencies. The material model intended primarily for numerical computations is also available in most commercial finite element codes. The model is a phenomenological model, i.e. not based on traditional plasticity theory, that reproduces several important material responses observed in dynamic structural impact. The three primary material responses are strain hardening, strain-rate effects and thermal softening. The Johnson-Cook model accounts for these three material responses independently in a multiplicative manner. In the unmodified form, the Johnson-Cook model [58] is given by equation 4.5:

$$\sigma_f = \underbrace{A + B\varepsilon_p^n}_{\text{Strain Hardening}} \underbrace{1 + C\ ln\ \varepsilon^*}_{\text{Strain-rate Effects}} \underbrace{1 - T^{*\ m}}_{\text{Thermal Softening}} \tag{4.5}$$

where σ_f: Equivalent Flow Stress; A: Yield stress; B: Coefficient of strain hardening; ε_p: Equivalent plastic strain; n: Strain hardening exponent; C: Strain-rate hardening coefficient; ε^*: Normalized strain-rate; T^*: Homologous temperature; m: Thermal softening exponent

The model parameters A,B,C, n and m are the five material constants to be determined. The normalized strain-rate, ε^*, is the ratio of the equivalent plastic strain-rate, ε_p, to the reference strain-rate, ε_0, at which the parameters A,B and n are determined. The reference strain-rate describes the material behaviour under quasi-static conditions and is taken as the quasi-static tensile test strain-rate of 2.78e-04s^{-1}. The parameter *A* is the Yield Stress defined by the model as the Flow Stress at zero plastic strain and quasi-static loading condition. The strain hardening behaviour is represented by the parameters *B* and *n* using a power-law relationship with the equivalent plastic strain. The strain-rate dependence is represented by the parameter *C* and the natural-logarithm of the normalized strain-rate. The thermal softening is accounted for by the parameter *m* with the homologous temperature fraction. The homologous temperature, T^*, is expressed in equation 4.6:

$$T^* = \frac{T - T_R}{T_M - T_R} \tag{4.6}$$

Here *T* is the absolute temperature, T_M the melting temperature and T_R is the reference temperature at which parameters A, B and n are determined. The homologous temperature is 0 if the absolute temperature is less than the reference temperature and 1 if the absolute temperature is above the melting temperature.

More complex models exist where the dependencies are linked in an integral manner, but the Simplified Johnson-Cook model has been shown to be suitable for the modelling of large deformations in thin-walled structural problems. A very fast and efficient version of the Johnson-Cook, termed Simplified Johnson-Cook [57], material model is incorporated in the numerical modelling of this study. This model ignores the temperature dependence in the Flow Stress formulation.

Only four constants are then necessary to implement the Simplified Johnson-Cook material model. The data from the material tests, discussed in sections 4.2.4 and 4.2.5, are used to determine the four material parameters. The method proposed by Lin *et al*.[62] is used to determine *B*, *n* and *C*. The parameter *A*, Yield Stress, is taken from the uniaxial tensile tests data at the 0.2% offset intersect and are shown in Table 4.4.

- **Determination of parameter *B* and *n***

At the reference strain-rate, ε_0, and reference temperature, T_R, equation 4.5 is expressed in a simpler form:

$$\sigma_f = A + B\varepsilon_p^n \tag{4.7}$$

Taking the logarithm on both sides of equation 4.7 and rearranged to obtain equation 4.8 in the form of a linear polynomial *y=mx + c*. Substituting the values of the equivalent Flow Stress and plastic strains from the uniaxial tensile tests gives the relationship between $ln\ \sigma_f - A$ and $ln\varepsilon_p$. From Figure 4.17 the values of *B* and *n* can be determined from the gradient and y-axis intercept of the fitting line respectively. For the rectangular tube profile of thickness 3.0mm, the values of *B* and *n* are 242.13 MPa and 0.578 respectively. The values of the other profiles are summarised in Table 4.5.

$$ln\ \sigma_f - A = n\, ln\varepsilon_p + lnB \tag{4.8}$$

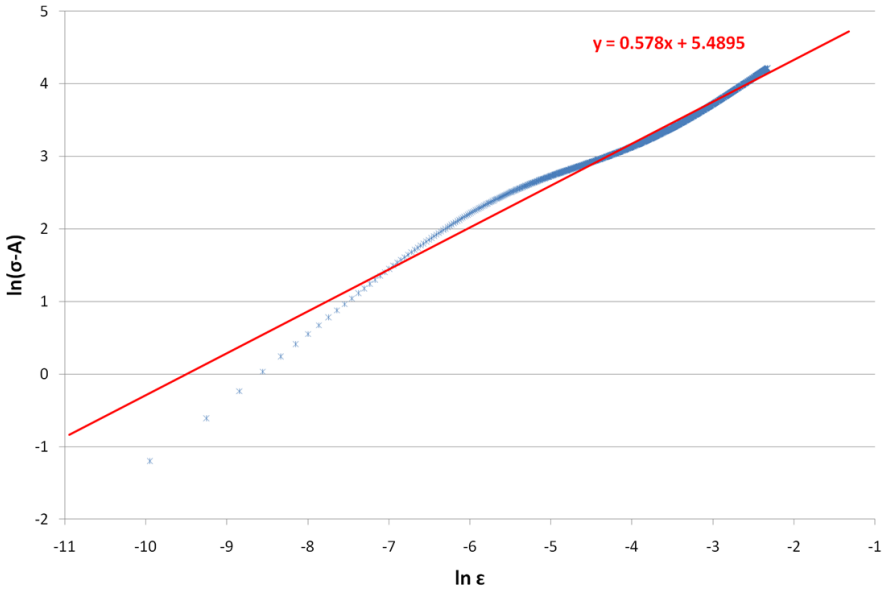

Figure 4.17: Relationship between ln(σ-A) and lnε from uniaxial quasi-static tensile test data of the rectangular tube profile of 3.0mm wall-thickness

- **Determination of parameter *C***

The strain-rate hardening coefficient, *C*, is determined at the reference temperature at which equation 4.5 is simplified and rearranged to equation 4.9:

$$\frac{\sigma_f}{A + B\varepsilon_p^n} - 1 = C \ ln \ \varepsilon^* \tag{4.9}$$

The relationship of equation 4.9 can be obtained by selecting discrete true strain points in the plastic region from the compressive tests under quasi-static and dynamic conditions. The model parameter C can then be evaluated by a linear fitting method. Two values of parameter *C* are determined: One relating to the rectangular tube profile of thickness 3.0mm and the other to the square tube profile of thickness 2.0mm. The data from the compressive tests discussed in section 4.2.5 are used. The linear trend lines in Figures 4.18 and 4.19 indicate that the parameter *C*, the gradient of the line, values are 0.0433 for the square tube profile material and 0.0299 for the rectangular tube profile. The scatter in Figures 4.18 and 4.19 could be as a result of impurities or bad finish on the surface of the specimen. The pre-stress in the manufacturing of the extrusions could account for the scatter as well.

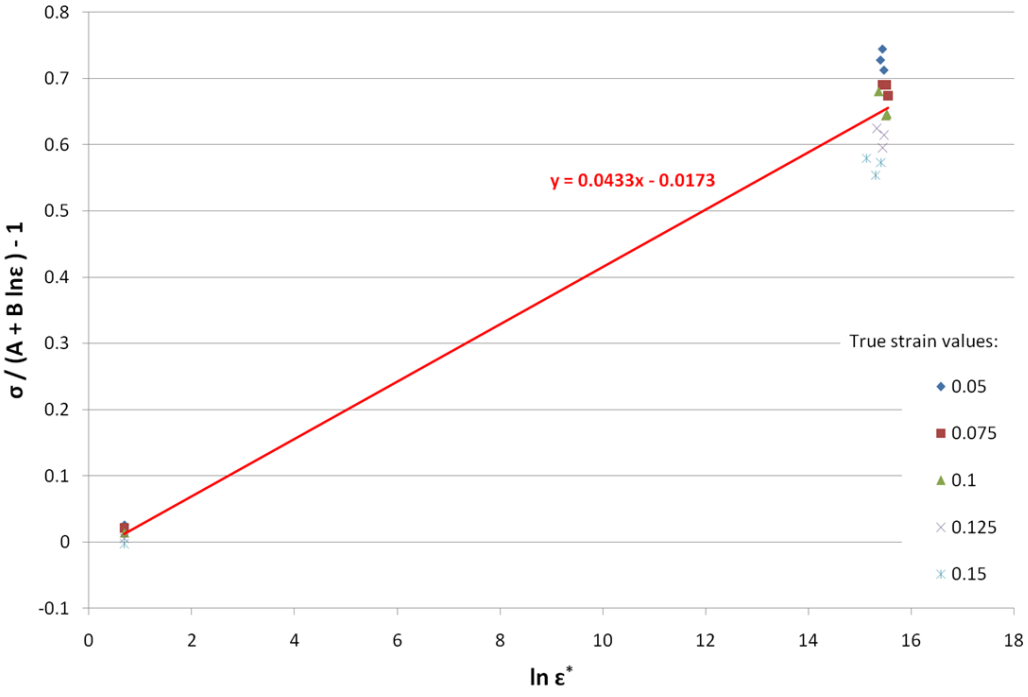

Figure 4.18: Relationship between σ/(A+Blnε)-1 and ln$\dot{\varepsilon}$ from compressive test data of the square tube profile of 2.0mm wall-thickness

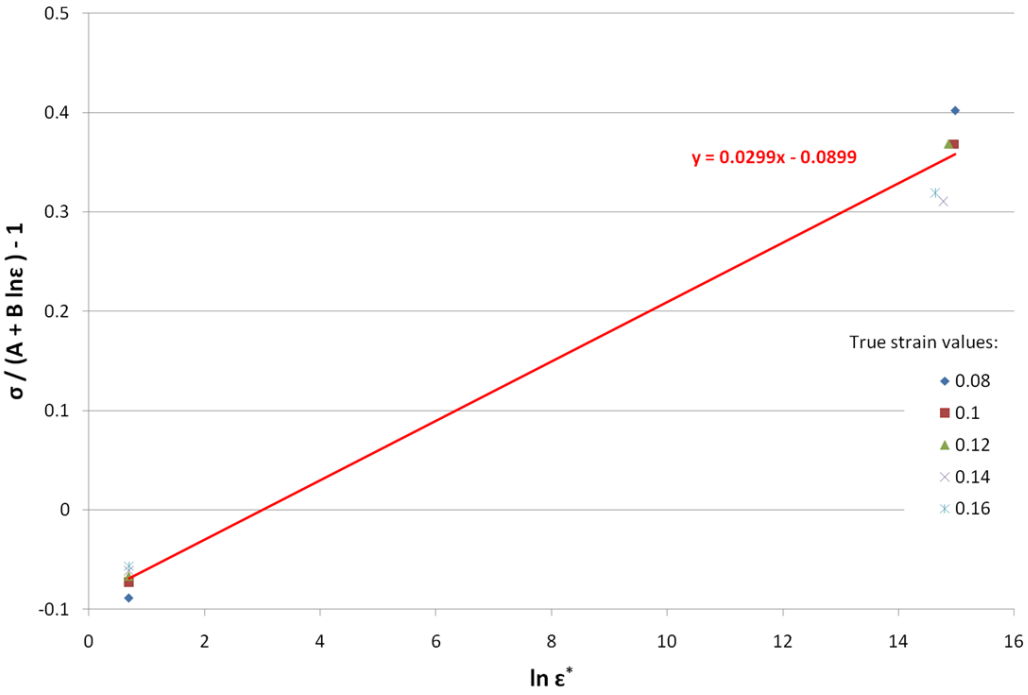

Figure 4.19: Relationship between σ/(A+Blnε)-1 and ln$\dot{\varepsilon}$ from compressive test data of the rectangular tube profile of 3.0mm wall-thickness

- **Simplified Johnson-Cook Material Models**

The values for the four model parameters are summarised in Table 4.5. The square and rectangular tube profiles of thickness 2.0mm show far more strain hardening and subsequently higher *B* and *n* values. The values of *C* are chosen for the non-tested rectangular profiles, 1.6mm and 2.0mm wall-thickness, as the stress-strain profiles are comparable to the two profiles that were tested. Namely the rectangular tube profile of 2.0mm wall-thickness has a similar hardening profile to the square tube profile material, and the rectangular tube profiles of thicknesses 1.6mm and 3.0mm share a similar stress-strain profile as well.

Tube Profile and Thickness	A (MPa)	B (MPa)	n	C
Rectangular @ 1.6mm	359.2	283.1	0.6306	0.0299
Rectangular @ 2.0mm	383.9	586.5	0.7647	0.0433
Rectangular @ 3.0mm	448.1	242.1	0.5780	0.0299
Square @ 2.0mm	352.7	1113.8	1.0012	0.0433

Table 4.5: Summary of the Simplified Johnson-Cook material model parameters of the four distinct tube profiles

The investigation of this study does not incorporate failure models. Therefore, no critical failure strain is defined in the material model. The Simplified Johnson-Cook models with the final selected parameter values are shown in Figure 4.20 up to a plastic strain of 25%.

The Simplified Johnson-Cook material models are incorporated in the numerical modelling formulation using LS-Dyna *MAT database. The material model is internally defined as *MAT_098 keyword and the four parameters *A,B,n* and *C* are defined according to the distinct tube profile.

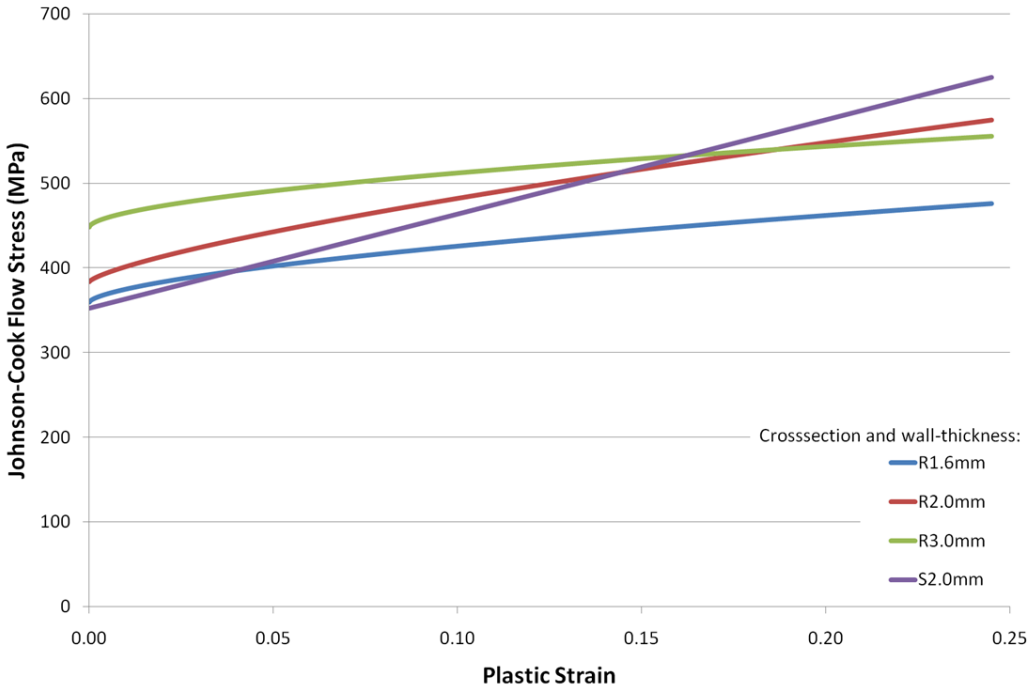

Figure 4.20: Johnson-Cook Flow Stress vs plastic strain of the models characterised for the four distinct tube profiles under quasi-static load condition

4.3 Results of finite element simulations

The numerical model is validated by comparing the critical deformation mode, crush distance and flex point height with the experimental results.

4.3.4 Deformation mode of impacted longitudinal member

The number of lobes formed in the experiments and numerical model shows exceptional correlation. The number of lobes obtained from finite element simulation are compared with the experiments in Table 4.6. The stacking of the tube arrangement is not as skewed in the numerical results compared to the experimental results because the numerical boundary conditions represent a 100% symmetric environment with the load evenly distributed. The experimental trolley-impactor arrangement could account for slight transverse loading to produce the skewed stacking of the lobes.

The results of number of lobes formed are listed in Table 4.6.; where * indicates a half-to-nearly completed lobe is formed.

Bumper System ID:	Experiments	Numerical Simulations
B1-301	4*	5
B1-396	6	6
B1-491	9	9
B2-301	4*	4
B2-396	5*	6
B2-491	8	7*
B3-301	4	5
B3-396	6	6*
B3-491	8	8*
BD3-301	5	5
BD3-396	7	7
BD3-491	8	8*

Table 4.6: Summary of number of lobes formed in experimental and numerical model bumper systems

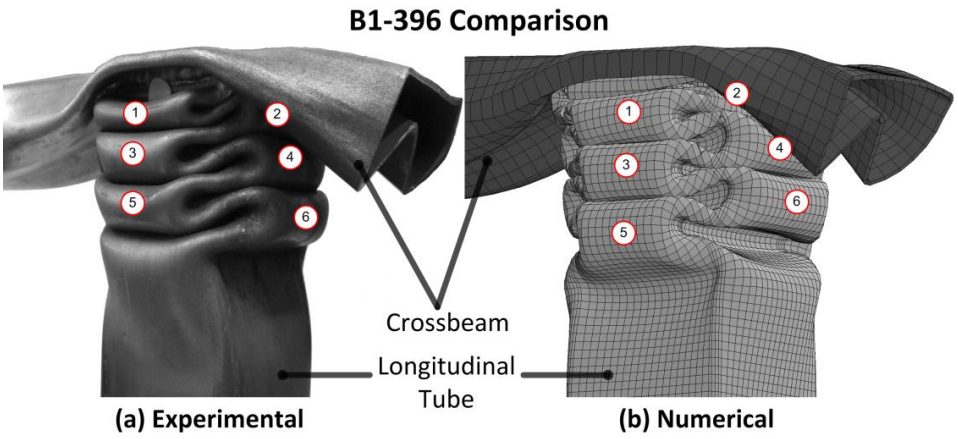

Figure 4.21: Comparison between experimental and numerical prediction of the B1-396 deformed longitudinal member

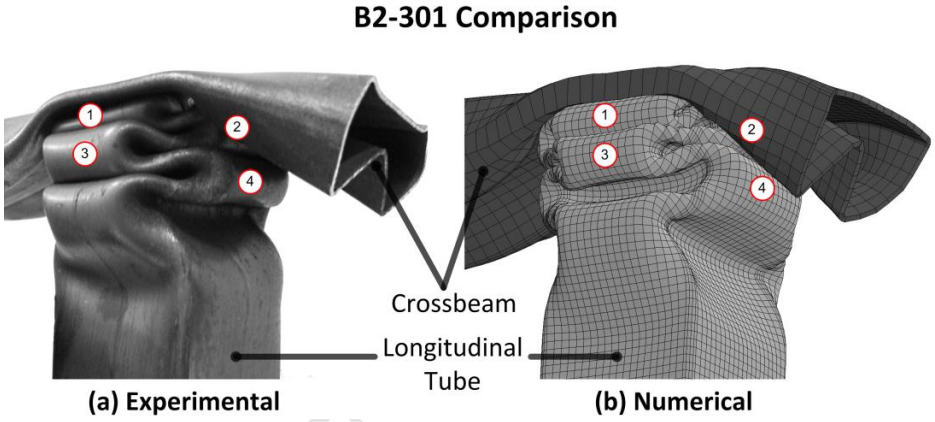

Figure 4.22: Comparison between experimental and numerical prediction of the B2-301deformed longitudinal member

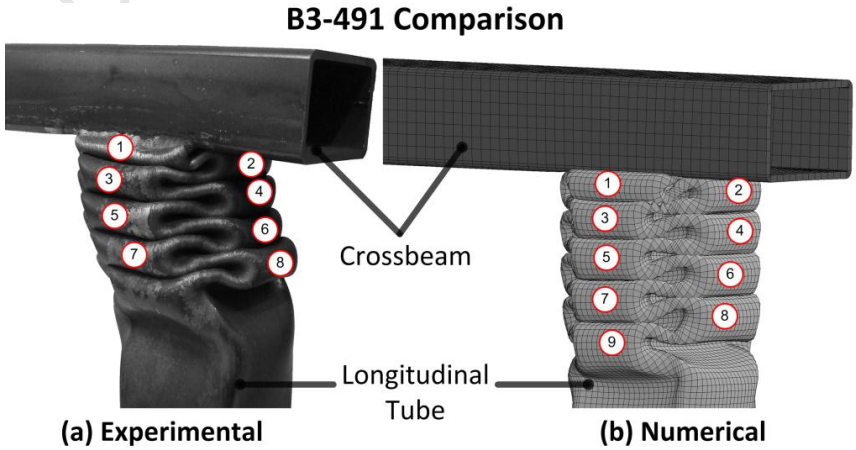

Figure 4.23: : Comparison between experimental and numerical prediction of the B3-491 deformed longitudinal member

4.3.5 Crush distance and flex point height

Generally, the correlation of the crush distance measurements and calculations is very agreeable. The crush distance at the impacted end of the bumper system is summarised in Table 4.7 for the experimental and numerical results. The numerical model in the thin-walled systems predicts the experimental crush distance with a relative error of less than 10%. The B1 and B2 system with a drop mass of 491kg under predicts the experimental results by 4.4% and 6%; showing very good correlation. The numerical model for the thicker-walled bumper systems over predict the crush distance by up to 21.9%.

Bumper System ID:	Experimental Crush Distance (mm):	Numerical Model Crush Distance (mm):	Absolute Relative Error (%):
B1-301	151	156.1	3.4
B1-396	207	205.4	0.8
B1-491	281	268.5	4.4
B2-301	147	147.3	0.2
B2-396	183	197.9	8.1
B2-491	268	252.0	6.0
B3-301	124	140.6	13.4
B3-396	168	188.7	12.3
B3-491	225	236.0	4.9
BD3-301	115	140.2	21.9
BD3-396	165	192.0	16.4
BD3-491	213	237.7	11.6

Table 4.7: Summary of crush distance from experimental and numerical model bumper systems

The measurements and calculations of the flex-point height are summarised in Table 4.8. The numerical model for the thin-wall bumper system show better correlation with the experiments (with a maximum error of 4.4%) than the numerical for the thick wall bumper system.

The thin-walled bumper system results show very good correlation. The numerical results show the model performs better with a higher increase in drop mass; where plastic deformation is more prevalent. The average crush distance error improves with an increase in drop mass and the average flex-point height error improves slightly. The crush distances are compared in Figure 4.24.

Bumper System ID:	Experimental Crush Distance (mm):	Numerical Model Crush Distance (mm):	Absolute Relative Error (%):
B1-301	544	525.6	3.4
B1-396	478	470.1	1.7
B1-491	410	414.5	1.1
B2-301	557	543.9	2.4
B2-396	515	492.1	4.4
B2-491	429	434.5	1.3
B3-301	592	550.5	7.0
B3-396	548	504.1	8.0
B3-491	493	457	7.3
BD3-301	604	548.9	9.1
BD3-396	557	497.8	10.6
BD3-491	506	456	9.9

Table 4.8: Summary of flex-point height in experimental and numerical model bumper systems

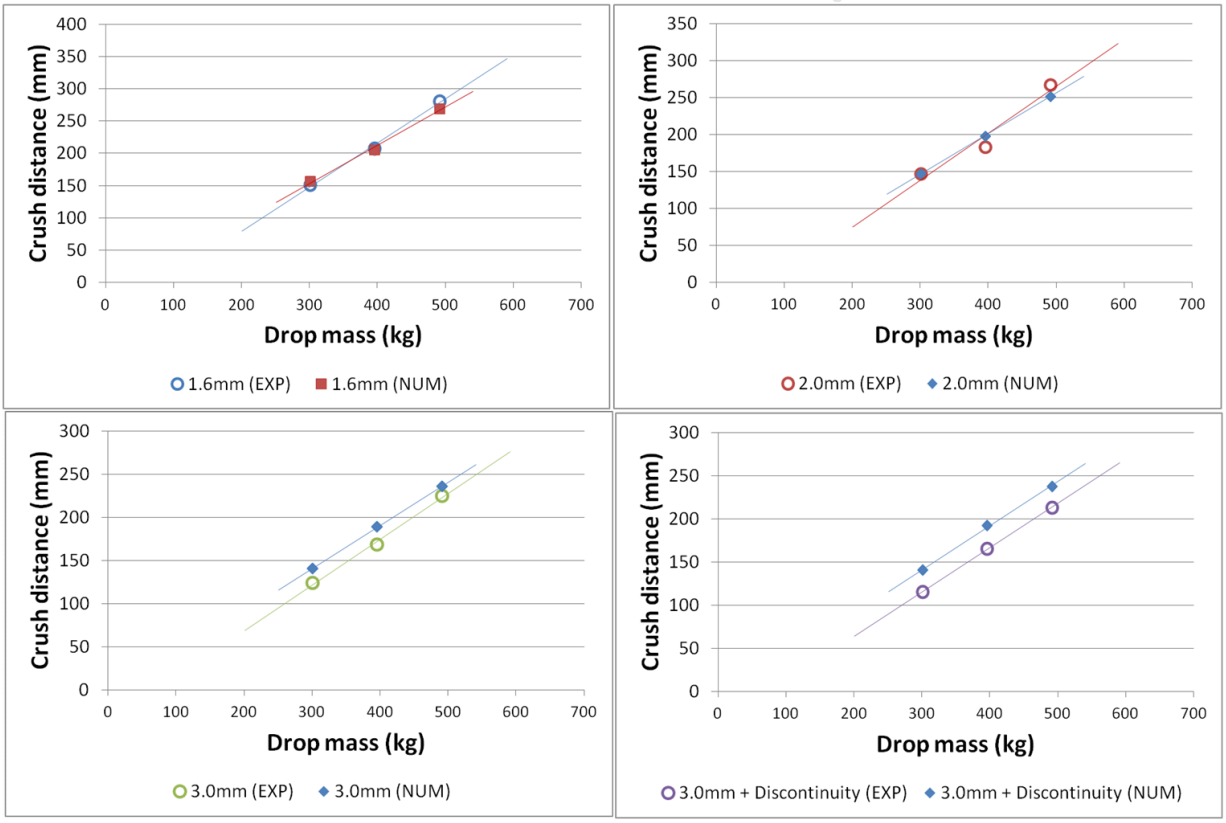

Figure 4.24: Comparison of crush distance results of experiments and numerical simulations

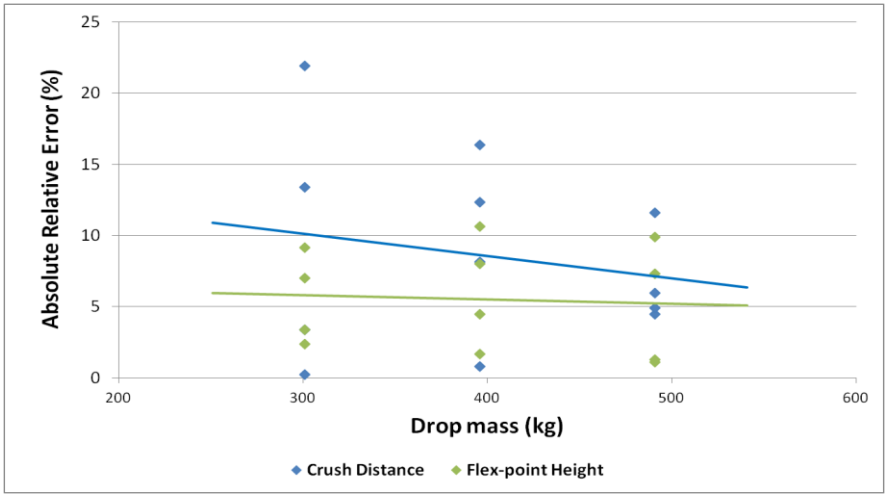

Figure 4.25: Absolute relative error of measurement comparison vs drop mass

4.3.6 Axial force calculation at impacted end

The axial force at the impacted longitudinal member is calculated and recorded in the numerical simulations. A low pass filter with a 600Hz cut-off frequency is applied to the force histories in conjunction with a 50 point smoothing moving average algorithm. The numerical models of the experimental work consist of 4 groups each having three different drop masses. The three **B1** axial force-displacement results are shown in Figure 4.26. The axial force-displacement profile show a distinct initial local peak representing the collapse of the crossbeam by lateral flattening. Thereafter a global peak force indicating the initiation of progressive buckling of the longitudinal member followed by a repetitive cyclic force indicating lobe formation is observed. No difference apart from the overall crush distance, i.e. displacement, is observed with the increase in the drop mass from 301kg to 491kg. The axial force-displacement profiles for groups **B2**, **B3** and **BD3** are found in *Appendix D* having similar behaviour, where the axial force-displacement profiles do not vary with drop mass apart from displacement.

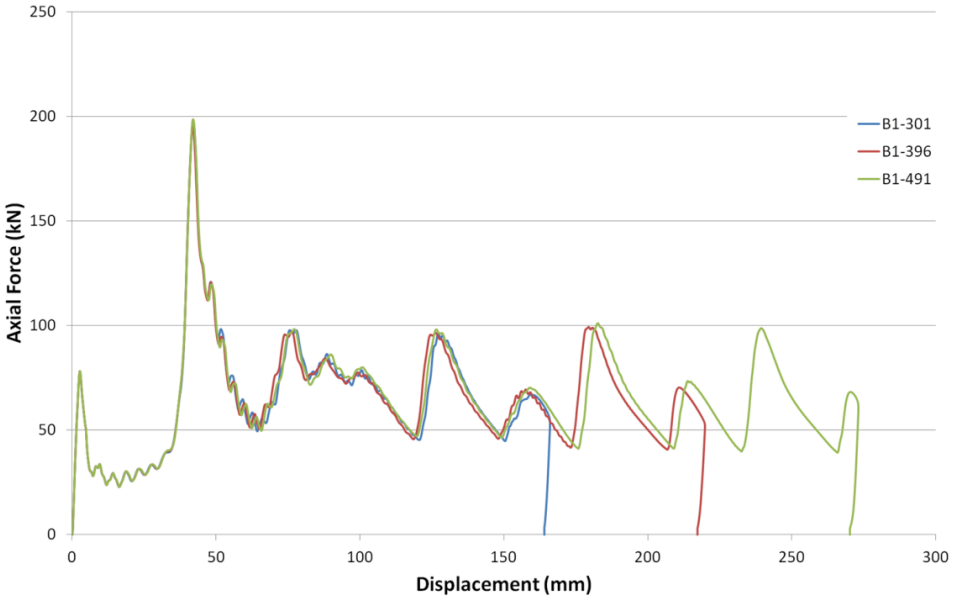

Figure 4.26: Axial force-displacement graph of B1 group numerical models at impacted end

One sample per group (**B1**, **B2**, **B3** and **BD3**) is plotted in Figure 4.27. The different wall-thicknesses of the crossbeam show clear distinction in the axial force-displacement calculations. The two thin-walled bumper systems, **B1** and **B2** respectively, show an initial local peak force representing the collapse of the crossbeam before the progressive buckling of the impacted longitudinal member commences. The thick-walled bumper systems, **B3** and **BD3** respectively, show the same profile with a high peak force. It is observed that the increase in the wall-thickness of the crossbeam increases the magnitude of the local and global peak forces. The axial force-displacement profiles are discussed in further detail in section 5.4.8.

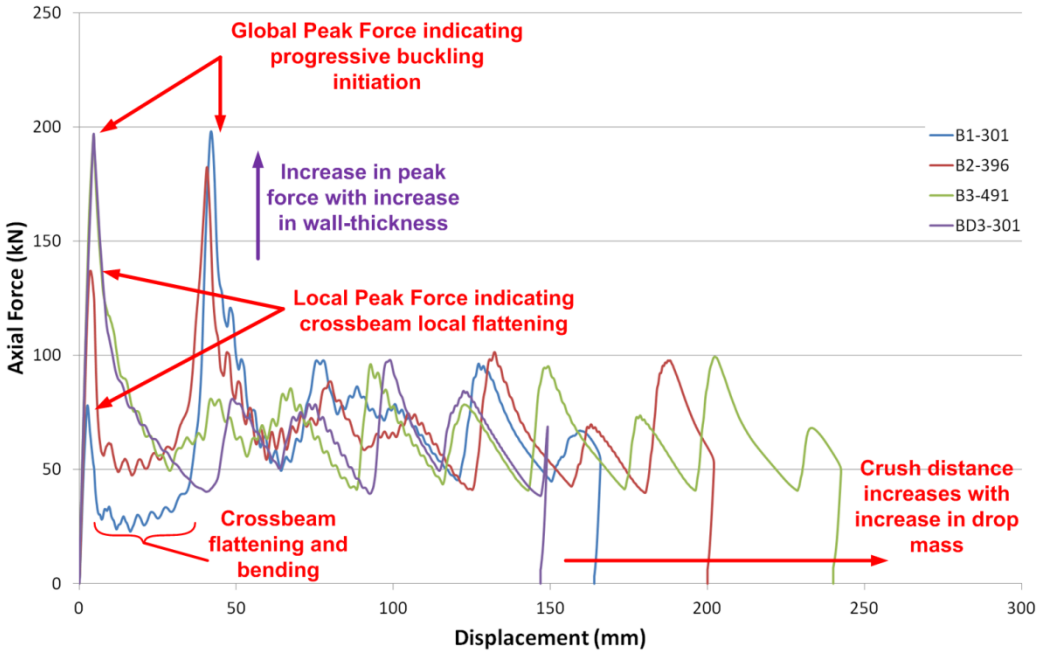

Figure 4.27: Axial force-displacement graph of numerical model at impacted end

4.3.7 Comparison of transient response of experiments and numerical simulations

The numerical model used predicts the transient behaviour of the experiments exceptionally. The high-speed camera footage of specific times during the deformation, from section 3.3.2, is compared to the numerical simulation results from the validation models. In the two thin-walled examples **B1-396** and **B2-396,** shown in Figures 4.28 and 4.29, the deformation onset time for the collapse of the crossbeam is well predicted by the numerical model. In both thin-walled bumper systems the crossbeam is fully collapsed at around 5ms. The first fully developed lobes occur at a time of approximately 9ms and in both cases the numerical model predicts the experimental results satisfactorily. In the experimental and numerical results the bumper system is fully deformed at around 45ms.

The transient response of thick-walled bumper systems, namely **B3-396** and **BD3-396** are shown in Figures 4.30 and 4.31. The numerical model predicts the **B3-396** bumper system very favourably and timely, but the deformation of the first lobe is slightly more prominent and the fully crushed stage show less lobe compaction than the experimental result. The **BD3-396** numerical model only predicts the experimental results acceptably. The time of the key stages are of similar degree but the location of the deformation is different. In experiments, the repeatability of the location of lobe formation and initiation is indefinite. In the **BD3** experimental results the lobes are formed between the two discontinuities whereas in the numerical model the lobe forms at the top of the impacted longitudinal member. However the number of lobes and crush distance correlate to an agreeable level.

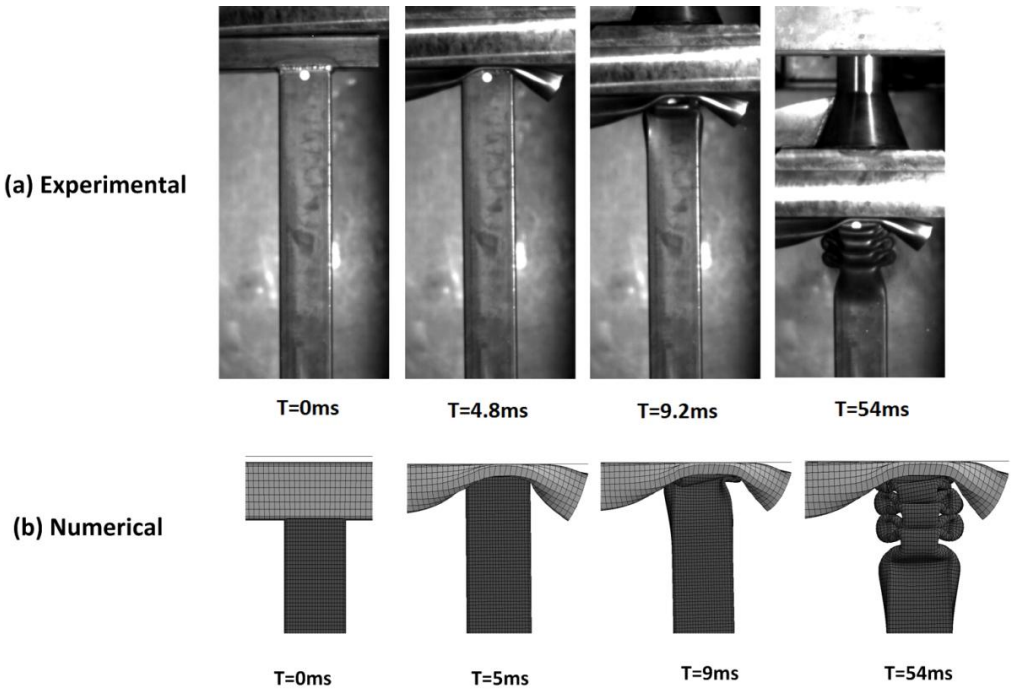

Figure 4.28: Transient response of impacted end of the B1-396 bumper system from (a) experimental and (b) numerical results

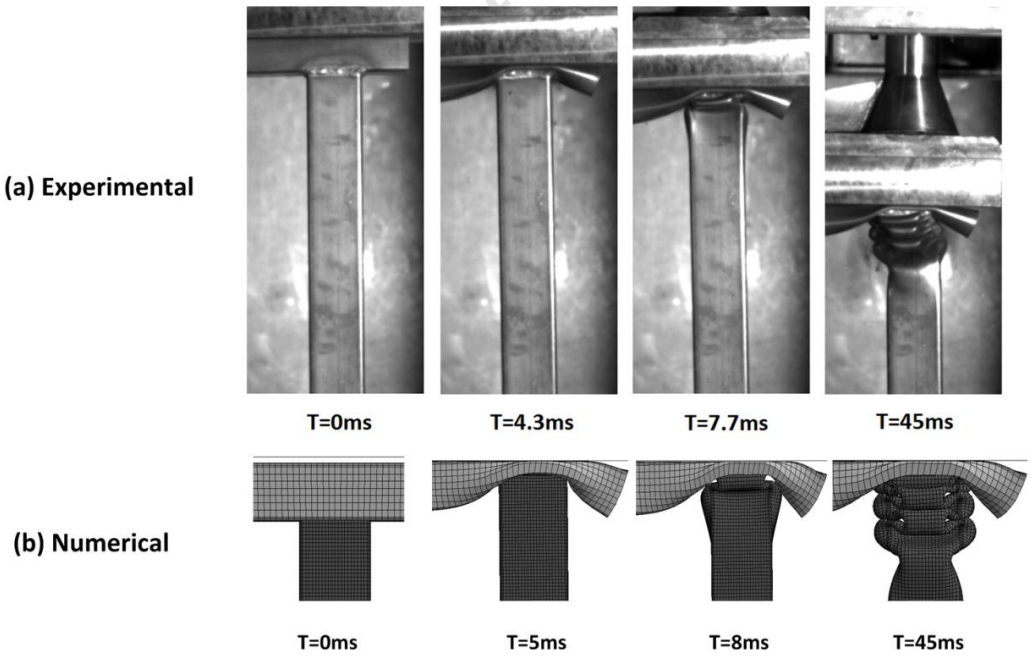

Figure 4.29: Transient response of impacted end of the B2-396 bumper system from (a) experimental and (b) numerical results

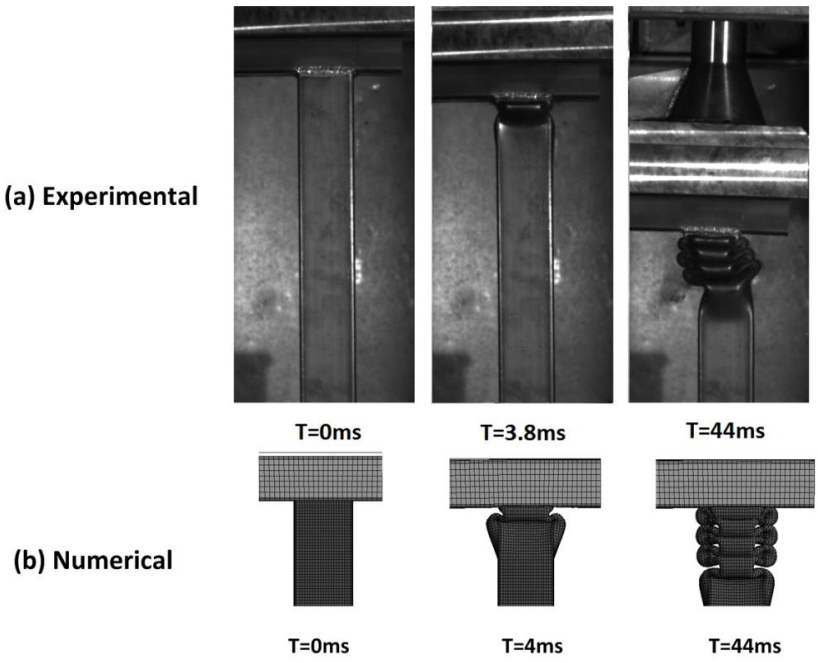

Figure 4.30: Transient response of impacted end of the B3-396 bumper system from (a) experimental and (b) numerical results

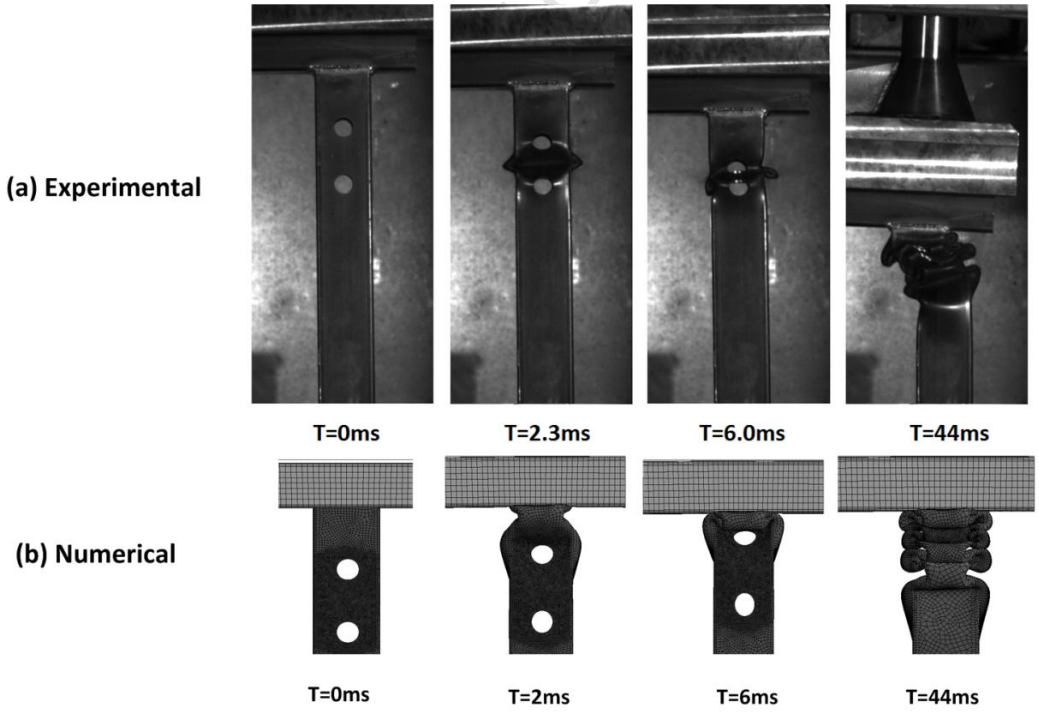

Figure 4.31: Transient response of impacted end of the BD3-396 bumper system from (a) experimental and (b) numerical results

4.4 Summary

The numerical model for the simplified bumper system is validated with a comprehensive set of experiments. The numerical model is validated with regards to deformation mode and crush distance of the longitudinal member and the flex point height of the crossbeam. Overall, the numerical model developed (comprising of the Simplified Johnson-Cook material model, boundary conditions and contact algorithms) accurately predicts the behaviour of the experimental bumper system with very good correlation. The crush distance, which represents the critical deformation of the bumper system, is predicted with a maximum error of 21%. The flex-point height of the crossbeam, where the kink is located, correlates very well between the experimental and numerical results.

In the comparison of the transient response between the experimental and numerical results, the validation model predicts the significant stages timely and the deformation satisfactorily for all bumper systems. The **BD3** bumper system results show slight variation in the matter of the deformation transient behaviour. This may be a need to further fine-tune the mesh around the discontinuities or further investigate the repeatability of the experiments within this group.

5. Parametric Study

This chapter reports on the use of numerical simulations to investigate the influence of parameters not investigated experimentally, such as the wall-thickness of the crossbeam and two geometric variations of the bumper system components. Two different geometric profiles of the crossbeam and longitudinal members are modelled. The main objective is to assess the deformation and the energy absorbing characteristics of the simplified bumper system with numerical modifications. The parametric study accounts for a total of 28 numerical simulations.

5.1 Parameter Selection

5.1.1 Influence of wall-thickness of crossbeam

The influence of the wall thickness of the crossbeam is investigated by varying the wall thickness from 1.0mm to 4.0mm in increments of 0.5mm. The wall-thickness is projected inwards to maintain an external dimension of 60x40mm. Figure 5.1 illustrates the extremes of the wall-thickness of the crossbeam investigated.

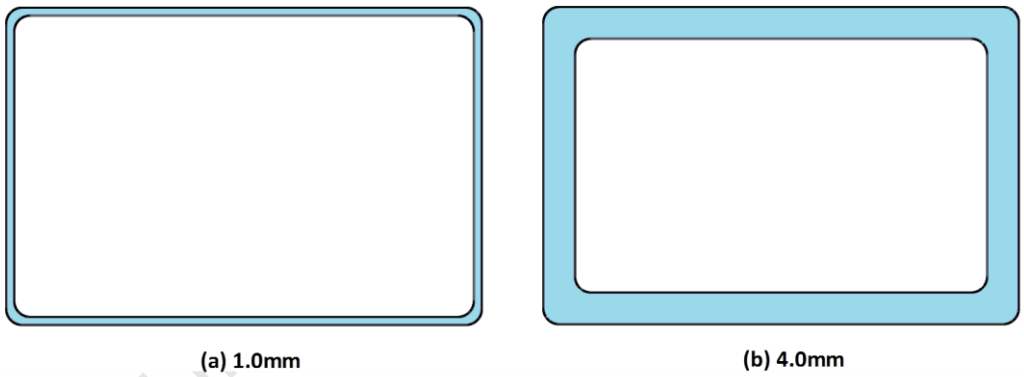

Figure 5.1: Illustration of wall-thickness of the crossbeam (a) minimum and (b) maximum extremes

5.1.2 Geometric profile of crossbeam

Two different geometric profiles of the crossbeam and longitudinal members are investigated. A straight and curved crossbeam profiles as illustrated in Figure 5.2 are studied. The dimensions of the cross-section of all crossbeams are 60x40mm, and the length is kept constant at 1125mm. The curved crossbeam profile has an increase in height of 100mm from the free edge to the midpoint; generating an incline of 17.9° at the crossbeam and longitudinal member interface. The volume change to the curved profile is negligible and allows for a direct comparison.

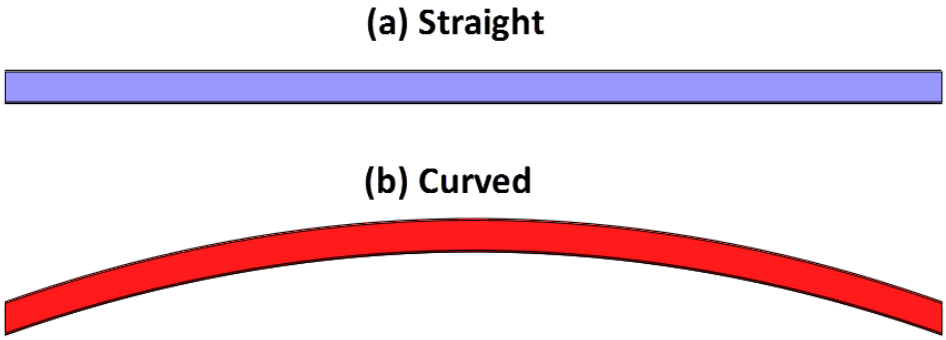

Figure 5.2: Schematic of (a) straight and (b) curved crossbeam profiles

5.1.3 Geometric profile of longitudinal member

The different profiles of the longitudinal members investigated are illustrated in Figure 5.3. The straight longitudinal member has a cross-section of 60x60mm and a total length of 650mm. The wall-thickness of the members is 2.0mm. For the tapered longitudinal member, the base dimensions are 100x60mm. The end of the tapered longitudinal is clamped up to a height of 50mm. Tapering of the left face is at an angle of 5.7° from the base. A tapered tube is reported to respond more favourably in a controlled manner in oblique and transverse loading conditions [53, 54, 63].

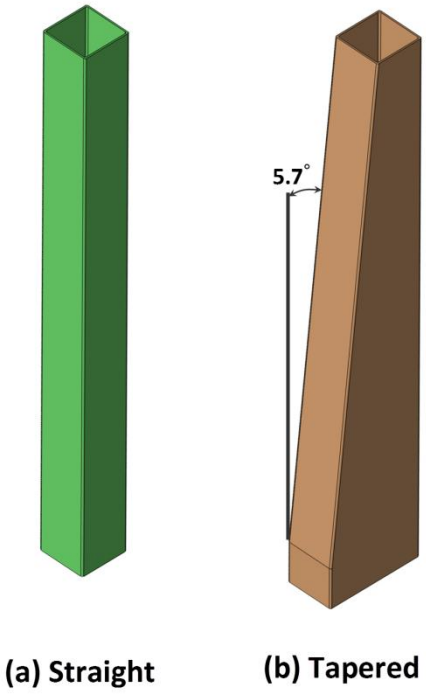

Figure 5.3: Schematic of (a) straight and (b) tapered longitudinal members

The mass property of the components is summarised in Table 5.1. The mass of the crossbeams vary from 1.73kg to 6.49kg, depending on the wall-thickness.

Profile	Mass (kg)
Straight crossbeam	1.73 – 6.49
Curved crossbeam	1.73 – 6.49
Straight longitudinal member	2.36
Tapered longitudinal member	3.03

Table 5.1: Mass properties of bumper system components

5.2 Simplified bumper system models

The finite element formulation discussed in section 4.1 is employed in the numerical parametric study. The velocity of the impactor is set at 8.85ms^{-1} and a drop mass of 500kg is selected resulting in a total of 19.6kJ of kinetic energy to be absorbed by the bumper system.

For the parametric study, a universal material is chosen for the different bumper system components to minimise the number of varied parameters. The material of the square tubes of 2.0mm wall-thickness is selected to replicate the deformation response of the impacted longitudinal member. The *Simplified Johnson-Cook* material model constants for the material are summarised in Table 4.5 (Square @ 2.0mm).

The following identification systems are used to distinguish the geometric varied bumper systems and are grouped accordingly:

SCB-SLM-x.x Straight crossbeam (SCB) and straight longitudinal members (SLM)

SCB-TLM-x.x Straight crossbeam (SCB) and tapered longitudinal members (TLM)

CCB-SLM-x.x Curved crossbeam (CCB) and straight longitudinal members (SLM)

CCB-TLM-x.x Curved crossbeam (CCB) and tapered longitudinal members (TLM)

where ***x.x*** represents the wall-thickness of the crossbeam in that specific model.

The identification system is depicted with the corresponding bumper system geometry in Figure 5.4.

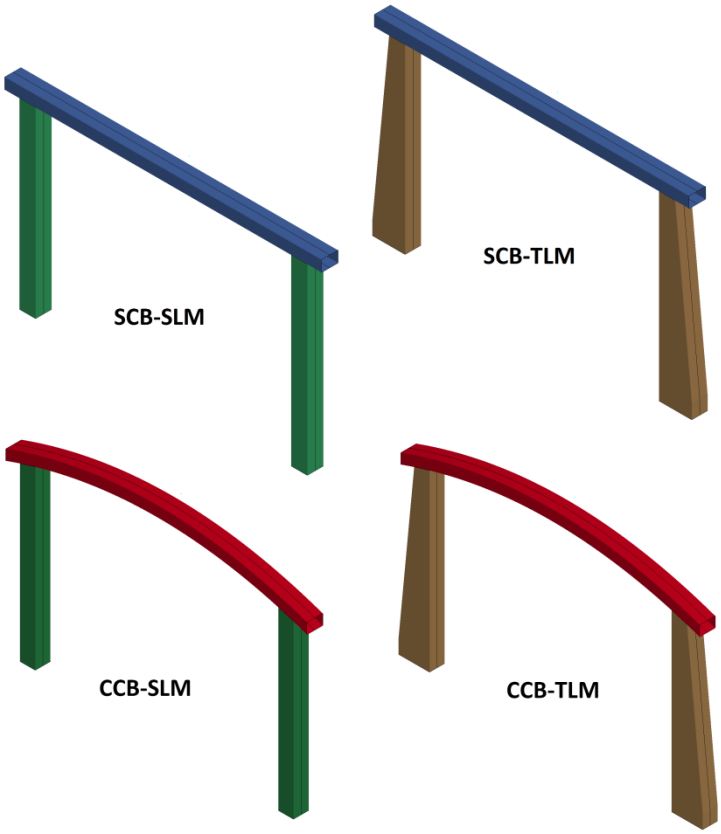

Figure 5.4: Bumper system identification

The four geometric variations of the components are meshed and modelled for the execution in LS-Dyna R4.2.1. solver with half-symmetry. The mesh properties are summarised in Table 5.2.

Profile	No. of Elements	Approx. Element Size (mm^2)
Straight crossbeam	6075	5.0 x 5.0
Curved crossbeam	6210	
SCB-SLM longitudinal	11 328	2.75 x 2.75
SCB-TLM longitudinal	13 746	
CCB-SLM longitudinal	11 328	
CCB-TLM longitudinal	13 983	

Table 5.2: Mesh properties of bumper system components of the parametric study

5.3 Crossbeam wall-thickness and profile

A common occurrence in the results, including crush distance, force calculations and energy absorption, is that there is a *transition value* where the trend of the wall-thickness of the crossbeam behaviour changes. The change could be a change in direction of the trend (increases or decreases) or an abrupt change in value. The *transition values* of the two crossbeam profiles differ in a few cases and are discussed in this section.

5.3.4 Deformation modes influenced by wall-thickness of the crossbeam and profile

5.3.4.1 Deformation modes of crossbeam

The crossbeam, whether straight or curved, generally deformed at three different locations labelled Region **A**, **B** and **C**, shown in Figure 5.5. In general, local plastic hinge formation is experienced in Region **A**, local bending occur at Region **B** and lateral flattening is observed at Region **C**.

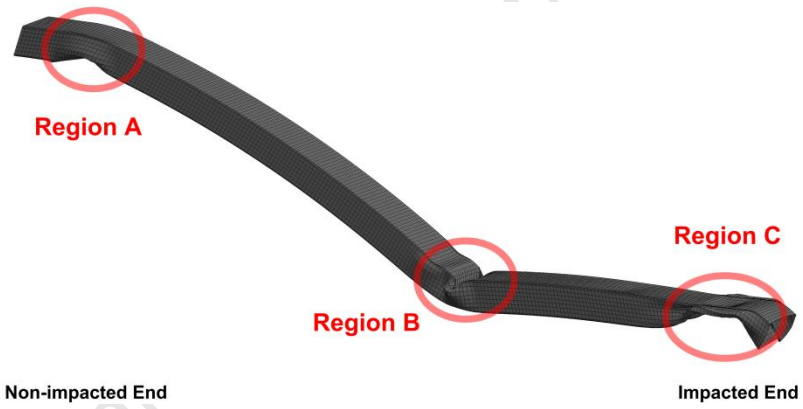

Figure 5.5: Deformation regions of crossbeam component (*CCB-SLM-1.0* shown)

The deformed side profiles from the **SCB-SLM** and **CCB-SLM** simulations are shown in Figures 5.6 and 5.7 respectively. with focus on the effects of the change in wall-thickness. The deformed side profiles from the **SCB-TLM** and **CCB-TLM** simulations can be found in *Appendix B*.

Region **A** represents the location in the crossbeam where the plastic hinge is formed and the side wall folds outwards at the non-impacted end of the longitudinal member interface. In some cases the crossbeam bends to the extent that it creates an inward pulling motion of the non-impacted longitudinal member. The side wall folding is more noticeable in the thinner-walled crossbeams. The curved crossbeams generally deform more in Region **A** than

the straight crossbeam and has more excessive side wall folding as the interface is at an angle, intensifying the stress concentration area further.

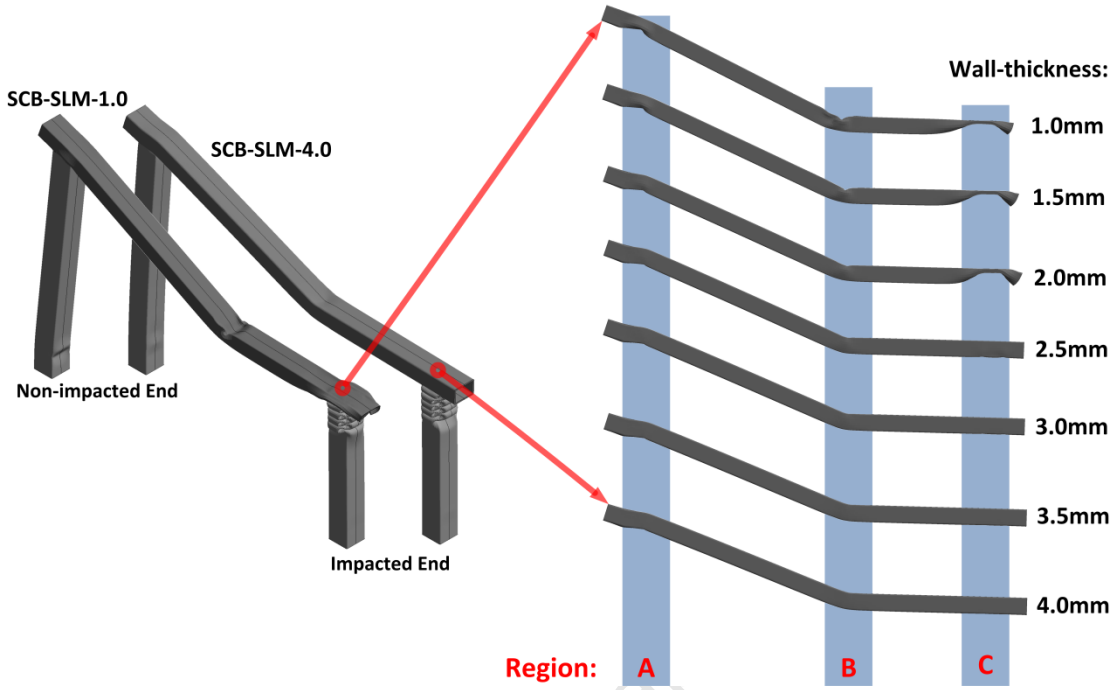

Figure 5.6: Deformed shapes of the crossbeam component from the *SCB-SLM* simulations

Region **B** illustrates the local bending failure in the middle section of the crossbeam where there are no support. The offset impact loading condition creates a high stress concentration near the edge of the impactor, resulting in the local bending failure of the crossbeam. Bending failure of this nature is common within thin-walled structures exposed to loading conditions perpendicular to the longitudinal direction. The bending is initiated with a plastic hinge at the top (impacted) surface of the crossbeam and develops further with the travel of the impactor. Thereafter, the upper flanges fold inward while the side-walls fold outward creating a *kink* in the crossbeam, categorised as a local bending failure. The curved crossbeams show more prominent bending failure than the straight crossbeams. This is a consequence of the gap difference between the impactor and the longitudinal members. The curved crossbeam and impactor are in contact for a greater distance before any contact between the impactor and longitudinal occurs. This results in the curved crossbeam to deform and bend more because of the additional interaction with the impactor. More energy is thereby absorbed by a curved crossbeam than a straight profiled one.

In region **C,** lateral flattening of the crossbeam is only observed at the impacted end of the bumper systems where the side-walls buckle outwards and the plastic hinges are formed along the top and bottom flanges. The development of plastic hinges removes the constraint the flanges on the side-walls, intensifying the outward buckling respectively.

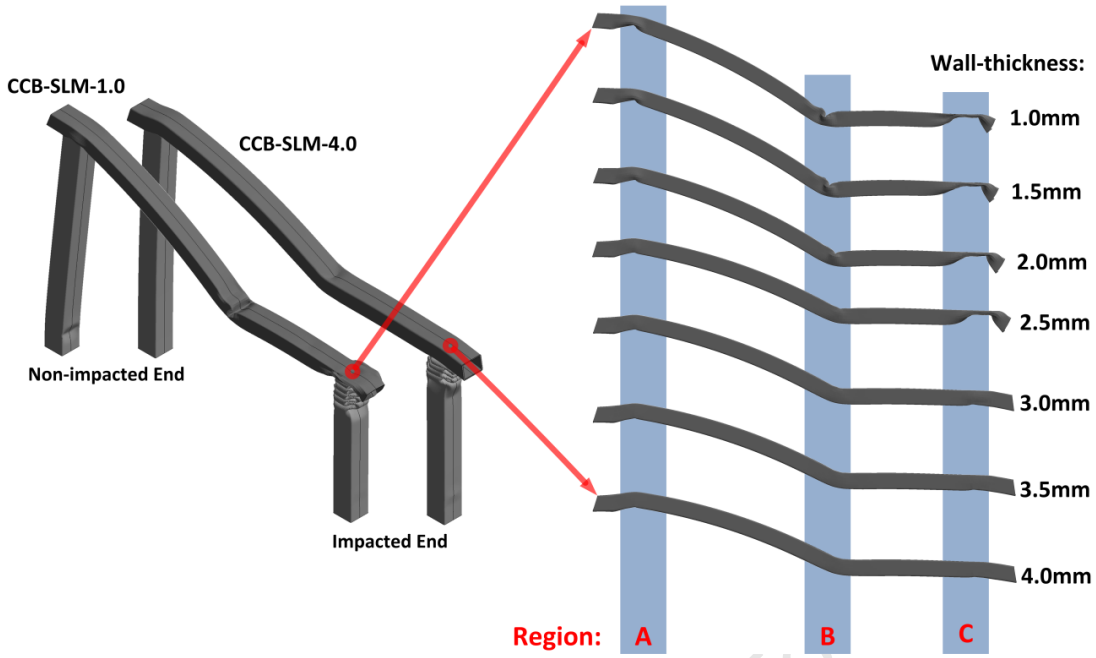

Figure 5.7: Deformed shapes of the crossbeam component from the *CCB-SLM* simulations

From the numerical simulations, the increase in the wall-thickness has a definite effect on the outcome of the deformation at region **C**. The deformation lateral flattening, is only evident at crossbeams with wall-thicknesses lower than 3.0mm. For the straight crossbeams, the lateral flattening occurs with thicknesses ranging from 1.0mm - 2.0mm as shown in Figure 5.6.; whereas for the curved crossbeams, it occurs in the range 1.0mm – 2.5mm, as shown in Figure 5.7. The results indicate a definite *transition value* of the occurrence of lateral flattening in the simplified bumper systems. The *transition value* depends upon the threshold of the crossbeam, undergoing lateral flattening, and the threshold of the impacted longitudinal member, undergoing progressive buckling. The increase in wall-thickness of the crossbeam increases the threshold of the component, eventually favouring progressive buckling of the impacted longitudinal member. The straight crossbeams exhibit a higher threshold for lateral flattening than the curved crossbeams. This is not due to the geometry, but the kinematic mechanism during the deformation. The bending of the curved crossbeam during the impact creates a plastic hinge at the impacted longitudinal member interface, allowing for an even thicker-walled crossbeam (2.5mm) to deform by lateral flattening. The top edge of the longitudinal members are inclined at 17.9°, thus presenting a high stress concentration region for the formation of the plastic hinge and thereby the failure of the crossbeam. The deformation modes of the longitudinal members are discussed in section 5.3.4.2.

5.3.4.2 Deformation modes of longitudinal member

The impacted longitudinal member is the main energy absorbing component in the simplified bumper system, and it has the most extensive deformation in all of the simulations carried out. The mode of deformation is independent of the profile geometry of the longitudinal member investigated. The impacted longitudinal member undergoes progressive buckling which is stable and favourable with a high energy absorbing capacity. An asymmetric mode of progressive buckling is observed throughout, where the two opposing walls move inward while the adjacent walls move outward, forming a lobe. The crush distance, number of lobes and the symmetry of the deformation are influenced by the variations to the parameters within this study.

- **Straight crossbeam profile**

The deformations observed in the **SCB-SLM** simulations are the most stable. The deformed shapes and crush distances of the impacted longitudinal members are shown in Figure 5.8. The symmetry of the lobe formation is observed to be exceptional, indicating the change of the wall-thickness of the crossbeam does not affect the response of the bumper system in this regard. A slight inward stacking profile of the lobes is observed within the thick-walled crossbeams systems and is because of the lateral forces generated by the pull-in motion. The number of lobes is consistent and correlates with the crush distance of the members accordingly. The increase in the wall-thickness of the crossbeam decreases the crush distance of the impacted longitudinal member, indicating that more energy is absorbed by the other components. However, a *transition value* is observed between the wall-thicknesses of the crossbeam of 2.0mm and the 2.5mm where the crush distance increases substantially and thereafter decreases proportionately with the increase in wall-thickness.

The deformed shapes of the tapered impact longitudinal members of the **SCB-TLM** simulations are shown in Figure 5.9. As mentioned, the increase in wall-thickness of the crossbeam decreases the crushing distance of the impacted longitudinal member. The transition value correlates between the bumper systems with a straight crossbeam profile. The change of the longitudinal profile decreases the crushing distance. This is due to the expected additional plastic deformation that tapered profiles experience during progressive buckling, owing to greater volume (compared with straight profiles).

Figure 5.8: Deformation of impacted longitudinal members of the SCB-SLM simulations

Figure 5.9: Deformation of impacted longitudinal members of the *SCB-TLM* simulations

- **Curved crossbeam profile**

The **CCB-SLM** simulations differ from the **SCB-SLM** only by the geometric shape of the crossbeam. The final deformed shapes of the impacted longitudinal members are shown in Figure 5.10. The curved crossbeam bumper systems show similar trend with straight crossbeam bumper systems in terms of the crush distance. The crush distance decreases with the increase in the wall-thickness of the crossbeam and a *transition value* is observed. The *transition value* is observed at a thicker-walled interval for the **CCB-SLM** simulations, between 2.5mm and 3.0mm. The crush distance of the impacted longitudinal member is predominantly lower in a bumper system with a curved crossbeam.

Figure 5.10: Deformation of impacted longitudinal members of the CCB-SLM simulations

The profile of the crossbeam influences the stacking of the lobes of the longitudinal member. The stacking shape of the lobes is not entirely vertical after a certain curved wall-thickness of the crossbeam of 2.5mm is reached. The mid-point bending of the curved crossbeam induces a bending moment at impacted end. Initially, the interface plane is at an angle to the vertical axis of the longitudinal member shown in Figure 5.11. In the case of a thin-walled crossbeam bumper system, the interface plane is deformed to a near horizontal

plateau, after the initiation of the buckling of the impacted longitudinal member. Conversely, a thick-walled crossbeam bumper system behaves differently. Due to the rigidity of the crossbeam and lack of lateral flattening, the interface plane remains at a relative angle to the vertical axis of the longitudinal member. This increases the bending moment induced at this interface. As the impacted longitudinal member deforms, the axial forces experienced by the member are not aligned with the vertical axis (i.e. bending moment influence), resulting in the asymmetric formation of the lobes. Oblique/offset impact loading is therefore prevalent at the interface between a thick-walled curved crossbeam and impacted longitudinal member.

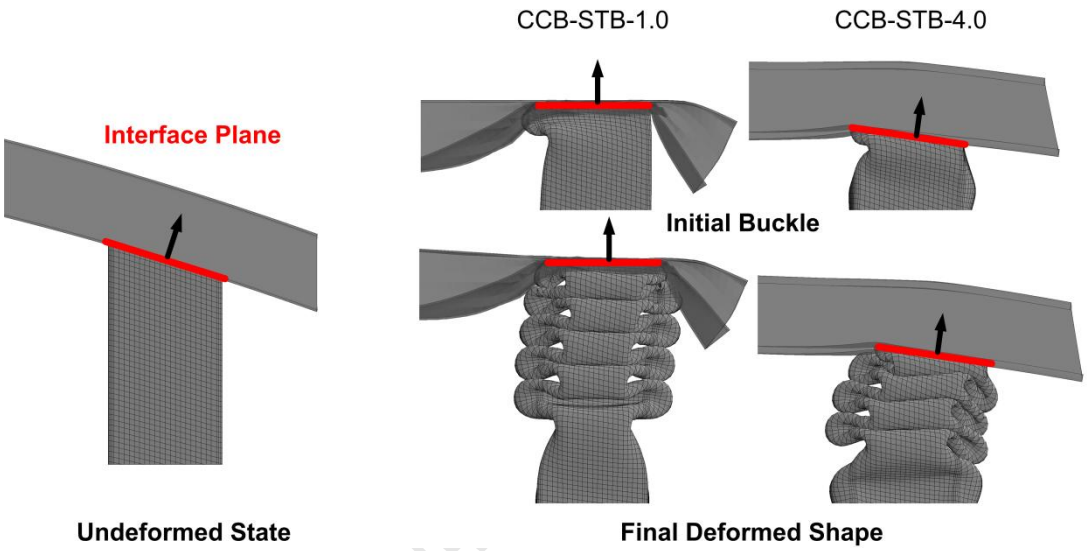

Figure 5.11: Orientation of interface plane at impacted end with change of wall-thickness of the crossbeam

(*Front View*)

The final deformed shapes of the impacted longitudinal members from the **CCB-TLM** simulations are presented in Figure 5.12. The resulting behaviour influenced by the wall-thickness of the crossbeam and profile is similar to that observed in **CCB-STB**.

Figure 5.12: Deformation of impacted longitudinal members of the *CCB-TLM* simulations

5.3.5 Crush Distance

The extent of deformation of the bumper systems is an important factor to consider when comparing energy absorbing structures. The crush distance, in most cases, is proportional to the energy absorbed; provided consistent modes of failure are observed. The simulations of the bumper system conducted include components with varied geometries and thereby crush distances of key points are taken throughout. Four crush distances are calculated per bumper system and is illustrated in Figure 5.13. The crush distances are plotted versus the wall-thickness of the crossbeam. Results are tabulated in *Appendix C*. The four crush distances are:

A. Mid-point of crossbeam
B. Flex point
C. Impacted end
D. Mid-point of impacted longitudinal member

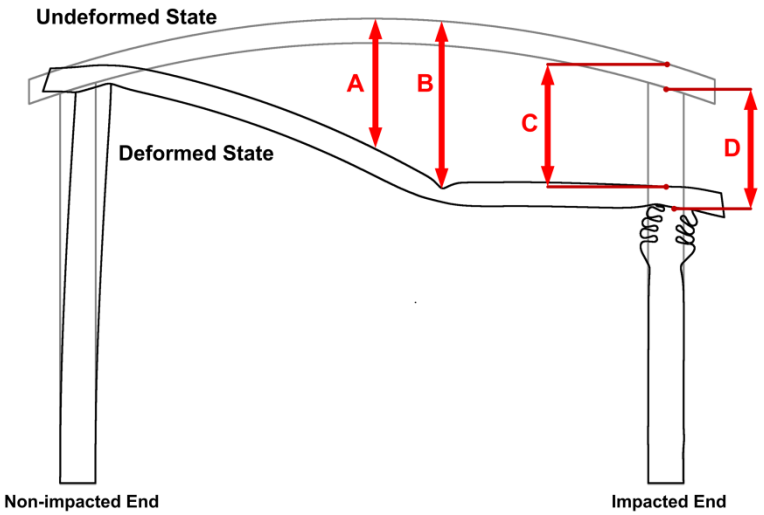

Figure 5.13: Numerical calculations of the crush distances of the bumper system

- **Mid-point of crossbeam**

The initial and final height of the mid-point of the crossbeam is measured and plotted in Figure 5.14. Generally for an increase in the wall-thickness of the crossbeam a decrease in the mid-point deflection of the crossbeam is observed. The deflection is higher in the bumper systems with a curved crossbeam. This is expected as the crossbeam is required to deform further until the impactor strikes the longitudinal. The *transition value* is clearly visible in the curved crossbeam bumper system results and is about 2.5mm.

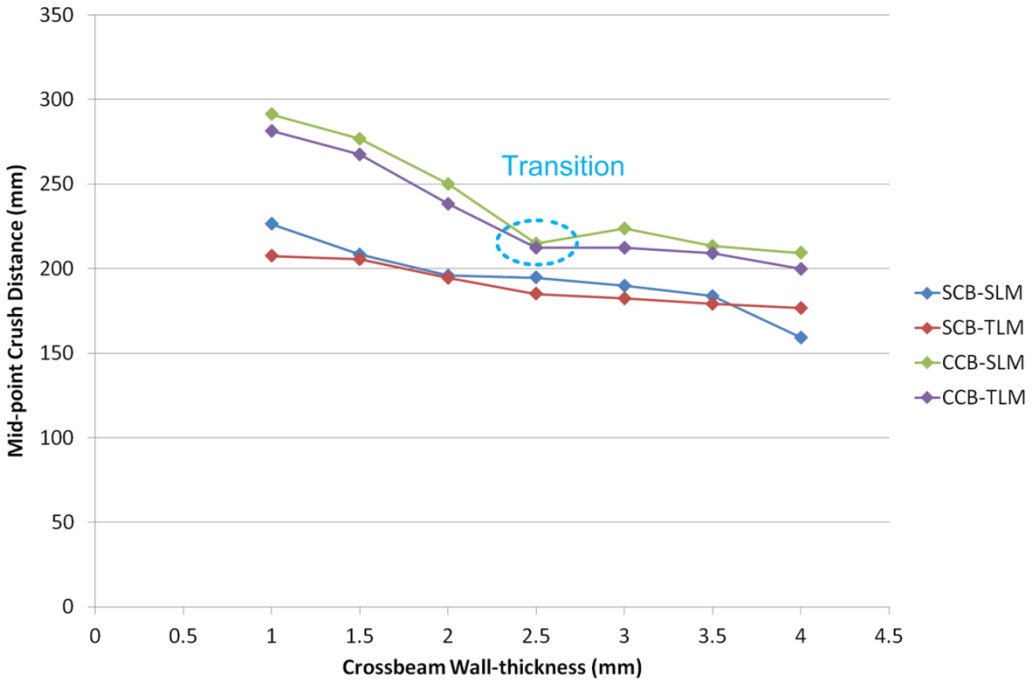

Figure 5.14: Crossbeam mid-point crush distance vs wall-thickness of all bumper systems

- **Flex point**

The flex point displacement calculated shows identical trends, as observed with the crush distance of the mid-point of the crossbeam. The plotted results can be found in *Appendix C*.

- **Impacted end**

The crush distance calculated at the impacted end is of most importance; as this is a reflection of the performance of the energy absorbing structure. The results are plotted in Figure 5.15. There is a general trend of decrease in the crush distance with increase of in wall-thickness of the crossbeam.

The differences between the straight and curved crossbeam results are greater after the *transition value*, i.e. after 2.5mm. As mentioned, the curved crossbeam is required to deform to a greater extent than a straight crossbeam. This increase in deformation increases the energy absorbed by the crossbeam and further accounts for the greater difference between the results. The reason for the difference being greater after the *transition value* is that far more energy is absorbed by other components, rather than the impacted longitudinal member.

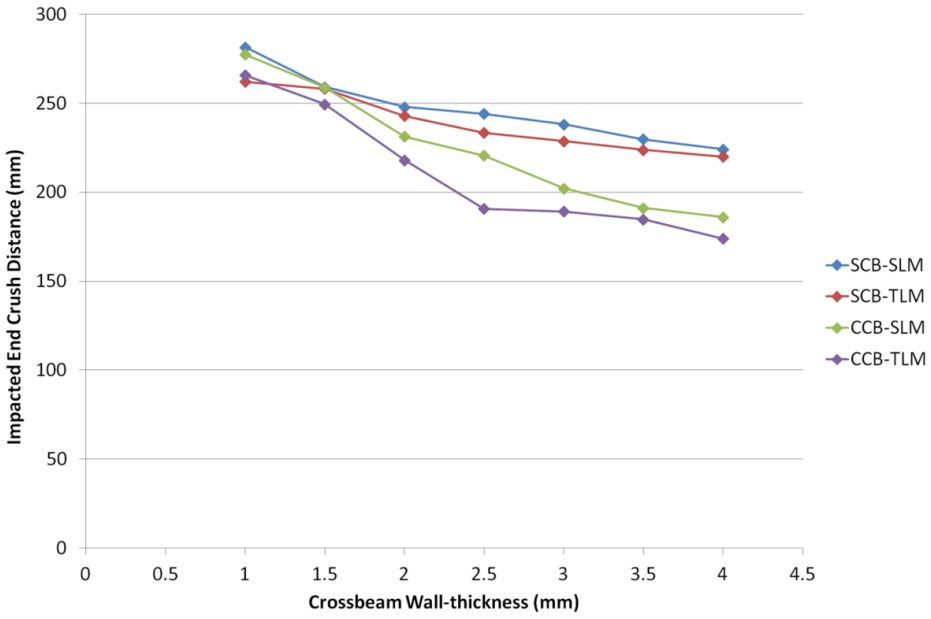

Figure 5.15: Impacted end crush distance vs wall-thickness of all bumper systems

- **Mid-point of impacted longitudinal member**

The results are calculated (label **D** in Figure 5.13) at the mid-point of the interface between the crossbeam and impacted longitudinal member, and are plotted in Figure 5.16. The *transition value* is observed more clearly in this representation of crush distance. For the straight crossbeam results, the *transition value* is from 2.0mm to 2.5mm, and for the curved crossbeam, it is from 2.5mm to 3.0mm. The longitudinal crush distance is observed to decrease before and after the transition value, showing a general trend that the crush distance decreases with increases in wall-thickness of the crossbeam. An abrupt increase after the transition is observed in the bumper systems with straight longitudinal members.

The **CCB-SLM** and **CCB-TLM** of wall-thickness 2.5mm have the least crush distance and can be interpreted as the bumper systems with the best distribution of impact energy and the highest potential for further energy absorption.

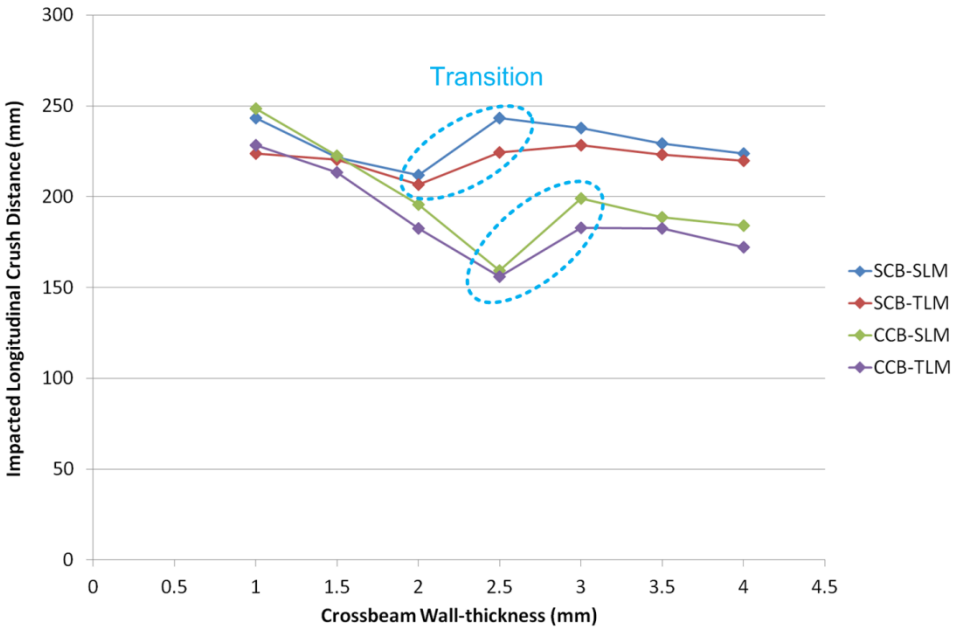

Figure 5.16: Impacted longitudinal member crush distance vs wall-thickness of all bumper systems

5.3.6 Energy Absorption

One of the main functions of the bumper system is the absorption of energy during an impact. The objective of the parametric study is to investigate the distribution of the energy between the components of the bumper system. The kinetic energy absorbed from the impactor is 19.6kJ for a mass of 500kg travelling at velocity of 8.85ms^{-1}. In comparison to the total impact energy, negligible energy is lost in the form of friction. In an offset impact scenario, the crossbeam and the impacted longitudinal member absorb the majority of the impact energy. In the parametric study, the crossbeam internal energy absorbed ranges

from 1.28kJ to 7.32kJ. The impacted longitudinal member energy absorbed ranges from 11.64kJ to 17.71kJ and for the non-impacted longitudinal member the range is 0.20kJ to 0.79kJ. The internal energy results of the parametric study are tabulated as follows:

ID	Crossbeam (kJ)	Impacted longitudinal member (kJ)	Non-Impacted longitudinal member (kJ)	Total Internal Energy Absorbed (kJ)
SCB-SLM-1.0	1.28	17.71	0.44	19.4
SCB-SLM-1.5	2.53	16.49	0.37	19.4
SCB-SLM-2.0	4.05	14.93	0.34	19.3
SCB-SLM-2.5	2.27	16.88	0.35	19.5
SCB-SLM-3.0	2.42	16.64	0.38	19.4
SCB-SLM-3.5	2.64	16.36	0.43	19.4
SCB-SLM-4.0	2.85	16.10	0.47	19.4

Table 5.3: Internal energy absorbed by components of the RCB-SLM bumper systems

ID	Crossbeam (kJ)	Impacted longitudinal member (kJ)	Non-Impacted longitudinal member (kJ)	Total Internal Energy Absorbed (kJ)
SCB-TLM-1.0	1.33	17.41	0.68	19.4
SCB-TLM-1.5	2.63	16.07	0.67	19.4
SCB-TLM-2.0	4.22	14.47	0.60	19.3
SCB-TLM-2.5	2.99	15.82	0.59	19.4
SCB-TLM-3.0	2.31	16.45	0.62	19.4
SCB-TLM-3.5	2.54	16.13	0.68	19.4
SCB-TLM-4.0	2.72	15.83	0.79	19.3

Table 5.4: Internal energy absorbed by components of the RCB-TLM bumper systems

ID	Crossbeam (kJ)	Impacted longitudinal member (kJ)	Non-Impacted longitudinal member (kJ)	Total Internal Energy Absorbed (kJ)
CCB-SLM-1.0	1.89	17.14	0.44	19.5
CCB-SLM-1.5	3.33	15.70	0.41	19.4
CCB-SLM-2.0	5.26	13.83	0.31	19.4
CCB-SLM-2.5	7.32	11.94	0.20	19.4
CCB-SLM-3.0	4.92	14.29	0.26	19.5
CCB-SLM-3.5	5.35	13.82	0.27	19.4
CCB-SLM-4.0	5.62	13.51	0.31	19.4

Table 5.5: Internal energy absorbed by components of the CCB-SLM bumper systems

ID	Crossbeam (kJ)	Impacted longitudinal member (kJ)	Non-Impacted longitudinal member (kJ)	Total Internal Energy Absorbed (kJ)
CCB-TLM-1.0	1.96	16.77	0.70	19.4
CCB-TLM-1.5	3.60	15.10	0.66	19.4
CCB-TLM-2.0	5.38	13.36	0.53	19.3
CCB-TLM-2.5	7.28	11.64	0.39	19.3
CCB-TLM-3.0	5.23	13.74	0.45	19.4
CCB-TLM-3.5	5.28	13.61	0.50	19.4
CCB-TLM-4.0	5.75	13.21	0.46	19.4

Table 5.6: Internal energy absorbed by components of the CCB-TLM bumper systems

5.3.6.1 Energy absorption by crossbeam

The variation of the wall-thickness alters the amount of internal energy absorbed by the crossbeam. In both crossbeam profiles, straight (**SCB**) and curved (**CCB**), the internal energy absorbed increases with the increase in wall-thickness up to the *transition value*. The *transition value* is 2.0mm for the straight crossbeam profile and for the curved crossbeam profile it is 2.5mm in the energy absorbed by the crossbeam results. After the *transition value*, there is an initial drop in the energy absorbed. Thereafter energy absorbed increases with an increase in wall-thickness; shown in Figure 5.17.

In all of the corresponding wall-thicknesses of the different profiled bumper systems, the curved profile bumper systems shows more internal energy being absorbed by the crossbeam; particularly after the *transition value* of 2.5mm where the curved profile results are approximately double that of the straight profiled results. The internal energy absorbed by the longitudinal members is discussed in section 5.4.7.

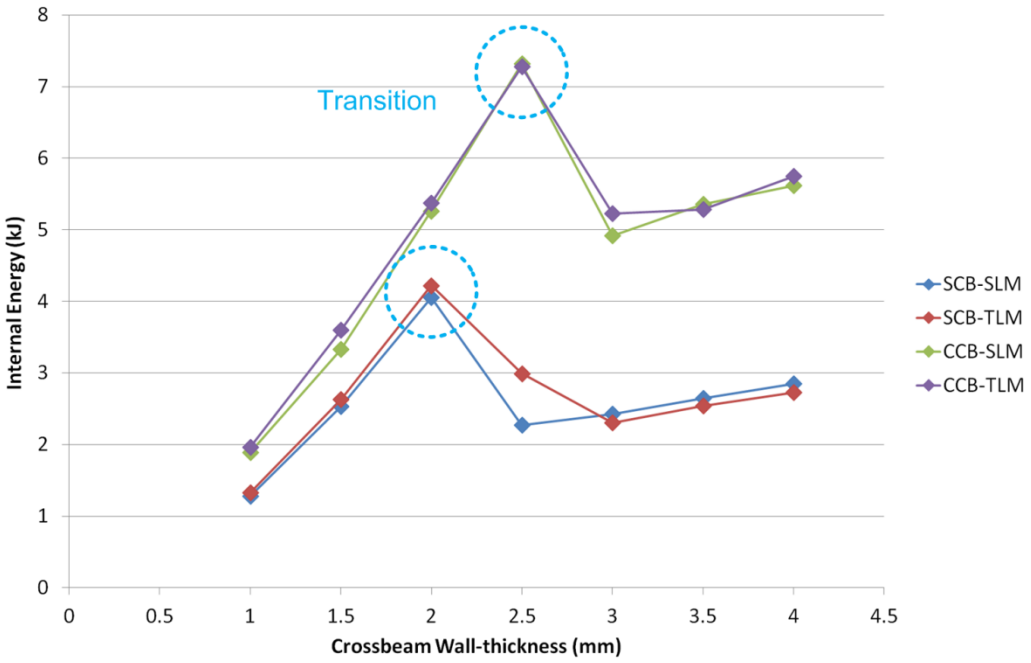

Figure 5.17: Internal energy absorbed vs wall-thickness of the crossbeam

5.3.6.2 Energy absorption by impacted longitudinal member

The effect of the geometric variation of the crossbeam shows that the straight crossbeam dissipates less energy away from the impacted longitudinal member than the curved crossbeam systems, especially after the *transition values* where the crossbeam has a higher wall-thickness. The internal energy absorbed by the impacted longitudinal members is shown in Figure 5.18. The internal energy absorbed decreases with the increase in wall-thickness of the crossbeam, as does crush distance. As the wall-thickness increases, the bumper system is able to dissipate more of the impact energy through the crossbeam and the non-impacted longitudinal member as the crossbeam gains more load bearing capacity through the increase in overall stiffness. The *transition value* is evident in the energy absorbed by the impacted longitudinal member in all bumper systems. For the straight crossbeam (**SCB**) bumper systems, this occurs from 2.0mm to 2.5mm and for the curved crossbeam (**CCB**) bumper systems from 2.5mm to 3.0mm wall-thickness values.

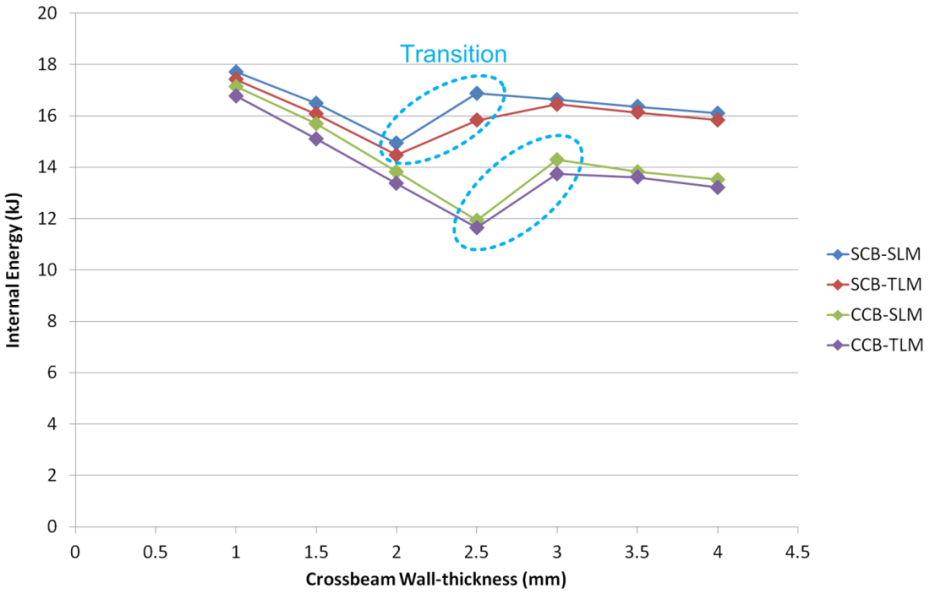

Figure 5.18: Internal energy absorbed vs wall-thickness of the impacted longitudinal member

5.3.6.3 Energy absorption by non-impacted longitudinal member

In general, shown in Figure 5.19, there is a decrease in energy being absorbed by the non-impacted member up to the *transition value*, thereafter there is an increase with the increase in wall-thickness of the crossbeam. The straight crossbeam (**SCB**) system energy absorption at the non-impacted end represents a parabolic trend with the wall-thickness of the crossbeam, at a minimum *transition value* of 2.5mm. The curved crossbeam (CCB) systems do not have a clear *transition values* for the energy absorption of the non-impacted longitudinal member are more irregular.

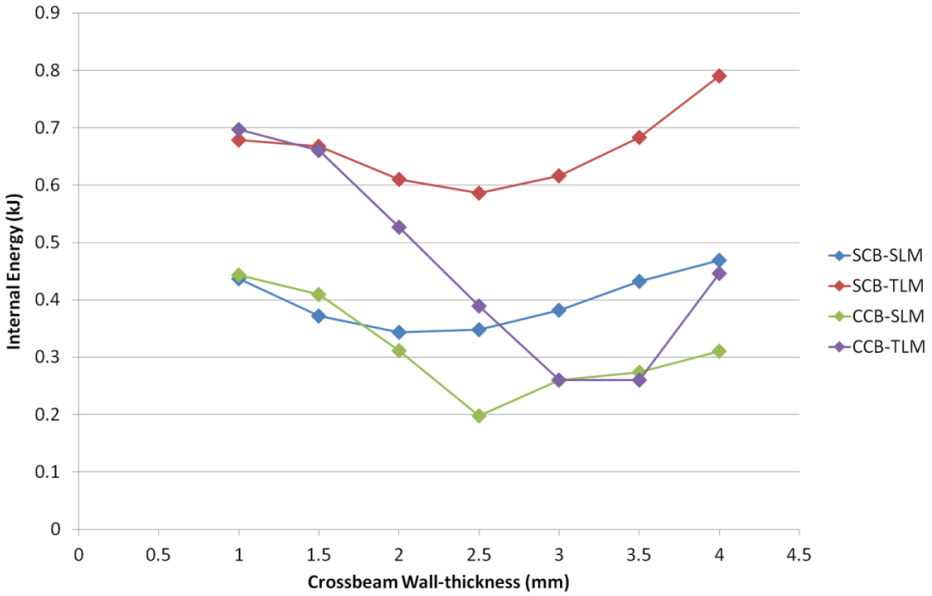

Figure 5.19: Internal energy absorbed vs wall-thickness of the non-impacted longitudinal member

The curved crossbeam (**CCB**) systems show a decrease of energy absorbed at the non-impacted end, with the increase in wall-thickness. The decrease in energy absorption is due to the plastic hinge formation at the non-impacted longitudinal member and crossbeam interface. This limits the load bearing capacity of the crossbeam at this interface, and therewith decreases the impact energy being transferred.

5.3.7 Axial Forces

The axial forces experienced at the clamped ends are recorded and discussed in this section. The clamps are positioned at the free ends of both longitudinal members, applying a constraint to secure all degrees of freedom. The forces experienced are representative of the forces that the rest of the structure may be subjected to, namely the passenger cell in the case of a vehicle.

5.3.7.1 Axial force at impacted end

The highest axial forces are experienced at the constrained end of the impacted longitudinal members. The axial forces at this end are plotted against the displacement of the impactor respectively. All **RCB-SLM** force calculated at the impacted end are plotted and shown in Figure 5.20.

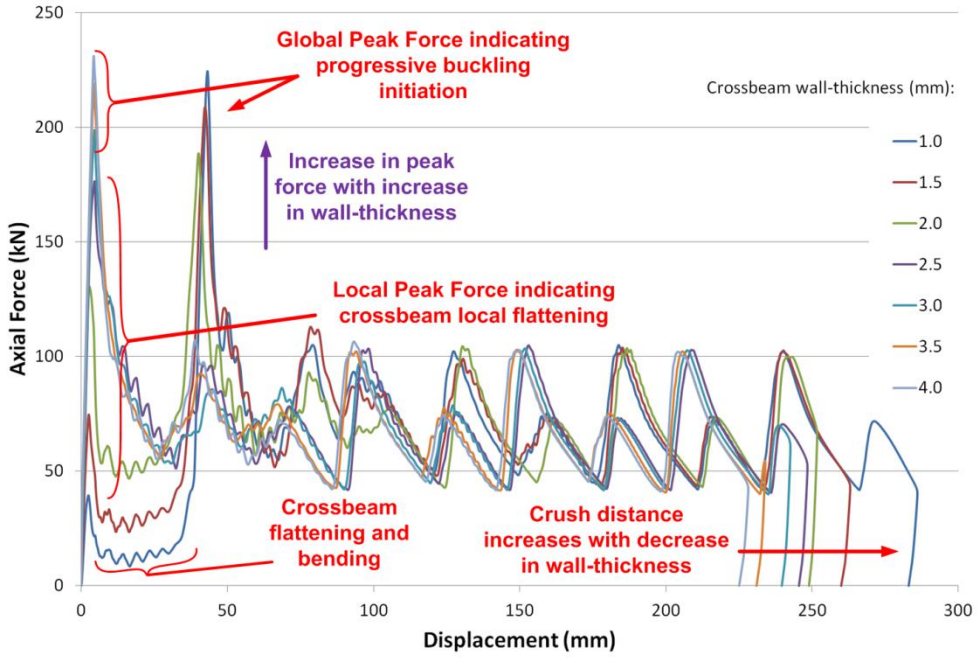

Figure 5.20: Axial force-displacement graph of *RCB-SLM* simulations at impacted end

Two peak axial forces are experienced in bumper systems with crossbeam wall-thicknesses below the *transition value*, in the **RCB-SLM** it is 2.5mm. The first peak force is associated with the crossbeam lateral flattening and the second peak force with the initiation of

progressive buckling. Bumper systems with higher wall-thickness of the crossbeam than the transition value only have a single global peak force indicating the initiation of progressive buckling. The axial-force displacement plots of the **RCB-TLM**, **CCB-SLM** and **CCB-TLM** are found in *Appendix D*. After the global peak force, which in all tests indicate progressive buckling, a repetitive cyclic axial-force displacement profile is observed representing the formation of several lobes.

The *transition value* in the **RCB-SLM** group is between 2.0mm and 2.5mm for wall-thickness of the crossbeam and the axial force-displacement of these two results are plotted in Figure 5.21.

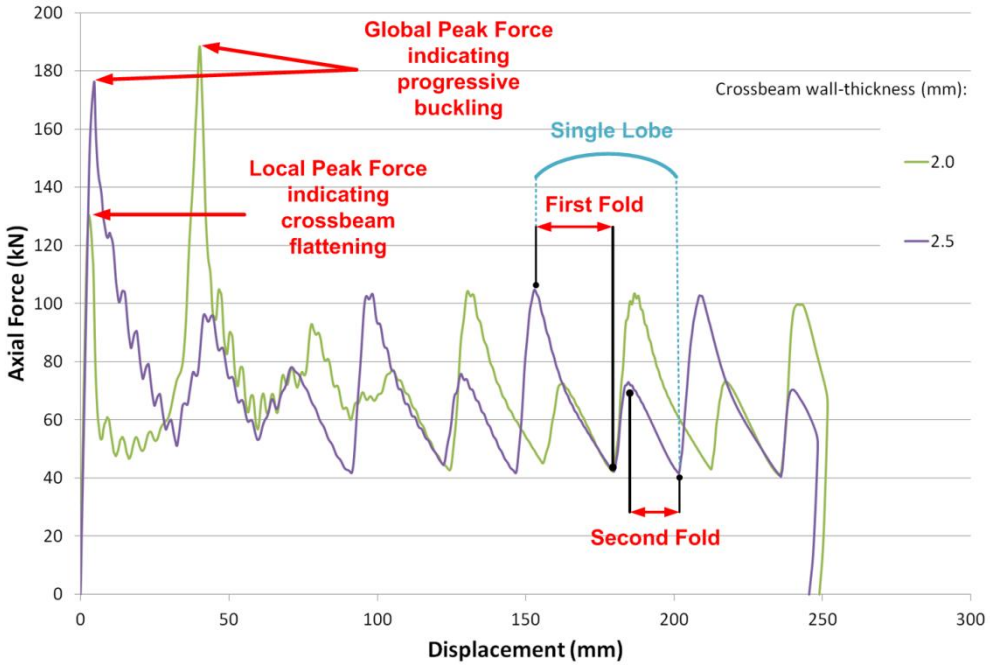

Figure 5.21: Axial force-displacement graph of the *transition value* of RCB-SLM simulations at impacted end

The axial-force displacement plot of the crossbeam of wall-thickness 2.0mm show a distinct initial peak force that is associated with the collapse of the crossbeam. The initial local peak force increases with the increase in the wall-thickness of the crossbeam and indicates the crossbeam lateral flattening failure. Thereafter, a global peak force is observed. A global peak force with a sharp contour is common in all **RCB-SLM** results and is associated with the formation of the first lobe in progressive buckling deformation mode. In the longitudinal member a typical progressive buckling force profile follows with a repetitive cyclic manner, whereby there are local minimum, ≈42kN, and local maximum, ≈103kN, force peaks are associated with the formation of lobes are observed. The bumper systems with a wall-thickness greater than 2.5mm do not exhibit an initial local peak force associated with crossbeam flattening failure.

The axial force-displacement calculations from the curved crossbeam (**CCB**) simulations differ in profile to the straight crossbeam (**SCB**) simulations. Significant **CCB-SLM** results are plotted in Figure 5.22 and are of a similar nature to the **CCB-TLM**. In both these curved crossbeam groups there is an initial low force profile observed, preceding sharp increase in the axial force. The initial low force profile, associated with the bending and lateral flattening of the crossbeam, occurs before 60mm of displacement. The magnitude of the force profile is observed to increase with wall-thickness of the crossbeam. A sharp increase in force, labelled **A** in Figure 5.22, is the contact point of the impactor and the crossbeam at the impacted end; where the arrow in the figure shows the progression of the point of contact with the increase in wall-thickness. The reason for the shift of the contact point in the thicker walled crossbeams is due to the lack of early deformation. The crossbeams of low wall-thickness exhibit side-wall folding and the collapse of the lower flanges, before the impactor contacts the crossbeam above the impacted longitudinal member. The deformations are shown in Figure 5.23 and occur at a comparatively similar time-step. A global peak force is observed for the initiation of progressive buckling throughout the **CCB** systems.

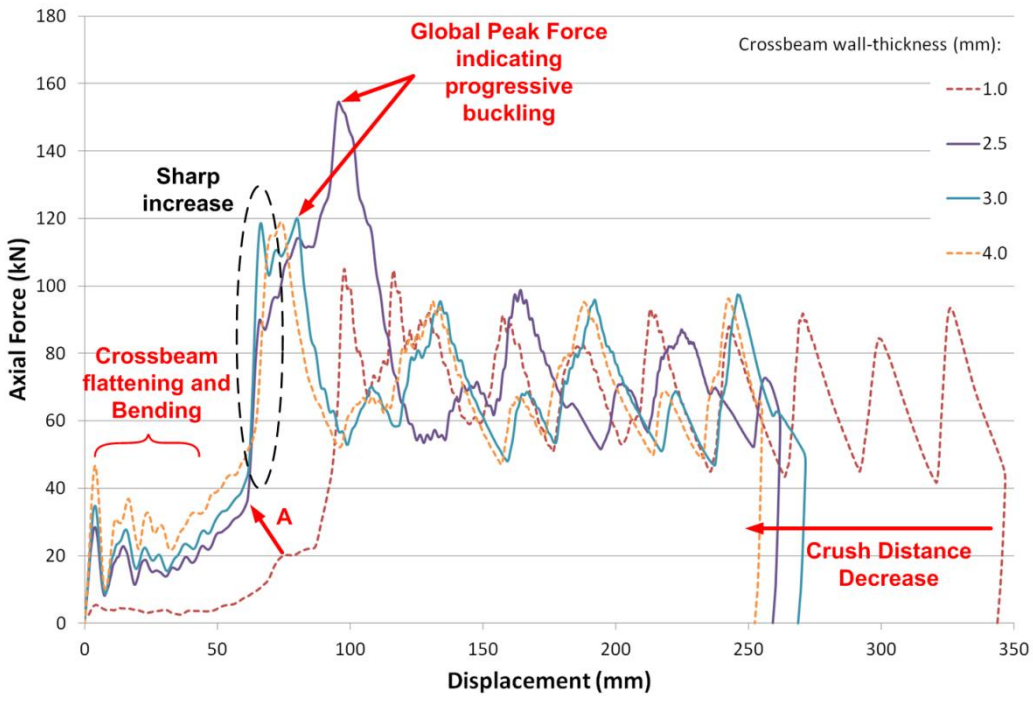

Figure 5.22: Axial force-displacement graph of the *transition value* of *CCB-SLM* simulations at impacted end

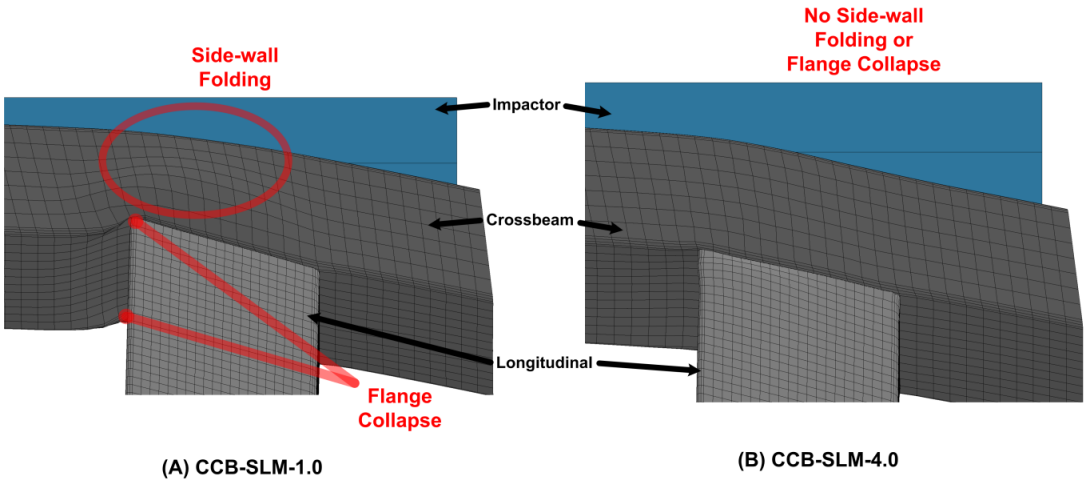

Figure 5.23: Comparison of early side-wall folding and flange collapse of the crossbeam in bumper systems (A) *CCB-SLM-1.0* and (B) *CCB-SLM-4.0*

In the curved crossbeam (**CCB**) bumper systems, the axial force-displacement profiles of the bumper systems before the *transition value* reveal certain key stages in the early deformation of the bumper systems. The significant stages are labelled **A**,**B** and **C** in Figure 5.24 and the deformation is depicted in Figure 5.25. The significant stage **A** is the contact of the impactor with the crossbeam above the longitudinal. With the increase in wall-thickness, this stage is observed at a lesser displacement, and is due to the decrease in early deformation of the crossbeam by lateral flattening. The full collapse of the crossbeam, by lateral flattening, is observed at stage **B** and thereafter the force increases until progressive buckling commences at stage **C**. In all stages, the force increases with the increase in wall-thickness of the crossbeam.

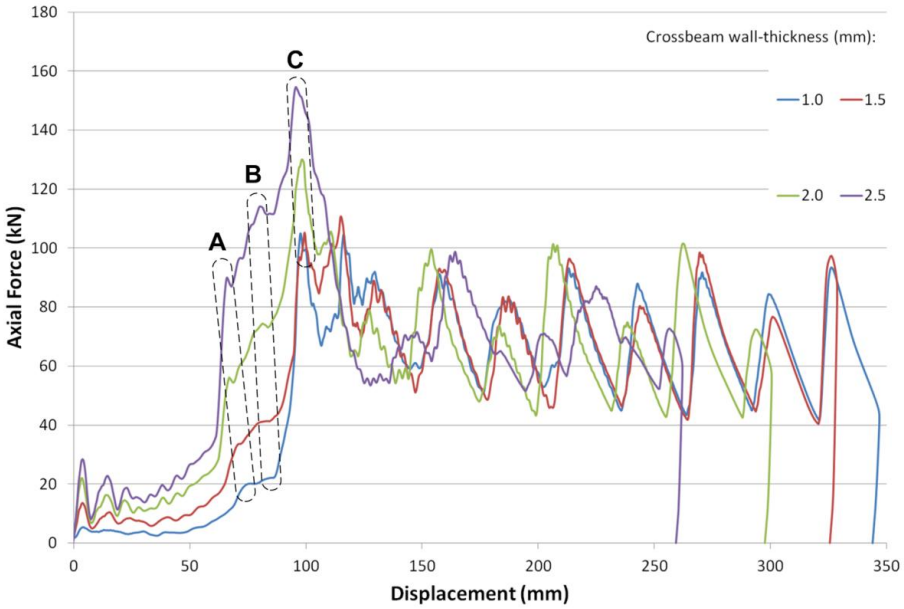

Figure 5.24: Axial force-displacement graph of *CCB-SLM* simulations at impacted end before *transition value*

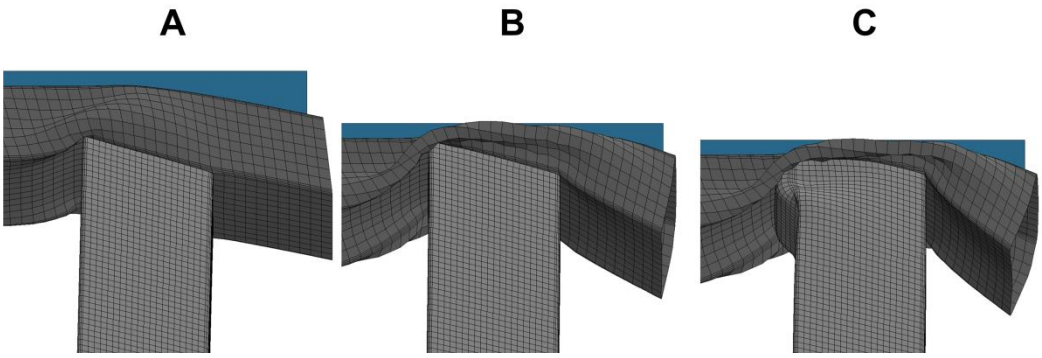

Figure 5.25: Significant stages in early deformation of *CCB-SLM-1.0* bumper system

The results for the curved crossbeam (**CCB**) bumper systems after the transition value are plotted in Figure 5.26 for the **CCB-SLM** simulations (**CCB-TLM** are of similar nature). Significant stages here are labelled **A** and **C**. There is no stage **B** associated with the lateral flattening failure of the crossbeam. The stage labelled **A**, contact of impactor with crossbeam, coincides with the results of thick-walled crossbeams. This is expected as there is no definite early deformation of the crossbeam at the interface with the impacted longitudinal member. Stage **C** indicates the initiation of progressive buckling of the impacted longitudinal member. The high peaks occur at stage **C** with the formation of lobes, and since the longitudinal has an inclined interface at the top edge, several local peaks result.

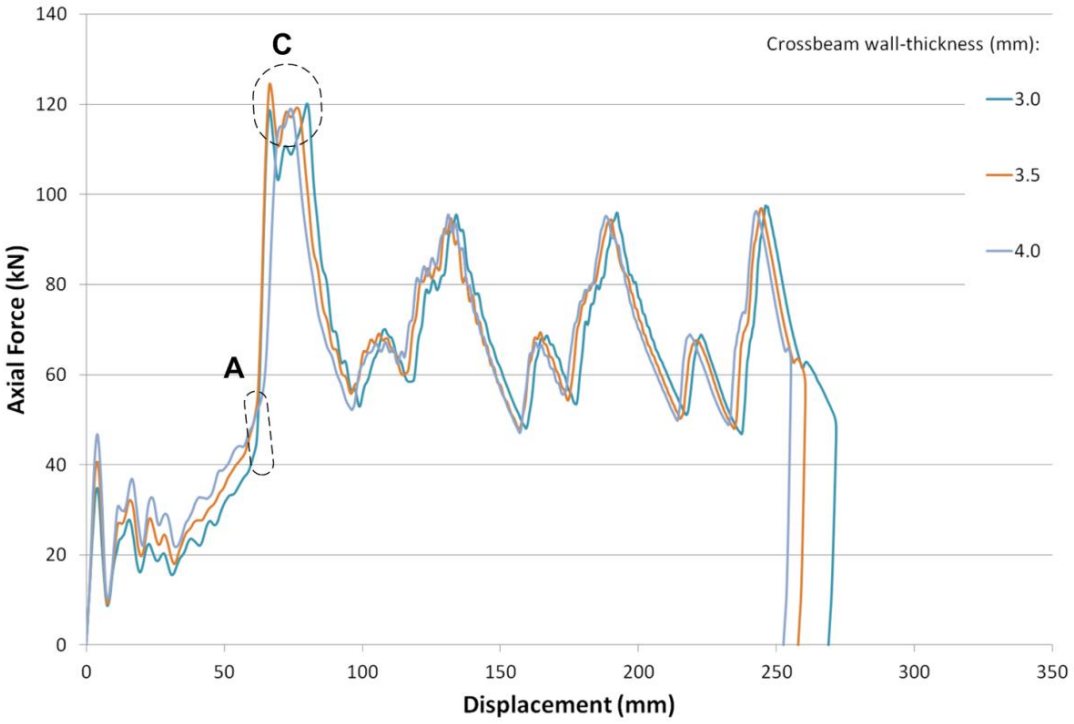

Figure 5.26: Axial force-displacement graph of *CCB-SLM* simulations at impacted end after *transition value*

5.3.7.2 Axial force at non-impacted end

Compared to the deformations observed at the non-impacted end, the axial forces experienced at the clamps are not significant. The axial force-displacement profiles of the **RCB-SLM** are plotted in Figure 5.27 with two significant observations made. The transient force increases with the increases in wall-thickness, indicating that a crossbeam of greater wall-thickness induces better load distribution. The other observation is the initial negative force; this occurs when the longitudinal is 'pulled' from the clamp. This force is generated by the inward pulling motion as the bending failure is initiated in the crossbeam. The formation of the bend in the crossbeam causes a slight spring-back effect that produces a lifting force at the non-impacted end due to a bending moment. After the lifting force effect, the downward travel of the impactor produces a downward axial force.

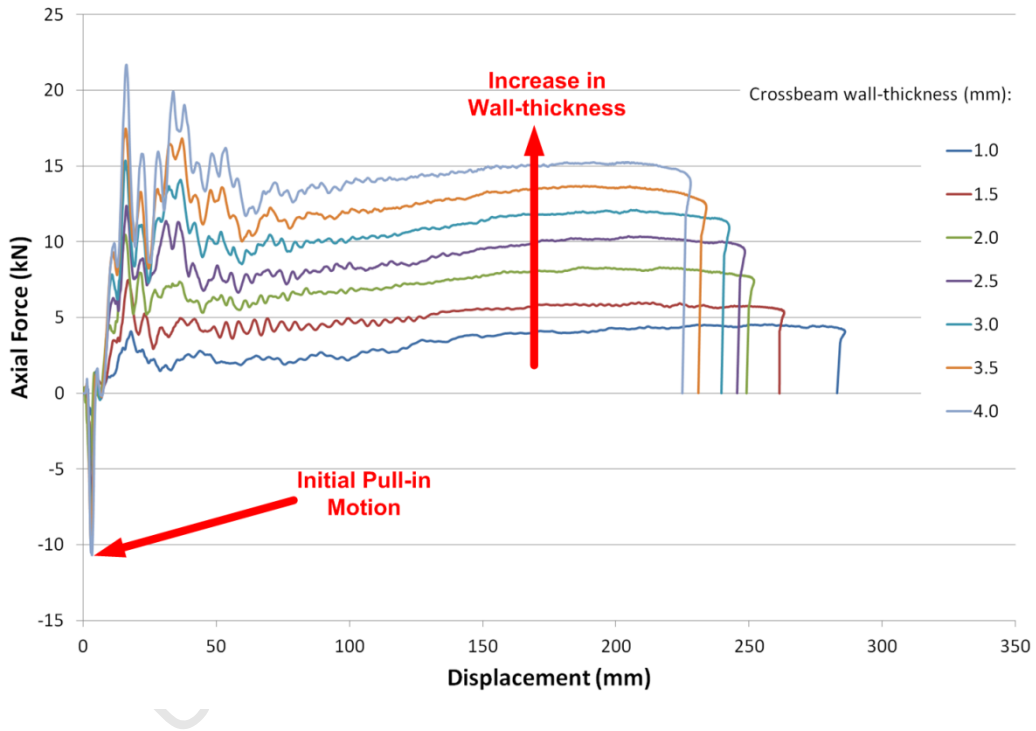

Figure 5.27: Axial force-displacement graph of *RCB-SLM* simulations at non-impacted end

The axial force-displacements profiles at the non-impacted end are repetitive and show no significant characteristic to the behaviour of the bumper system. Plotting the moving average of the axial force-displacement profiles shows clearer differentiation between the bumper systems. Figure 5.28 shows the moving average axial-force displacement profiles up to the maximum displacement of the impactor. As observed, the axial force experienced at the non-impacted end increases with the increase of wall-thickness of the crossbeams.

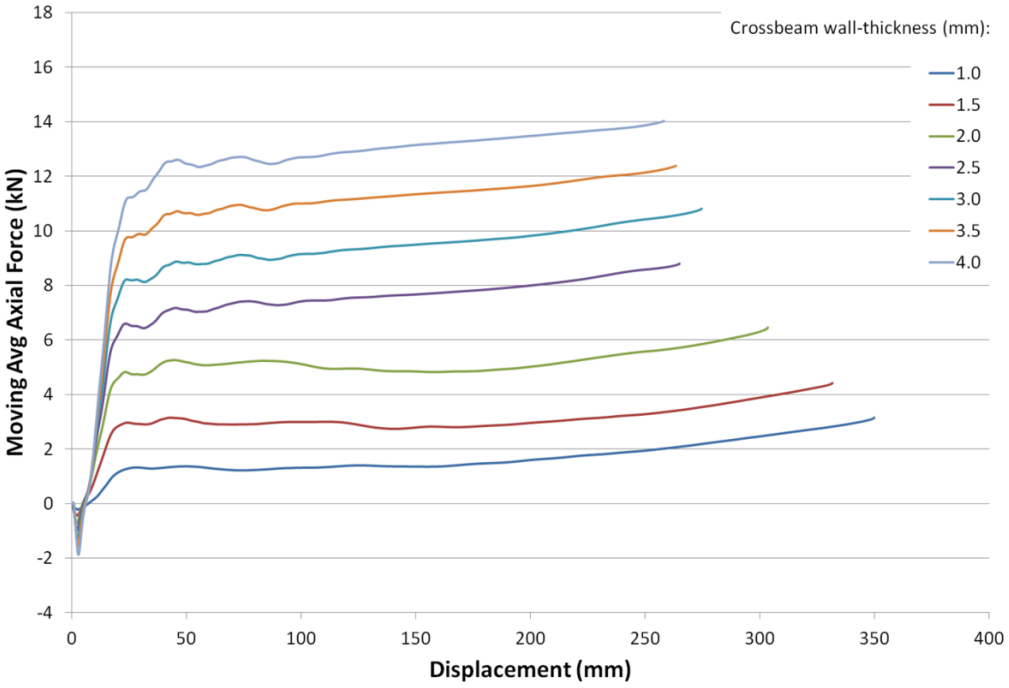

Figure 5.28: Moving average axial force-displacement graph of *RCB-SLM* simulations at non-impacted end

The moving average axial force-displacement profiles of the other grouped simulations show the same behaviour: Increase in force with the increase in wall-thickness of the crossbeams. The plots of the **RCB-TLM**, **CCB-SLM** and **CCB-TLM** can be found in *Appendix D*.

5.3.7.3 Analysis of force calculations

- **Impacted longitudinal member**

The peak force experienced in a structure is important with regards to structural integrity and crashworthiness. The peak force ought to be known when designing the trigger systems for the supplemental restraint systems of a motor vehicle. The design of the subsequent structure from the bumper system should take into account the maximum force that is expected to be transfered.

The peak axial force at the impacted longitudinal member is shown in Figure 5.29 impacted end, the peak axial force shows opposite trends for the two crossbeam profiles. For low wall-thicknesses of the crossbeam, the straight crossbeam (**SCB**) system peak force decreases, whereas the curved crossbeam (**CCB**) systems increase with peak force as the wall-thickness of the crossbeams increases, until a transition value of 2.5mm wall-thickness. Thereafter, the trend reverses for both crossbeam profiled systems. The **CCB** systems deliver a far lower peak force, which is favourable in most design requirements. The mean axial forces of the impacted longitudinal members are shown in Figure 5.30. In general, all of the bumper systems have a similar mean force.

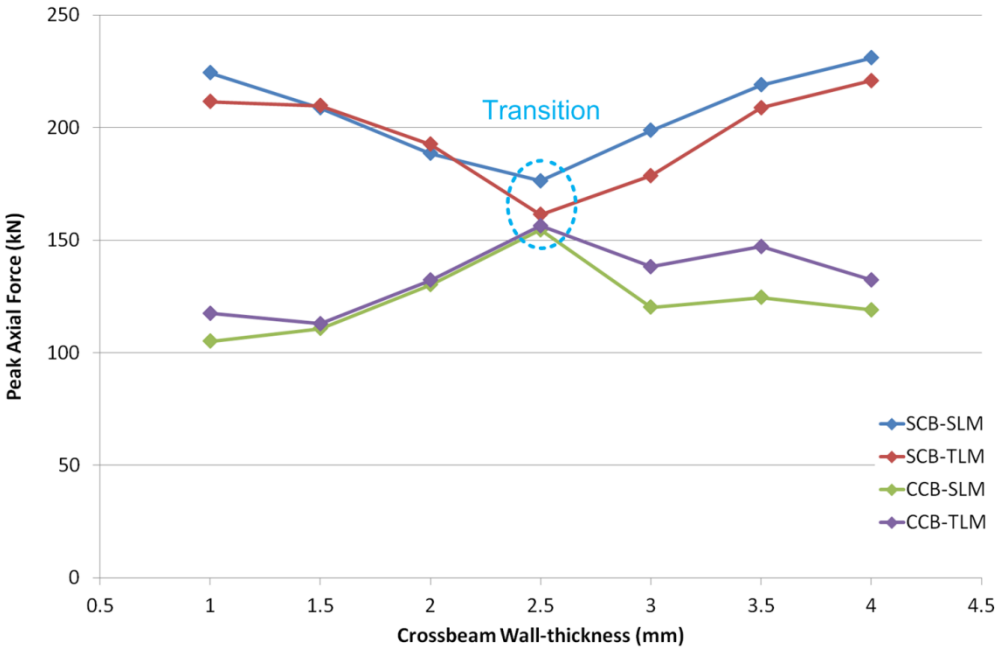

Figure 5.29: Peak axial force vs crossbeam wall-thickness of the impacted longitudinal members

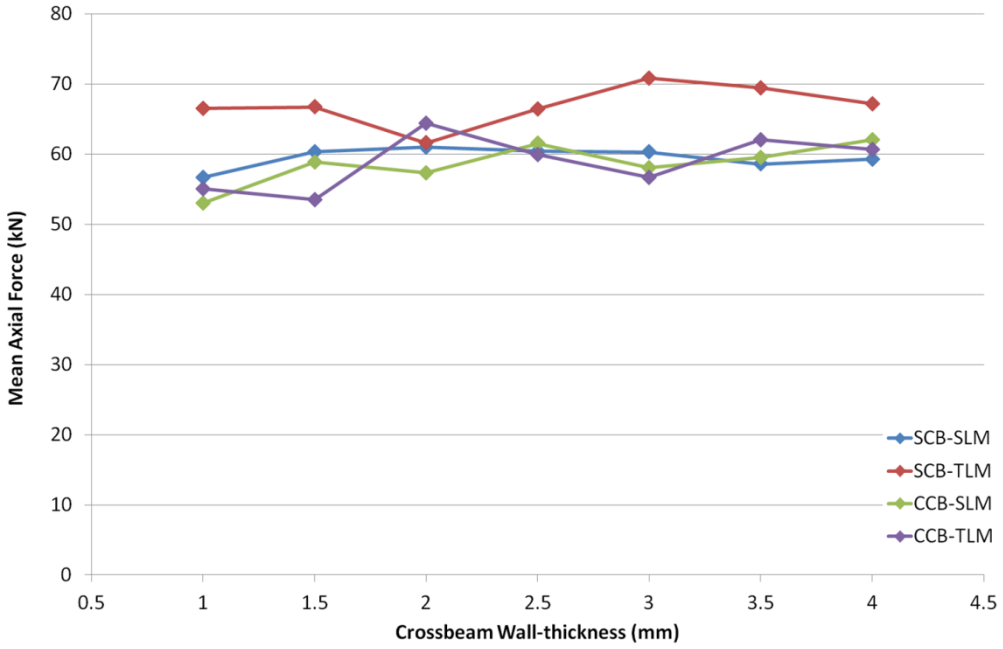

Figure 5.30: Mean force vs wall-thickness of the crossbeam of the impacted longitudinal members

- **Non-impacted longitudinal member**

The peak axial force at the non-impacted longitudinal member increases with the increase in wall-thickness of the crossbeam; shown in Figure 5.31. The mean axial force, Figure 5.32, increases with the increase in wall-thickness of the crossbeam.

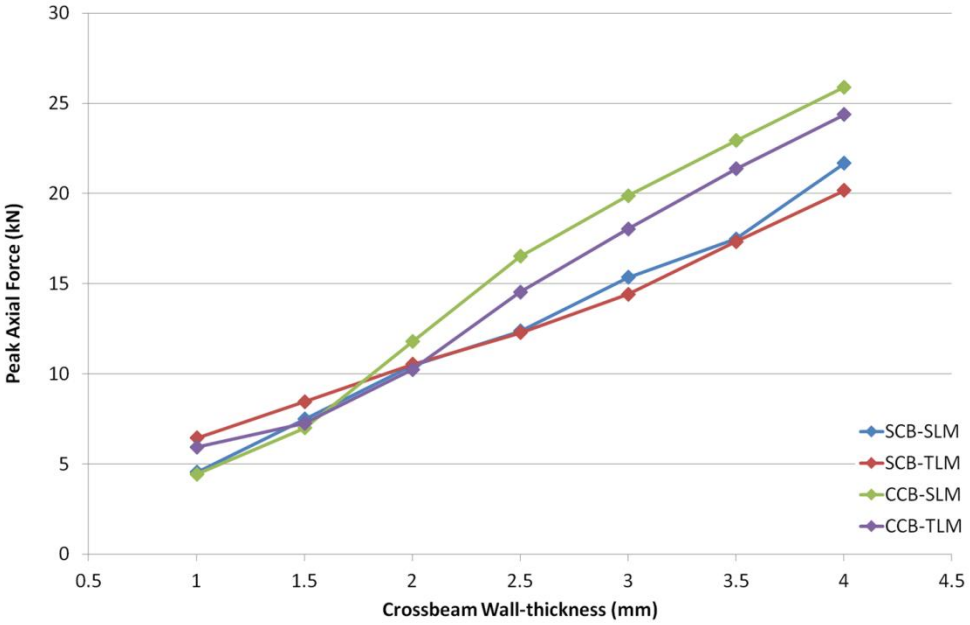

Figure 5.31: Peak force vs wall-thickness of the crossbeam of the non-impacted longitudinal members

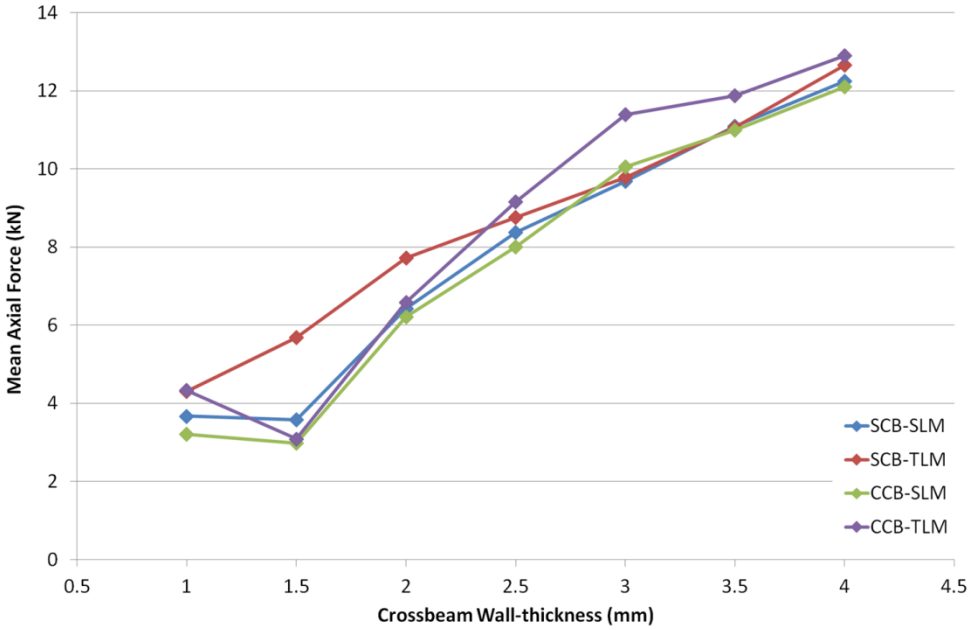

Figure 5.32: Mean force vs wall-thickness of the crossbeam of the non-impacted longitudinal members

The impact energy is dissipated through the crossbeam to the non-impacted longitudinal member, applying more force at the non-impacted end. The peak axial force is higher for the **CCB** systems as there is a high stress concentration area, i.e. *stress-concentrator,* due to the curvature of the interface between the crossbeam and longitudinal member.

5.4 Longitudinal profile parameter

Overall the influence of varying the profile of the longitudinal was not observed to be as significant to the extent of varying the crossbeam parameters has.

5.4.4 Deformation of impacted longitudinal member

Comparing the **CCB-STB** and **CCB-TTB** simulations in Figures 5.10 and 5.12, it is observed that the presence of a tapered side in the longitudinal member presents better deformation characteristics. The stacking of the lobes is more congruous with the vertical axis of the longitudinal member and more symmetric as well. This suggests that tapered members are advantageous to oblique loading conditions, especially those in an offset impact scenario. The skew stacking of the lobes is only common in the bumper systems with the curved crossbeam, and is shown in Figure 5.33 where it is more dominant in bumper systems with straight longitudinal members. The tapered longitudinal members are observed to buckle progressively in a more symmetric and controlled manner than that of straight longitudinal members.

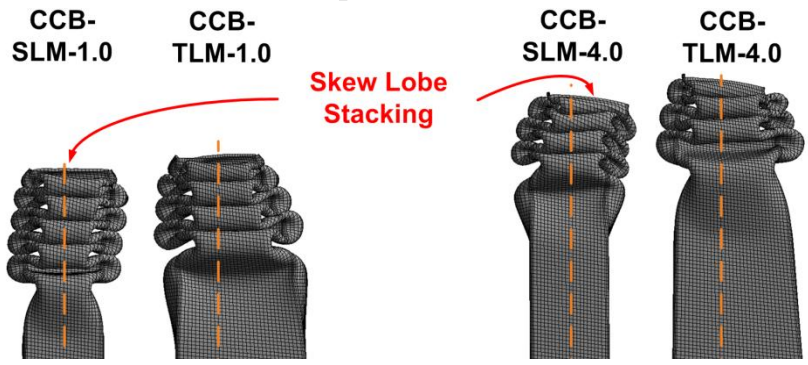

Figure 5.33: Illustration of skew lobe stacking of bumper systems with curved crossbeams (*Front View*)

The simulations with the tapered longitudinal members show similar deformation modes to the simulations with straight longitudinal members. The only discrepancy to the deformation is observed at the impacted end of the **CCB-TLM** bumper systems, as shown in *Appendix B*. The differed deformation is due to the increase in side-wall buckling of the crossbeam that induces a greater bending moment. The tapered longitudinal members perform better under oblique loading with increased stability to oppose the bending

moment. This results in the crossbeam of bumper systems with tapered longitudinal members to deform more with an increase in stability.

5.4.5 Deformation of non-impacted longitudinal member

The deformation of the non-impacted longitudinal member is not observed to be extensive throughout the simulations. However, a local kink of the longitudinal member is observed near the clamped end. The boundary condition at the clamped end induces a bending moment in the bumper system, increasing the stress in this region and resulting in the local kink of the longitudinal member.

The profile of the longitudinal member is offset to its initial vertical plane due to the inward pulling motion. The mode of failure is more prominent in a bumper system with a thin-walled crossbeam member, as greater inward pulling motion incites a higher bending moment. The tapered longitudinal exhibits extended local buckling failure due to the member being more resistant to global bending, thus transferring the load to the clamp end. The increase in wall-thickness of the crossbeam is observed to increase the extent and size of the plastic hinges formed at the interface of the crossbeam and non-impacted longitudinal member, shown in Figure 5.34.

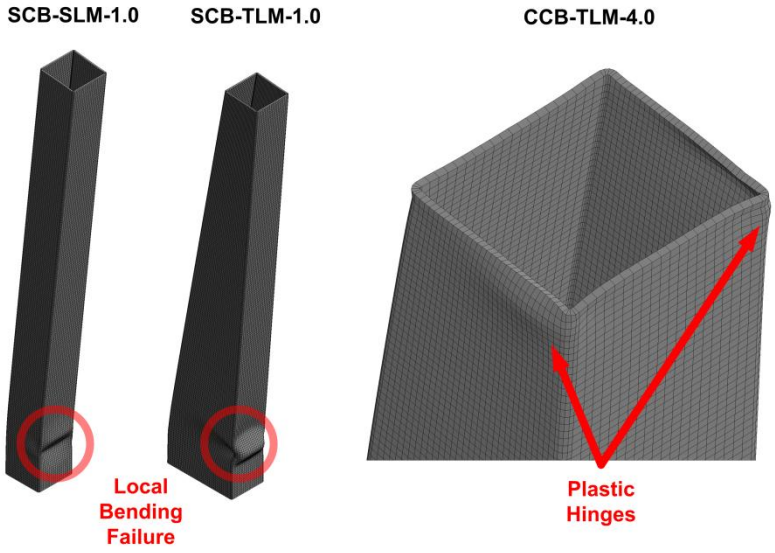

Figure 5.34: Observed deformations of non-impacted longitudinal members

5.4.6 Crush Distance

The variation of the geometric profiles of the longitudinal, affects the crush distance results in several ways. At 1.0mm, the tapered longitudinal bumper systems are observed to have a lower mid-point of crossbeam crush distance than the straight longitudinal, shown in Figure 5.14. However, at the maximum wall-thickness, the bumper systems with straight longitudinal members have lower crush distances than the bumper systems with the corresponding straight longitudinal members. In general, the tapered bumper systems have a slightly lower mid-point crush distance of the crossbeam.

The crush distance at the impacted end, shown in Figure 5.15, between the straight and tapered longitudinal members are relatively comparable with the crush distance slightly lower for the bumper systems with tapered longitudinal members; indicating that the bumper systems with tapered longitudinal members dissipate the energy more through the system.

5.4.7 Energy Absorption

In the bumper system the impacted longitudinal member is the main energy absorbing component. The non-impacted longitudinal members absorbed minor energy when compared to the impacted member. The results of the internal energy absorbed for the longitudinal are summarised in Tables 5.3 to 5.6.

The effect of the longitudinal geometric variation is minor, but the tapered longitudinal systems absorb less energy as they dissipate more energy to the non-impacted member. The internal energy absorbed by the non-impacted longitudinal member is shown in Figure 5.19. Hence, the tapered longitudinal members oppose the bending moment at the interfaces between the crossbeam and longitudinal members more favourably than the straight longitudinal members.

5.4.8 Axial Forces

The axial forces experienced at the clamped ends are recorded and discussed in section 5.3.7. The axial force-displacement profiles, shown in Figure 5.35, from the **RCB-TLM** formulates series with tapered longitudinal members are similar in nature to the **RCB-SLM** simulations with straight longitudinal members.

The effect that the longitudinal profile variation has on the peak force results is only evident after the *transition value*s within a bumper system group. In the **SCB** systems, the straight longitudinal members show a slightly higher peak force than the tapered longitudinal member counterparts as shown in Figure 5.29. The opposite is seen in the **CCB** systems, as the tapered longitudinal members exhibit a higher peak force than the bumper systems with straight longitudinal members. In general, all of the bumper systems have a

similar mean force; the **SCB** systems with tapered longitudinal members experiencing higher mean axial force at the impacted longitudinal members than the other bumper system groups.

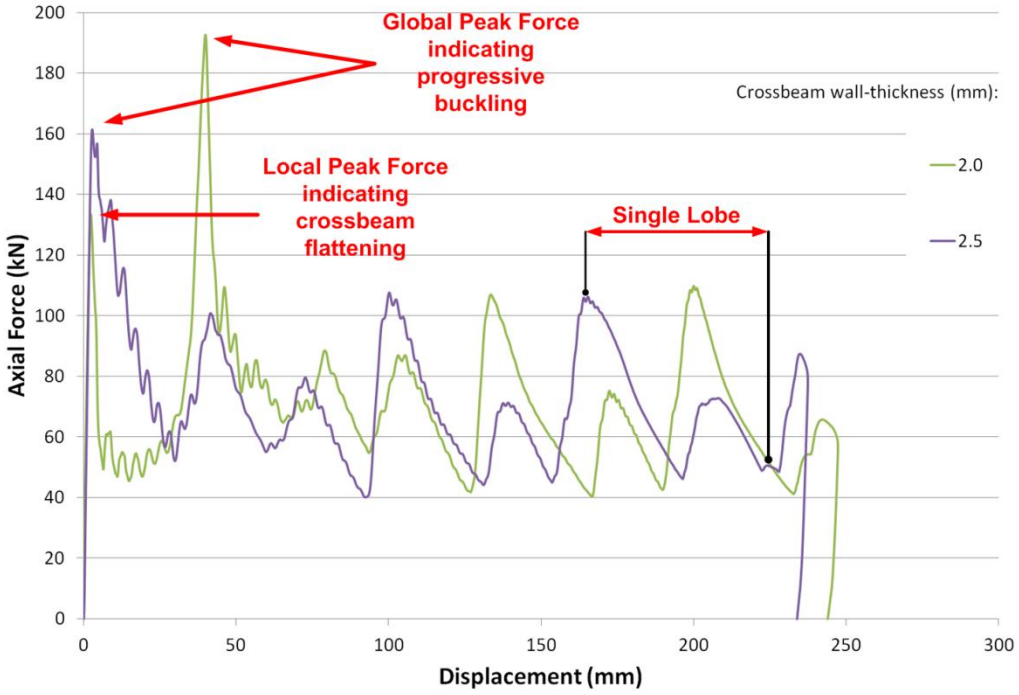

Figure 5.35: Axial force-displacement graph of the *transition value* of RCB-TLM simulations at impacted end

6. Discussions of Study

The objective of the study is to investigate, experimentally and numerically, the influence of varying parameters of a simplified bumper system and the effect on the resulting behaviour and energy absorbing characteristics. These parameters are:

- Wall-thickness of the crossbeams
- Two different crossbeam profiles – straight and curved
- Two different longitudinal profiles – straight and tapered

The bumper system is one of the key structures designed to absorb the energy in an impact scenario. In this study, the impact scenario is chosen to represent an offset impact of 40% of the crossbeam's length. The kinetic energy of the impactor is absorbed by the bumper system through several categorised modes of deformation. The common observed modes of deformation for the two components are:

- Crossbeam:
  - Lateral flattening of crossbeam at impacted end
  - Local bending failure
  - Plastic hinge formation at non-impacted interface
  - Side-wall folding at non-impacted end

- Longitudinal members:
  - Progressive buckling of impacted longitudinal member
  - Local kink of longitudinal members near clamped end

The energy absorbers of the bumper system may differ in their response to similar impact loads when analysed independently. This is the case with the skewed stacking of the lobe formation of the impacted longitudinal members that experienced pull-in motion by the bending crossbeam. Both profiles of longitudinal members are beneficial as energy absorbers since they undergo progressive buckling. This mode has a high initial peak force but show exceptional energy absorbing characteristics.

6.1 Influence of the wall-thickness of the crossbeam

The main parameter investigated is the change in the wall-thickness of the crossbeam. The crossbeam is the first component to make contact with the impactor and, if altered, changes the behavioural outcome of the system.

- **Deformation modes**

Altering the wall-thickness of the crossbeam parameter primarily changes the deformation modes of the crossbeam. The three deformation modes observed of the crossbeam are: lateral flattening, local bending and plastic hinge formation. Increasing the wall-thickness results in less lateral flattening and local bending; due to the crossbeam with thicker walls having an increase in stiffness, i.e. a higher load bearing capacity and greater peak crush force requirement to deform. The interface arrangement between the crossbeam and longitudinal members are inadequate in dissipating the impact energy towards the non-impacted end as plastic hinges are continually formed. The plastic hinge formation, however, increases with the increase in the wall-thickness. As the crossbeam has more load bearing capacity to dissipate the impact energy more broadly through the system, the interface at the non-impact longitudinal and crossbeam experiences more force. Since the interface has a high stress concentration, termed *stress-concentrator*, the plastic hinge forms more readily and to a greater degree. The *stress-concentrator* is shown for the **SCB-SLM** bumper system in Figure 6.1.

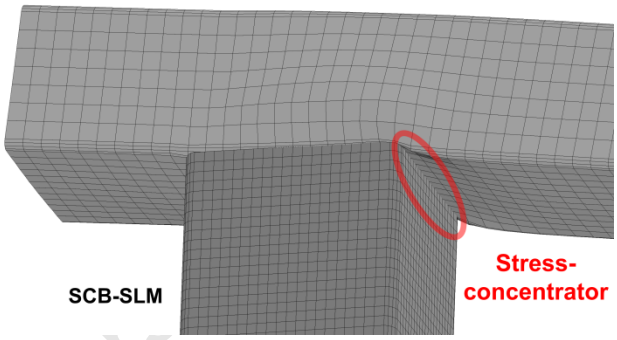

Figure 6.1: Stress-concentrator at non-impacted longitudinal member and crossbeam interface (SCB-SLM)

The deformation of the impacted longitudinal member, the main energy absorbing component, decreases with increase in wall-thicknesses of the crossbeams. The thicker walled crossbeams with higher load bearing capacities absorb more energy and dissipate more energy to the non-impacted longitudinal member. The deformation mode of the impacted longitudinal member does not alter with the wall-thickness of the crossbeam, but the stacking of the progressive buckling lobes is affected. The increase in the wall-thickness of the crossbeam results in the crossbeam being more stiff, decreasing the local bending failure and resisting the pull-in motion by the impactor. The more rigid crossbeam and the pull-in motion for the impactor skews the stacking of the lobes as the longitudinal members are affected by the pull-in motion. The pull-in motion is a consequence of the offset impact scenario having oblique loading conditions.

- **Crush Distance & Energy Absorption**

Increasing the wall-thickness of the crossbeam improves the load bearing capacity of the crossbeam. This improves the energy dissipation of the bumper system as a whole. The crush distance, axial force and energy absorption trend results are related to this energy dissipation.

In the thin wall-thickness range, less than the common *transition value* of ±2.5mm, the crossbeam collapses completely before the impacted longitudinal member deforms. The increase of the wall-thickness increases the load bearing capacity of the crossbeam, allowing it to absorb more energy from the impactor. This in return reduces the crush distance at the impacted end, as well as the peak force for the straight crossbeam (**SCB**) systems.

In all the bumper system groupings, there is a wall-thickness *transition value*, where an abrupt drop or rise is observed in the trends of the results. This *transition value* is related to the maximum load relationship of the crossbeam and impacted longitudinal member. In the thin-walled bumper systems, the crossbeam collapses completely; whereas in the thick-walled bumper systems, the crossbeam only deforms to a certain extent. In between the thin and thick range is a *transition value* where the maximum load property of the crossbeam is nearly equivalent to the initial peak force required to deform the longitudinal member. The transition value is shown in the Figure 6.2. In the SCB systems, the transition value occurs after 2.0mm and in the curved crossbeam (**CCB**) systems, the value is after 2.5mm.

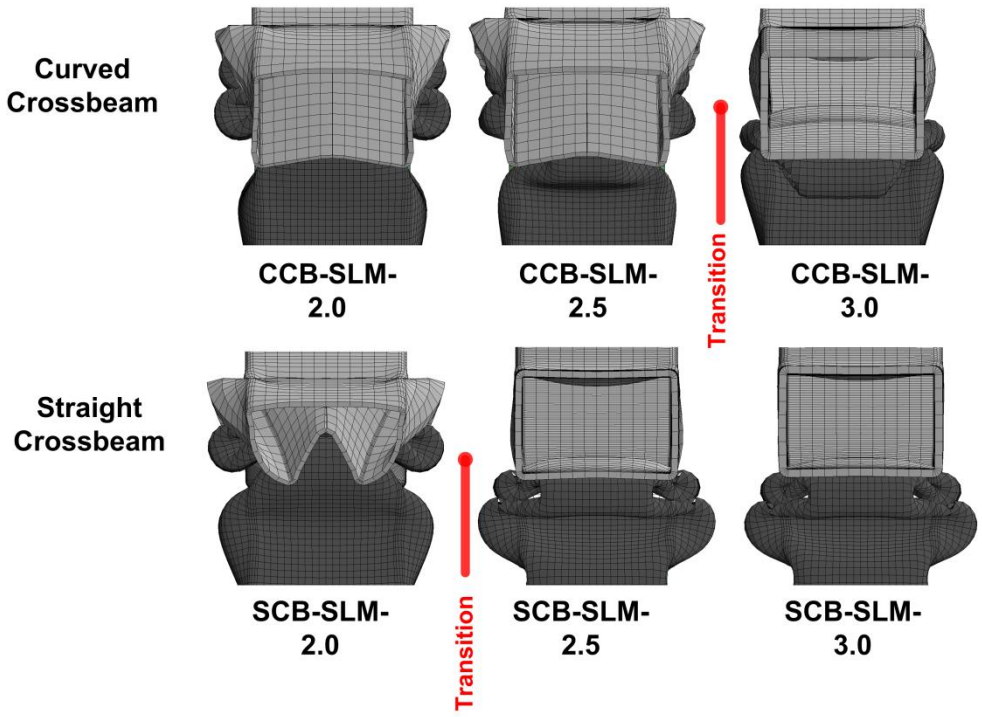

Figure 6.2: Transition value of curved and straight profiled crossbeam bumper systems

In the bumper systems with wall-thicknesses lower than the *transition value*, the crossbeam absorbs more of the impact energy than in the systems with higher wall-thicknesses which is a favourable response. After the wall-thickness *transition value*, the crossbeam has a higher maximum load requirement than that of the longitudinal member; thereby absorbing less of the impact energy and dissipating it to both longitudinal members.

The distribution of kinetic energy absorbed by the components as internal energy in the bumper system is shown in Figure 6.3.

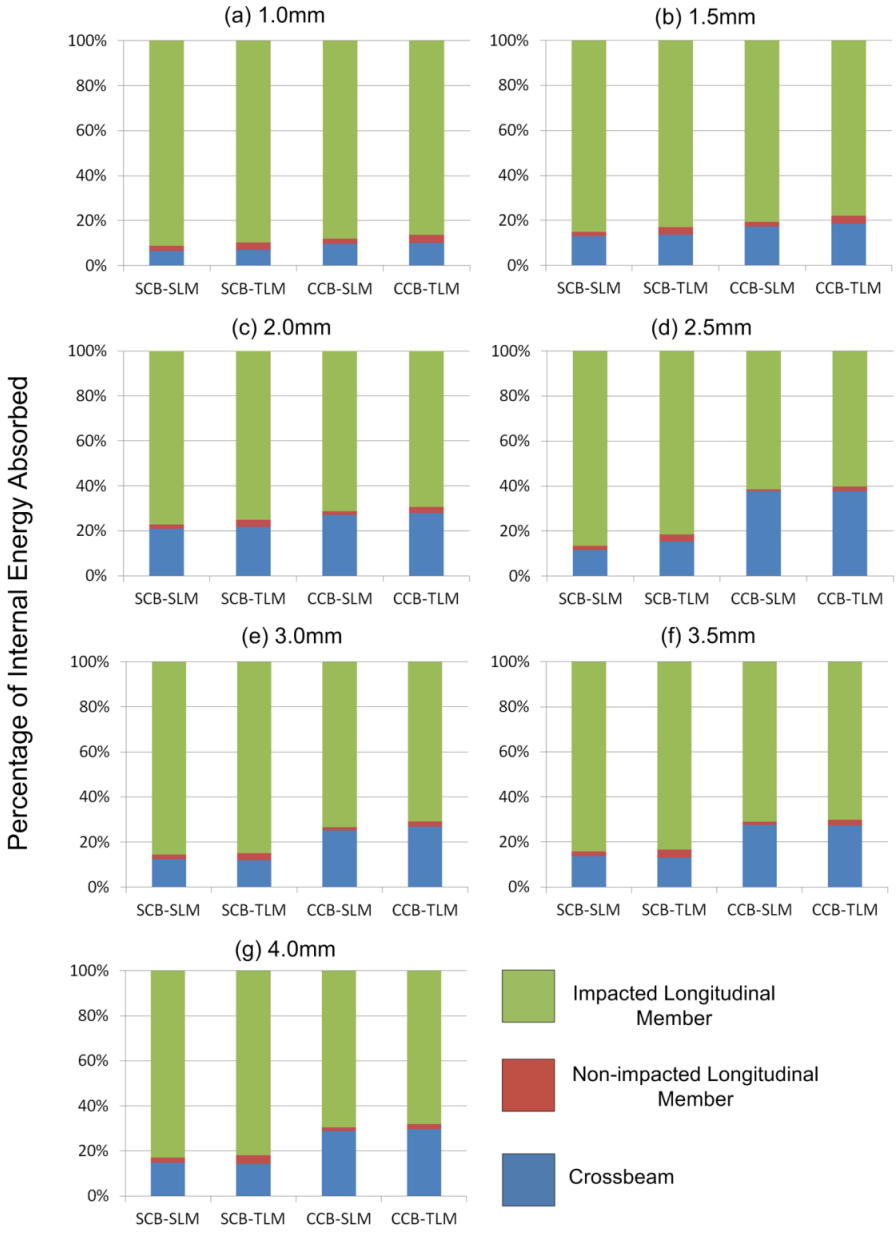

Figure 6.3: Percentage of internal energy absorbed by the bumper system components with crossbeam thickness of: (a) 1.0mm (b) 1.5mm (c) 2.0mm (d) 2.5mm (e) 3.0mm (f) 3.5mm (g) 4.0mm

Figure 6.3 shows the percentage of internal energy absorbed by the three components of the bumper system. Out of all the bumper system configurations, the crossbeam absorbs the most energy in the **CCB-SLM-2.5** bumper; the non-impacted longitudinal member absorbs the most in the **SCB-TLM-4.0** bumper. The impacted longitudinal member absorbs the least amount of energy in the **CCB-TLM-2.5** bumper. These configurations are of particular interest to optimize the energy absorbing capacity of a bumper system.

The peak axial force at the impacted end varies with each wall-thickness alteration. The **SCB** systems show a favourable decrease in the peak force up to the *transition value*, thereafter the peak axial force increases. After the *transition value*, the maximum load requirement of the crossbeam is greater than that of the longitudinal member; therefore the crossbeam deforms less with the increase in the wall-thickness as it becomes more stiff/rigid.

Contradictory behaviour is observed for the **CCB** systems, which tend to increase in peak axial force with the increase in crossbeam, wall-thickness up to the *transition value,* thereafter the peak force decreases with increase in wall-thickness of the crossbeam. The behaviour is due to the curved crossbeam having an additional deformation distance, illustrated in Figure 6.4, until the longitudinal member response come into effect. As a result, the peak axial force increases since the maximum load requirement of the crossbeam increases with the increase in wall-thickness. After the *transition value*, the maximum load requirement of the crossbeam is far higher than that of the longitudinal member; resulting in the longitudinal member deforming at an earlier stage because of the increase in the force transferred to the high stress concentration area at the interface of the crossbeam and longitudinal member. Hence the peak axial force decreases with an increase in wall-thickness of the crossbeam after the *transition value*.

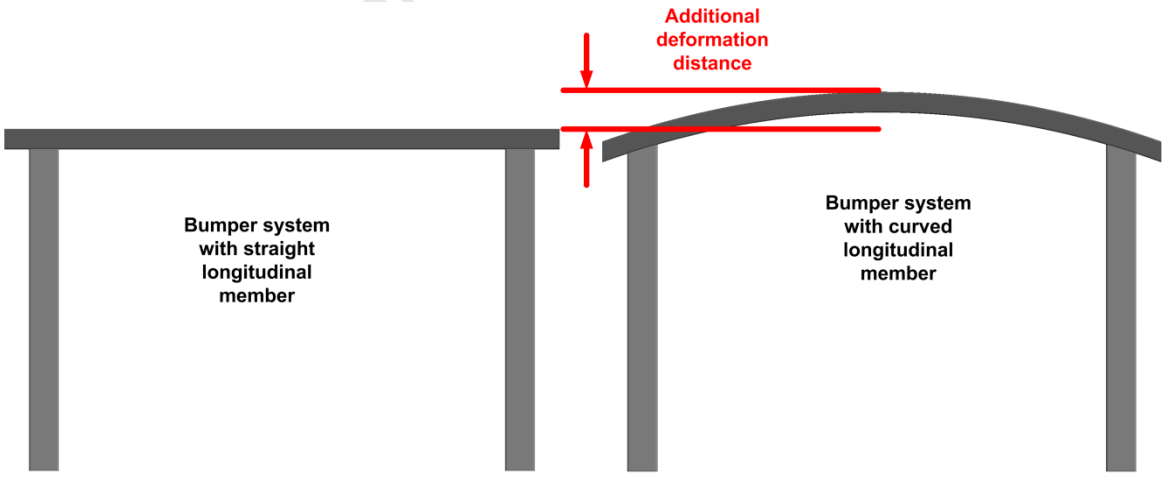

Figure 6.4: Schematic of the additional deformation distance in a bumper system with a curved crossbeam

6.2 Influence of the crossbeam profiles

A distinct difference between the two crossbeam profiles is the axial force results, shown in Figures 5.20 and 5.22. In the straight crossbeam (**SCB**) systems the interface between the crossbeam and longitudinal member is completely horizontal; whereas in the curved crossbeam (**CCB**) systems, the interface is at an angle. The angled interface helps to reduce the peak loads and axial force results considerably; since it is a high stress region where the lower flanges of the crossbeam collapse and the outer walls buckle, as shown in Figure 5.23, as the crossbeam bends. In the very thick walled **CCB** crossbeam systems, the impact energy is dissipated more readily to the longitudinal members, resulting in earlier deformation and lower peak forces.

The **CCB** systems prove to be less effective in dissipating energy to the non-impacted longitudinal member, as a result of the more prominent plastic hinge formed at the high stress concentration area. The angled interface intensifies the *stress-concentrator*, shown in Figure 6.5, and the extended pull-in motion result in a greater plastic hinge being formed, when compared to **SCB** systems. The formation of a plastic hinge at the interface limits the loads and forces being transferred at the non-impacted end of the bumper system.

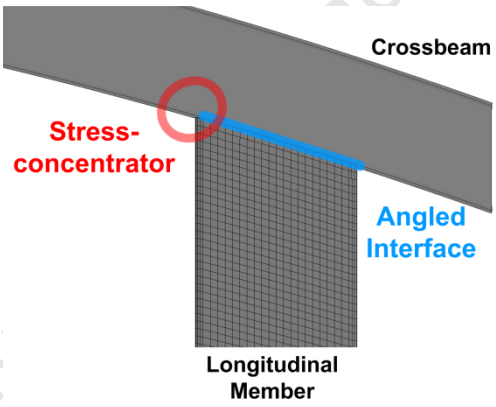

Figure 6.5: Angled interface of curved crossbeam systems

The energy absorbed by the **CCB** systems proves to be far more favourable than the **SCB** systems. The **CCB** systems dissipate more energy away from the impacted longitudinal member, improving the overall energy capacity of the bumper.

6.3 Influence of the longitudinal profiles

The two variations in profile of the longitudinal members show minor differences in the behaviour of the bumper systems under offset impact loading conditions. The energy absorbing characteristics of the bumper systems with tapered longitudinal members show that slightly more energy is absorbed by the crossbeam, i.e. more energy dissipated by the bumper system. More energy is absorbed, shown in Figure 5.18, by the tapered longitudinal members than the corresponding straight longitudinal members while the crush distance at

the impacted end is less for the bumper systems with tapered longitudinal members as shown in Figure 5.15; thereby the tapered longitudinal members are more favourable for the bumper systems.

In an offset impact scenario, the dissipation of impact energy to the whole structure is beneficial. As shown in Figure 5.19 the tapered longitudinal members outperform the straight longitudinal members at dissipating the impact energy. Even the curved crossbeam (**CCB**) systems with the tapered longitudinal members are marginally more effective at dissipating energy to the non-impacted end, shown in Figure 6.3. The study shows that tapered longitudinal outperform straight longitudinal members in offset loading conditions as an energy absorber to a reasonable extent.

7. Conclusions

The influence of the parameters on the behaviour of a simplified bumper system are investigated experimentally and numerically with emphasis on energy absorption characteristics. *As set out in Chapter 1, this study has*:

(1) Designed and constructed a simplified bumper system to be tested experimentally with different parameters (wall-thickness of crossbeam of 1.6mm, 2.0mm and 3.0mm respectively) to validate and calibrate a finite element model.

The experiments are performed in a drop tester replicating a 40% offset impact scenario with three drop masses. The wall-thickness of the crossbeam is the parameter investigated in the experiments. The results from the experiments are used to validate the numerical model.

(2) Developed a numerical model to replicate a simplified bumper system.
(3) Compared the results to the numerical simulations with experiments in terms of the crush distances, deformation modes and transient response for validation.

The numerical model is developed using LS-Dyna 4.2 and uses a well-defined and documented material model, Johnson-Cook, incorporating the effects of strain-hardening and strain rates. The numerical model replicates the results of the experiments favourably, illustrating the same deformation modes, crush distance and similar transient response. The experimental and numerical results are compared.

(4) Numerically performed a parametric study to investigate the influence of the wall-thickness of the crossbeam and two distinct profiles the crossbeams (straight and curved) and longitudinal members (straight and tapered) respectively.

The wall-thickness of the crossbeam is observed to be the most influential parameter as an increase in wall-thickness changes the characteristics of the bumper system; in terms of the initiation and location of deformation, crush distance, the magnitude of the initial peak axial force experienced at the impacted end and the dissipation of the impact energy through the bumper system.

Based on the findings of this investigation, the following conclusions may be drawn:

In terms of design requirements, the following bumper systems performed best based on:

1. Lowest peak force: CCB-SLM-1.0
2. Largest energy absorption capacity: CCB-TLM-2.5
3. Most energy dissipated to crossbeam: CCB-SLM-2.5
4. Most energy dissipated to non-impacted end: SCB-TLM-4.0

In general, the bumper systems with the curved crossbeams show far more favourable behaviour in the study especially resulting in the lowest peak force and highest energy absorbing capacity. The wall-thickness of the crossbeam parameter is the most dominant parameter investigated in this study. The selection of tapered longitudinal members only show a marginal improvement over straight longitudinal members in offset loading conditions.

8. Recommendations

The study improved the understanding of the behaviour of a bumper system and how parameters alter the response; however as a result of the findings and conclusion in this study, some recommendations for further investigations are:

- To quantify the value of the transition value of the wall-thickness of the crossbeam more accurately.

- To improve the design between the interface of the longitudinal members and crossbeam to promote more energy dissipation through the bumper system and minimise the effect the *stress-concentrator* has in forming plastic hinges.

- To investigate discontinuities and buckling initiators in the longitudinal members further and observe the response of the bumper system.

- To investigate the behaviour of a more optimised and efficient designed structure with focus on material selection, manufacturing methods and crash box inclusion.

9. References

[1] EuroNCAP. (est. 1997, accessed 5 July 2011). *EuroNCAP - For Safer Cars*. Available: http://www.euroncap.com

[2] ADAC. (accessed 7 July 2011). *ADAC*. Available: http://www.adac.de/

[3] NHTSA. (accessed 5 July 2011). *NHTSA - National Highway Traffic Safety Administration*. Available: http://www.nhtsa.gov

[4] Volvo Cars Ltd., "Safety instructions for rescue work (only USA)," in *Volvo Car Customer Service* vol. SPJ Instruction No. S88002 + TJ Instruction VCC-376947-5, ed, 2009.

[5] T. Frank and K. Gruber, "Numerical simulation of frontal impact and offset collisions," *CRAZY Channels, Crazy Inc.,* 1992.

[6] S. L. Stucki and W. T. Hollowell, "Determination of frontal offset test conditions based on crash data," *NHSTA R&D,* 1998.

[7] C. A. Hobbs and P. J. McDonough, "Development of the European New Car Assessment Programme (Euro NCAP)," Transport Research Laboratory, United Kingdom1998.

[8] W. Abramowicz, "Thin-walled structures as impact energy absorbers," *Thin-Walled Structures,* vol. 41, pp. 91-107, 2003.

[9] J. M. Alexander, "An approximate analysis of the collapse of thin cylindrical columns," *Quarterly Journal of Mechanics and Applied Mathematics,* vol. 13, pp. 10-15, 1960.

[10] A. G. Pugsley and M. Macaulay, "The large scale crumpling of thin cylindrical columns," *Quarterly Journal of Mechanics and Applied Mathematics,* vol. 13, pp. 1-9, 1960.

[11] W. Abramowicz and N. Jones, "Dynamic axial crushing of circular tubes," *International Journal of Impact Engineering,* vol. 2, pp. 263-281, 1984.

[12] W. Abramowicz and N. Jones, "Dynamic axial crushing of square tubes," *International Journal of Impact Engineering,* vol. 2, pp. 179-208, 1984.

[13] W. Abramowicz and N. Jones, "Dynamic progressive buckling of circular and square tubes," *International Journal of Impact Engineering,* vol. 4, pp. 243-270, 1986.

[14] W. Abramowicz and N. Jones, "Static and dynamic axial crushing of circular and square tubes," in *Metal Forming and Impact Mechanics*, ed Oxford: Pergamon Press, 1985, pp. 225-247.

[15] N. Jones, *Structural Impact*. United Kingdom: Cambridge University Press, 1989.

[16] A. G. Olabi, E. Morris, and M. S. J. Hashmi, "Metallic tube type energy absorbers: A synopsis," *Thin-Walled Structures,* vol. 45, pp. 706-726, 2007.

[17] Ø. Jensen, M. Langseth, and O. S. Hopperstad, "Experimental investigations on the behaviour of short to long square aluminium tubes subjected to axial loading," *International Journal of Impact Engineering,* vol. 30, pp. 973-1003, 2004.

[18] K. R. F. Andrews, G. L. England, and E. Ghani, "Classification of the axial collapse of circular tubes under quasi-static loading," *International Journal Mechanical Sciences,* vol. 25, pp. 687–96, 1983.

[19] S. Chung Kim Yuen, "The effects of blast-induced imperfections on the energy absorption characteristics of square tubes," PhD Thesis, Department of Mechanical Engineering, University of Cape Town, 2006.

[20] W. Abramowicz and N. Jones, "Transition from initial global bending to progressive buckling of tubes loaded statically and dynamically," *International Journal of Impact Engineering,* vol. 19, pp. 415–37, 1997.

[21] M. Alves and D. Karagiozova, "Dynamic global and progressive buckling of circular shells under impact loads," in *Plasticity, damage and fracture at macro, micro and nano scales*, ed Maryland, USA: Neat Press, 2002, pp. 621–623.

[22] O. Jensen, M. Langseth, and O. S. Hopperstad, "Transition between progressive and global buckling of aluminium extrusions," *Structures under shock and impact VII, WIT Press,* pp. 269–277, 2002.

[23] S. S. Hsu and N. Jones, "Quasi-static and dynamic axial crushing of thin-walled circular stainless steel, mild steel and aluminium alloy tubes," *International Journal of Crashworthiness,* vol. 9, pp. 195–214, 2004.

[24] D. Karagiozova and M. Alves, "Transition from progressive buckling to global bending of circular shells under axial impact—part I: experimental and numerical observations," *Int. J. Solids Structures,* vol. 41, pp. 1565–1580, 2004.

[25] D. Karagiozova, M. Alves, and N. Jones, "Inertia effects in axisymmetrically deformed cylindrical shells under axial impact," *International Journal of Impact Engineering,* vol. 24, pp. 1083-1115, 2000.

[26] D. Karagiozova and N. Jones, "On the mechanics of the global bending collapse of circular tubes under dynamic axial load—Dynamic buckling transition," *International Journal of Impact Engineering,* vol. 35, pp. 397–424, 2008.

[27] J. DeRuntz and P. Hodge, "Crushing of a tube between rigid plates," *Journal of Applied Mechanics, Transactions of ASME,* vol. 30, pp. 391-395, 1963.

[28] S. Reid and T. Reddy, "Effect of strain hardening on the lateral compression of tubes between rigid plates," *International Journal of Solids Structures,* vol. 14, pp. 213-225, 1978.

[29] A. Sherbourne and F. Lu, "Strain hardening in the moving hinge method," *International Journal of Solids Structures,* vol. 30, pp. 3475-3489, 1993.

[30] E. Morris, A. G. Olabi, and M. S. J. Hashmi, "FE simulation and experimentation of nested systems under static and impact loading conditions," in *Proceedings of the 12th international conference on experimental mechanics*, Bari, Italy, 2004, pp. 196-203.

[31] R. Sowerby, W. Johnson, and S. Samanta, "The diametric compression of circular rings by ‘‘point’’ loads," *International Journal of Mechanical Sciences,* vol. 10, pp. 369-383, 1968.

[32] A. R. Watson, S. R. Reid, W. Johnson, and S. G. Thomas, "Large deformation of thinwalled circular tubes under transverse loading," *International Journal Mechanical Sciences,* vol. 18, pp. 387-396, 1976.

[33] W. Johnson and A. C. Walton, "Protection of car occupants in frontal impact with heavy lorries: frontal structures," *International Journal of Impact Engineering,* vol. 1, pp. 111-123, 1983.

[34] W. Johnson and A. C. Walton, "An experimental investigation of the energy dissipation car bumpers under quasi-static lateral loads," *International Journal of Impact Engineering,* vol. 1, pp. 301-308, 1983.

[35] Y. Jing and D. Barton, "The response of square cross-section tubes under lateral impact loading," *International Journal of Crashworthiness,* vol. 3, 1998.

[36] S. Chung Kim Yuen and G. N. Nurick, "The energy-absorbing characteristics of tubular structures with geometric and material modifications: An overview," *Applied Mechanics Review,* vol. 61, p. 15, 2008.

[37] S. B. Bodlani, S. Chung Kim Yuen, and G. N. Nurick, "The energy absorption characteristics of square mild steel tubes with multiple induced circular hole discontinuities - part II: numerical simulations," *Journal of Applied Mechanics,* vol. 76, p. 10, 2009.

[38] Constellium. (2011, 30 July). *Innovations for crash management systems*. Available: http://www.constellium.com/innovation-at-constellium/innovation-success-stories/innovations-for-crash-management-systems

[39] D. Bonorchis, "Analysis and simulation of welded plates subjected to blast loading," PhD Thesis, Department of Mechanical Engineering, University of Cape Town, 2007.

[40] R. Hosseinzadeh, M. M. Shokrieh, and L. B. Lessard, "Parametric study of automotive composite bumper beams subjected to low-velocity impacts," *Composite Structures,* vol. 68, pp. 419-427, 2005.

[41] S. S. Cheon, J. H. Choi, and D. G. Lee, "Development of composite bumper beam for passenger cars," *Composite Structures,* vol. 32, pp. 491-499, 1995.

[42] P. Simon and P. D. Beggs, "A numerical performance comparison of a dual-phase steel and aluminium alloy bumper bar system," *International Journal of Crashworthiness,* vol. 15, pp. 425-442, 2010.

[43] F. Jenefeldt, "Investigating the effects of strengthening the crossbeam in frontal car-to-car impacts," *International Journal of Crashworthiness,* vol. 13, pp. 1-8, 2008.

[44] G. M. Nagel, "Impact and energy absorption of straight and tapered rectangular tubes," PhD Thesis, School of Civil Engineering, Queensland University of Technology, 2005.

[45] A. G. Hanssen, L. Lorenzi, K. K. Berger, O. S. Hopperstad, and M. Langseth, "A demonstrator bumper system based on aluminium foam filled crash boxes," *International Journal of Crashworthiness,* vol. 5, pp. 381-392, 2000.

[46] A. G. Hanssen, M. Langseth, and O. S. Hopperstad, "Static and dynamic crushing of square aluminium extrusions with aluminium foam filler," *International Journal of Impact Engineering,* vol. 24, pp. 347-383, 2000.

[47] S. Kokkula, "Bumper beam-longitudinal system subjected to offset impact loading: An experimental and numerical study," PhD, Department of Structural Engineering, Norwegian University of Science and Technology, Trondheim, Norway, 2005.

[48] S. Kokkula, O. S. Hopperstad, O. G. Lademo, T. Berstad, and M. Langseth, "Offset impact behaviour of bumper beam-longitudinal systems: numerical simulations," *International Journal of Crashworthiness,* vol. 11, pp. 317-336, 2005.

[49] S. Kokkula, O. S. Hopperstad, M. Langseth, and O. G. Lademo, "High speed offset impact behaviour of an automotive bumper beam-longitudinal system," presented at the IMPLAST 2007, Bochum, Germany, 2007.

[50] S. Kokkula, M. Langseth, O. S. Hopperstad, and O. G. Lademo, "Behaviour of an automotive bumper beam-longitudinal system at 40% offset impact: an experimental and numerical study," *Latin American Journal of Solids and Structures,* vol. 3, pp. 59-73, 2006.

[51] A. G. Hanssen, T. Auestad, T. Tryland, and M. Langseth, "The kicking machine: A device for impact testing of structural components," *International Journal of Crashworthiness,* vol. 8, pp. 385-392, 2003.

[52] M. G. Cockcroft and D. J. Latham, "Ductility and workability of metals," *Journal of the Institute of Metals,* vol. 96, pp. 33-39, 1968.

[53] G. M. Nagel and D. P. Thambiratnam, "A numerical study on the impact response and energy absorption of tapered thin-walled tubes," *International Journal Mechanical Sciences,* vol. 46, pp. 201-216, 2004.

[54] G. M. Nagel and D. P. Thambiratnam, "Dynamic simulation and energy absorption of tapered thin-walled tubes under oblique impact loading," *International Journal Mechanical Sciences,* vol. 32, pp. 1695-1620, 2006.

[55] S. B. Bodlani, S. Chung Kim Yuen, and G. N. Nurick, "The energy absorption characteristics of square mild steel tubes with multiple induced circular hole discontinuities - part I: experiments," *Journal of Applied Mechanics,* vol. 76, p. 041012, 2009.

[56] *LS-DYNA: Keyword User's Manual* vol. 1, version 971. Livermore, California: Livermore Software Technology Corporation (LSTC), 2007.

[57] J. O. Hallquist, "LS-Dyna Theory Manual," ed. Livermore, California: Livermore Software Technology Corporation, 2006.

[58] G. R. Johnson and W. H. Cook, "A constitutive model and data for metals subjected to large strains, high strain rates and high temperatures," in *Proceedings of the Seventh International Symposium on Ballistics*, The Hague, 1983, pp. 541-547.

[59] J. E. Shigley and C. R. Mischke, *Mechanical Engineering Design*, 6th Metric Edition ed.: McGraw Hill, 2003.

[60] S. T. Marais, "Development and proving of a split hopkinson pressure bar used for high strain rate materials testing," Master Thesis, Department of Mechanical Engineering, University of Cape Town, 2001.

[61] R. Govender, BISRU, University of Cape Town, 2011.

[62] Y. C. Lin, X.-M. Chen, and G. Liu, "A modified Johnson-Cook model for tensile behaviors of typical high-strength alloy steel," *Materials Science and Engineering A,* vol. 527, pp. 6980-6986, 2010.

[63] A. Reyers, M. Langseth, and O. S. Hopperstad, "Crashworthiness of aluminium extrusions subjected to oblique loading: experiments and numerical analysis," *International Journal of Impact Engineering,* vol. 44, pp. 1965-1984, 2002.

10. Appendices

A. Element Size Variations of Longitudinal Member

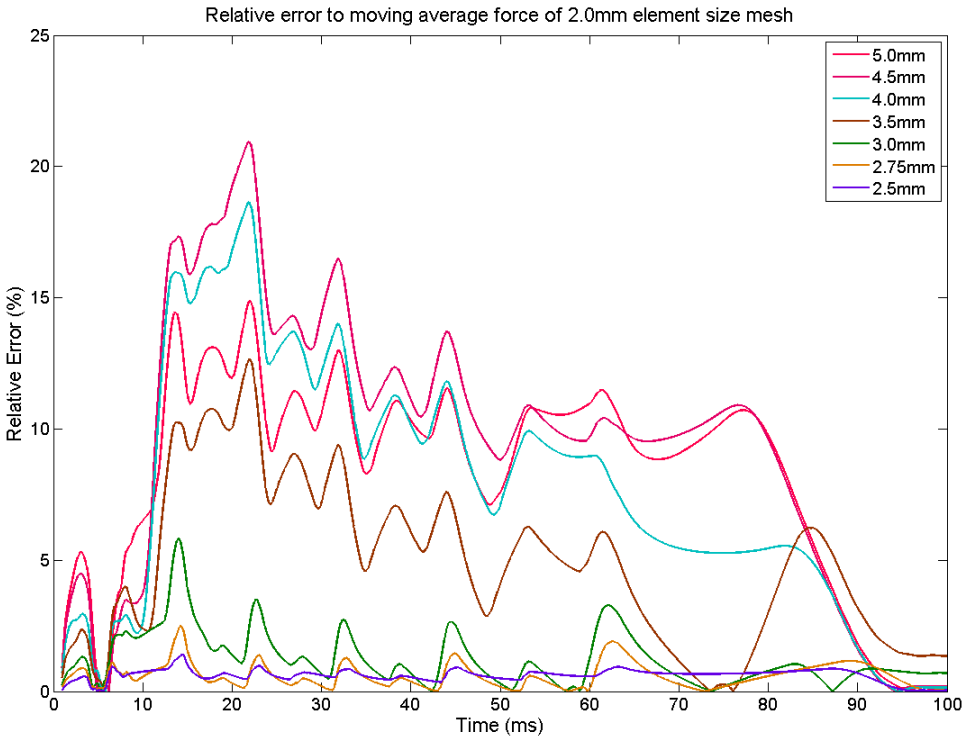

Figure 10.1: Relative error to moving average force of 2.0mm element mesh size

B. Deformed Crossbeam Component

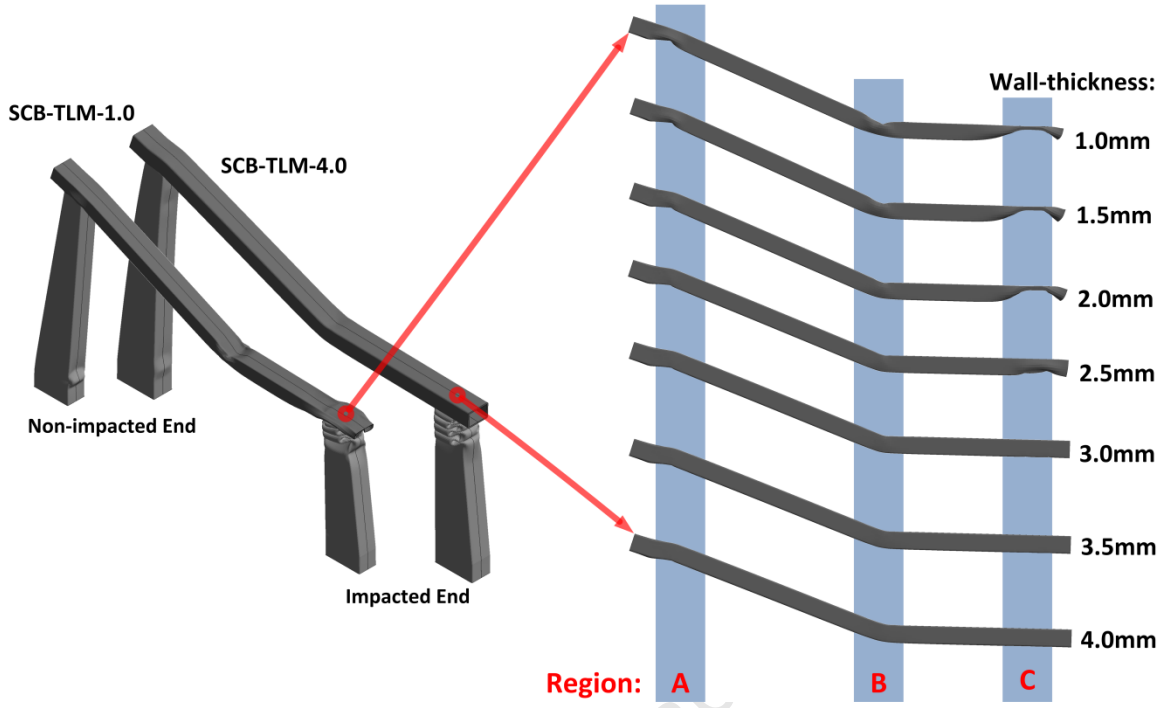

Figure 10.2: Deformed shapes of the crossbeam component from the *SCB-TLM* simulations

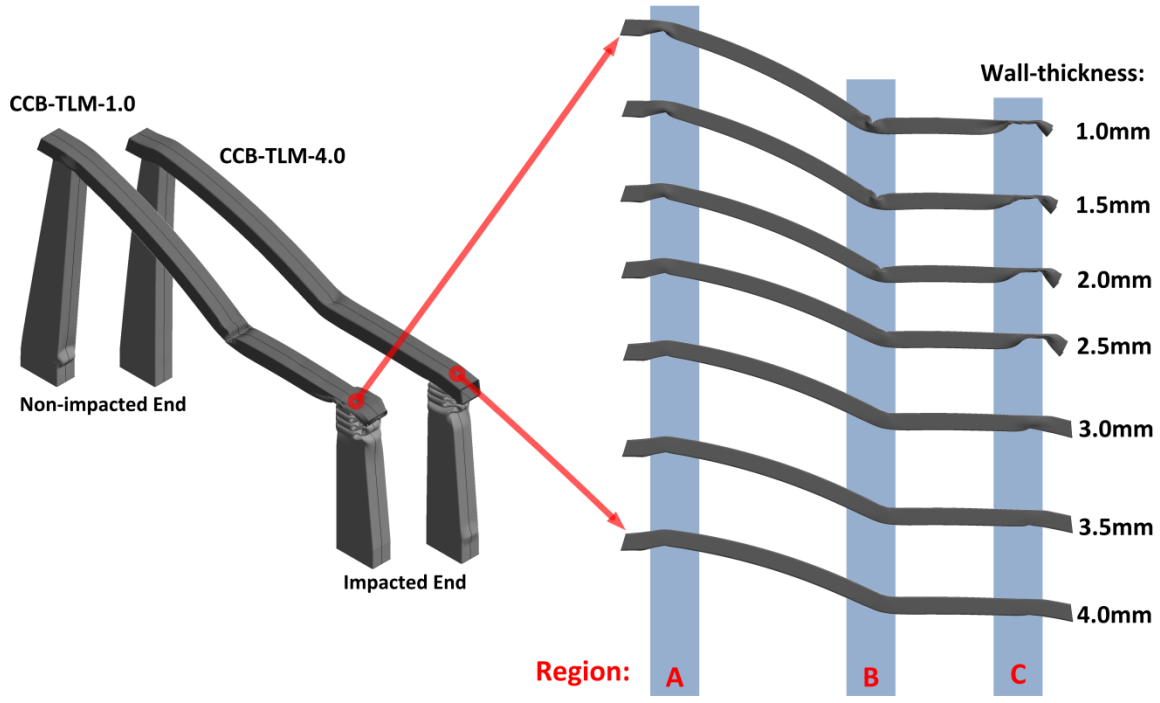

Figure 10.3: Deformed shapes of the crossbeam component from the *CCB-TLM* simulations

C. Crush Distance Calculations

ID	Crossbeam Mid-point (mm)	Flex Point (mm)	Impacted End (mm)	Impacted longitudinal member (mm)
SCB-SLM-1.0	226.4	285.8	281.6	243.4
SCB-SLM-1.5	208.3	263.9	259.2	221.7
SCB-SLM-2.0	195.9	249.9	247.9	212.0
SCB-SLM-2.5	194.7	244.3	244.1	243.3
SCB-SLM-3.0	189.9	236.4	238.2	237.8
SCB-SLM-3.5	183.7	225.7	229.8	229.4
SCB-SLM-4.0	159.2	217.6	224.2	223.8

Table 10.1: Crush distance results of *RCB-SLM* simulations

ID	Crossbeam Mid-point (mm)	Flex Point (mm)	Impacted End (mm)	Impacted longitudinal member (mm)
SCB-TLM-1.0	207.5	262.6	262.2	223.7
SCB-TLM-1.5	205.6	258.9	258.2	220.3
SCB-TLM-2.0	194.5	244.4	243.0	206.8
SCB-TLM-2.5	185.1	232.1	233.4	224.5
SCB-TLM-3.0	182.4	226.7	228.8	228.3
SCB-TLM-3.5	179.1	219.3	223.8	223.3
SCB-TLM-4.0	176.7	213.5	220.1	219.7

Table 10.2: Crush distance results of *RCB-TLM* simulations

ID	Crossbeam Mid-point (mm)	Flex Point (mm)	Impacted End (mm)	Impacted longitudinal member (mm)
CCB-SLM-1.0	291.2	356.1	277.5	248.4
CCB-SLM-1.5	276.9	341.7	259.0	222.7
CCB-SLM-2.0	250.1	311.8	231.4	195.8
CCB-SLM-2.5	214.9	267.6	220.7	159.3
CCB-SLM-3.0	223.6	275.7	202.1	199.0
CCB-SLM-3.5	213.4	263.1	191.2	188.6
CCB-SLM-4.0	209.3	254.7	186.0	184.2

Table 10.3: Crush distance results of *CCB-SLM* simulations

ID	Crossbeam Mid-point (mm)	Flex Point (mm)	Impacted End (mm)	Impacted longitudinal member (mm)
CCB-TLM-1.0	281.4	345.3	265.9	228.2
CCB-TLM-1.5	267.6	330.0	249.5	213.3
CCB-TLM-2.0	238.4	297.7	218.1	182.7
CCB-TLM-2.5	212.3	264.1	190.7	156.0
CCB-TLM-3.0	212.3	262.1	189.2	183.0
CCB-TLM-3.5	209.0	257.5	184.7	182.6
CCB-TLM-4.0	199.8	244.7	174.0	172.2

Table 10.4: Crush distance results of *CCB-TLM* simulations

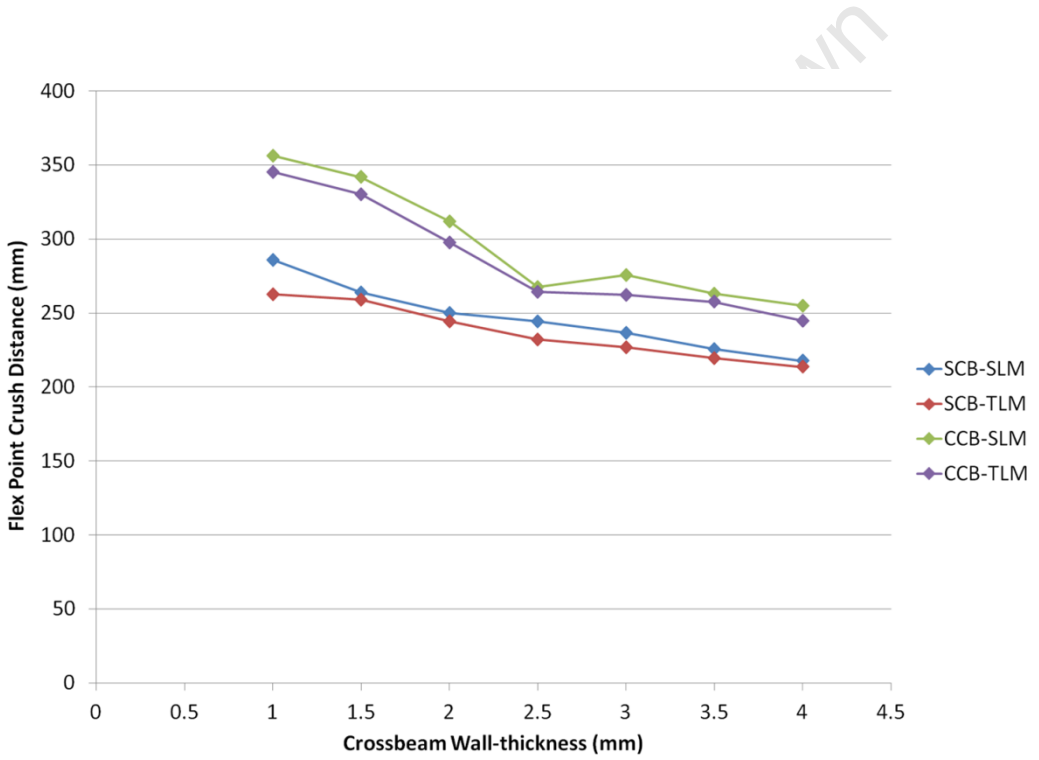

Figure 10.4: Flex point crush distance vs wall-thickness of all bumper systems

D. Axial Force-Displacement Graphs

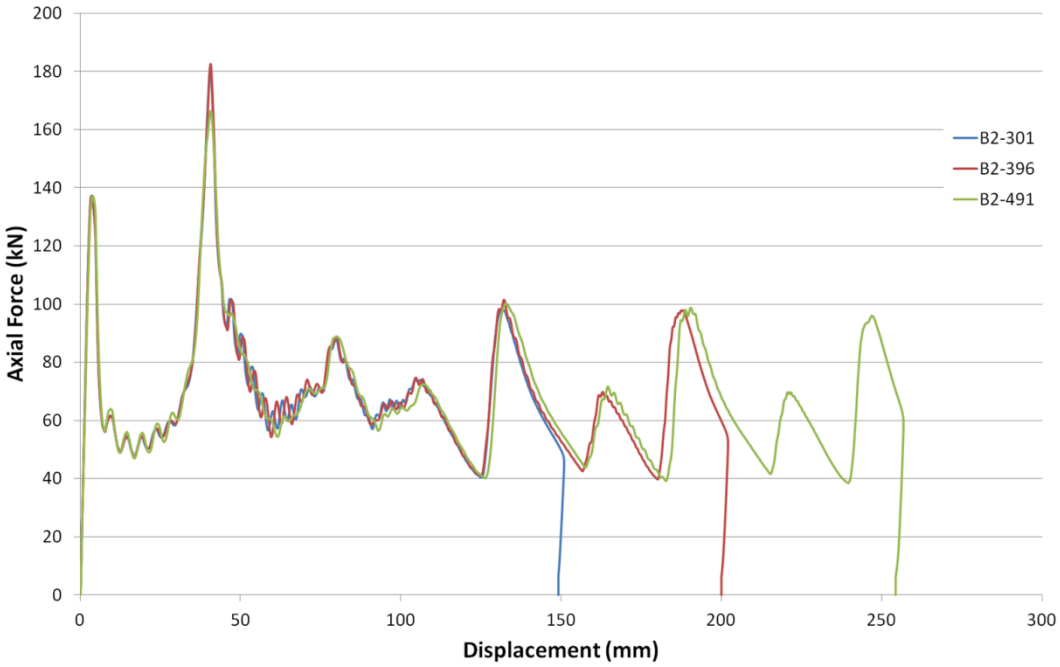

Figure 10.5: Axial force-displacement graph of B2 group numerical models at impacted end

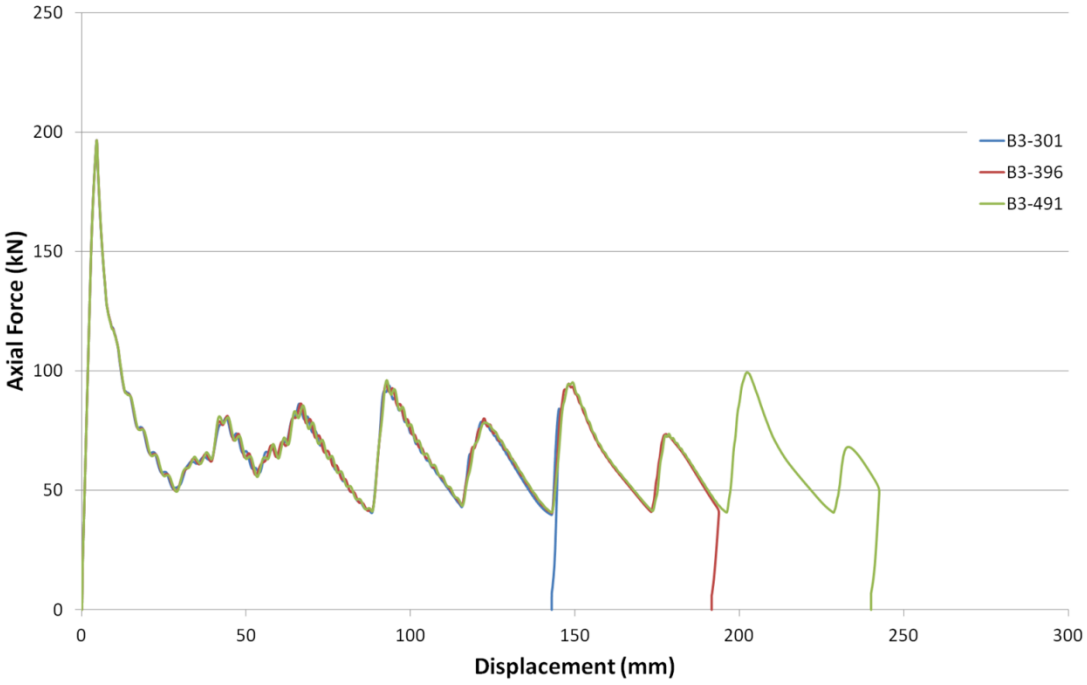

Figure 10.6: Axial force-displacement graph of B3 group numerical models at impacted end

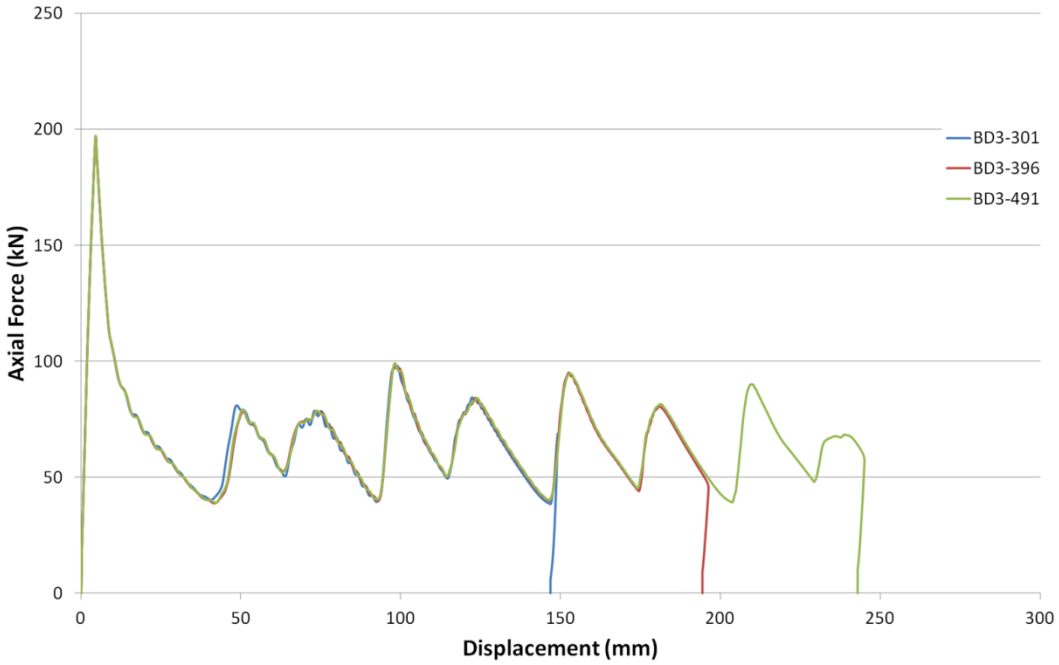

Figure 10.7: Axial force-displacement graph of BD3 group numerical models at impacted end

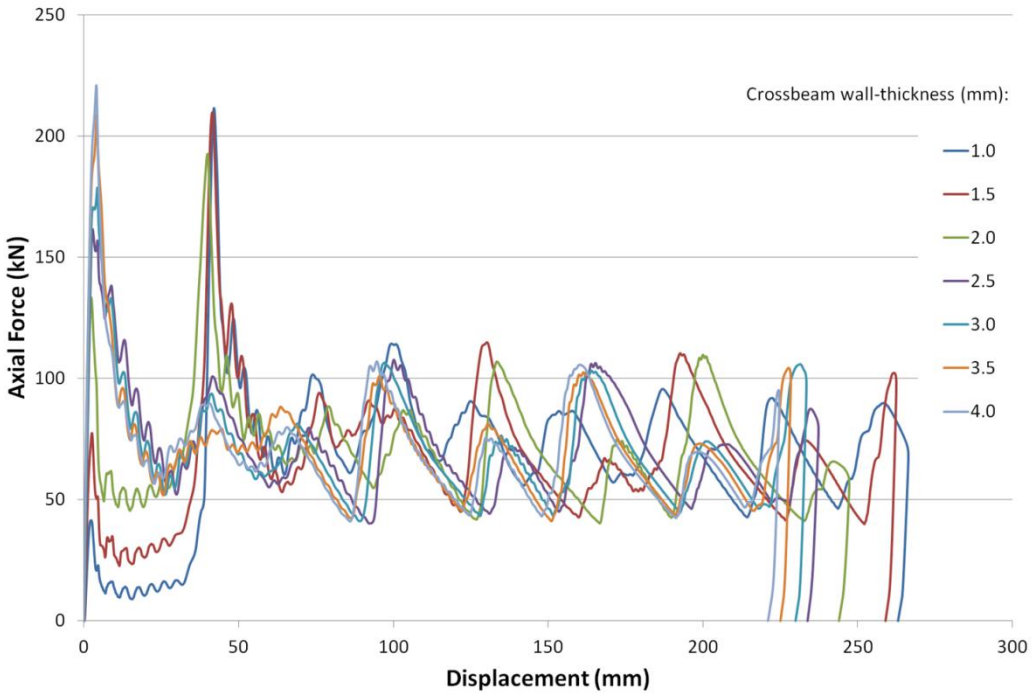

Figure 10.8: Axial force-displacement graph of RCB-TLM simulations at impacted end

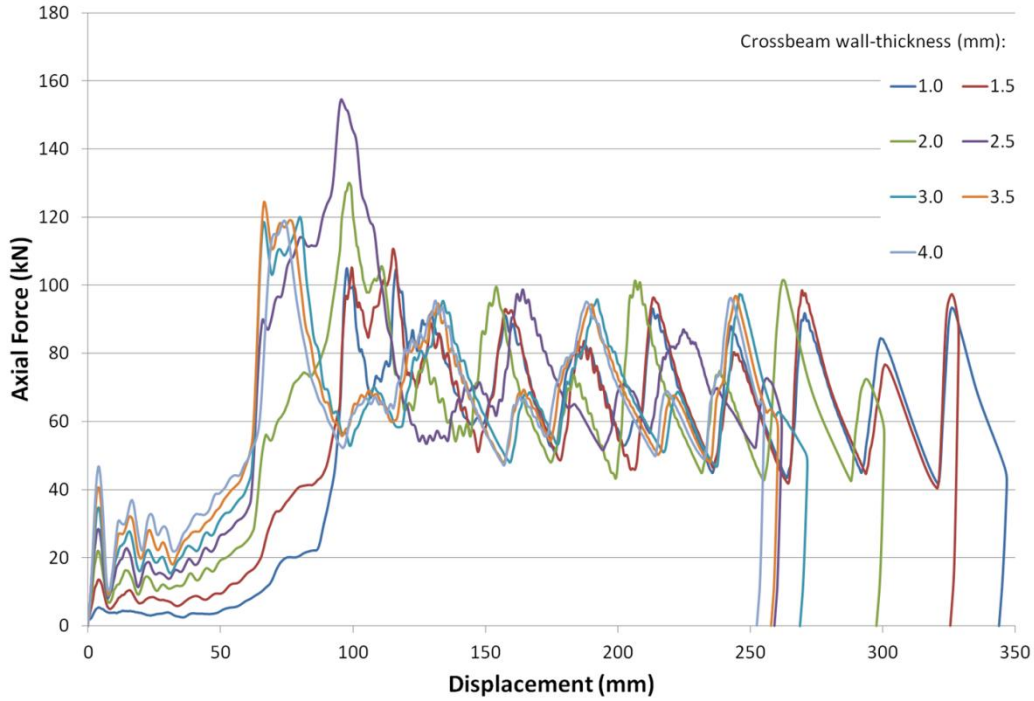

Figure 10.9: Axial force-displacement graph of CCB-SLM simulations at impacted end

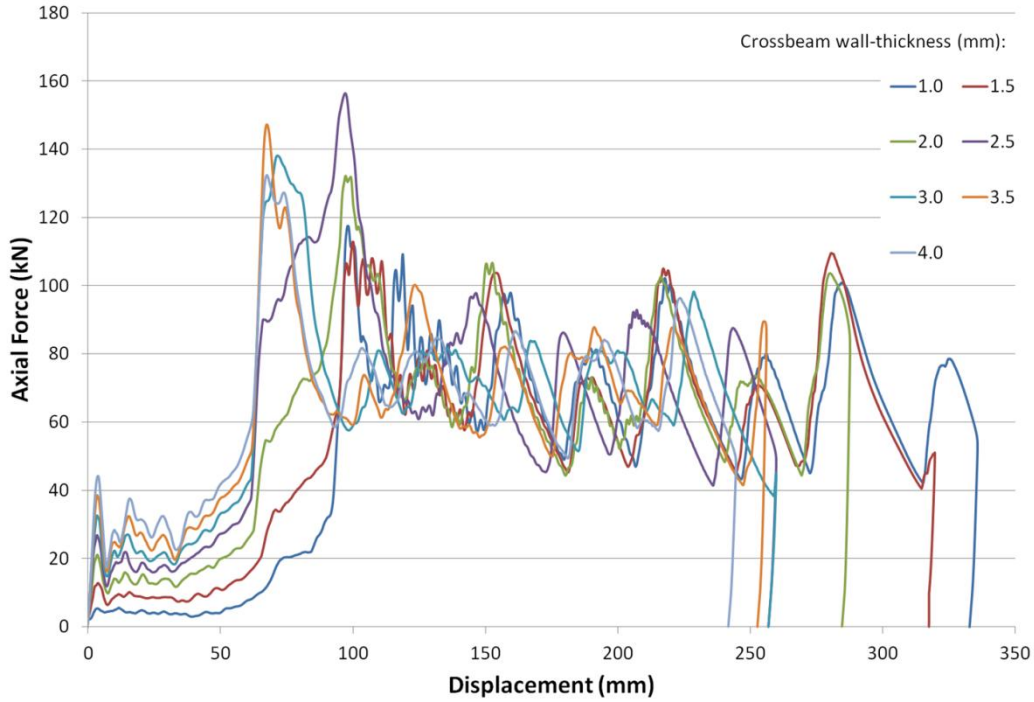

Figure 10.10: Axial force-displacement graph of *CCB-TLM* simulations at impacted end

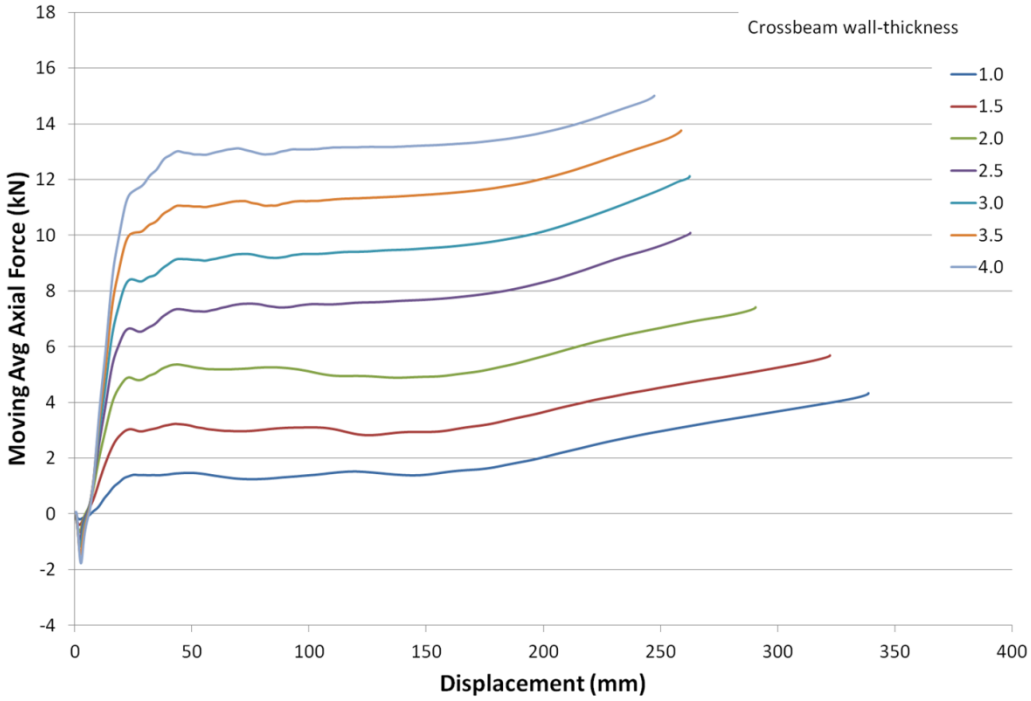

Figure 10.11: Moving average axial force-displacement graph of *RCB-TLM* simulations at non-impacted end

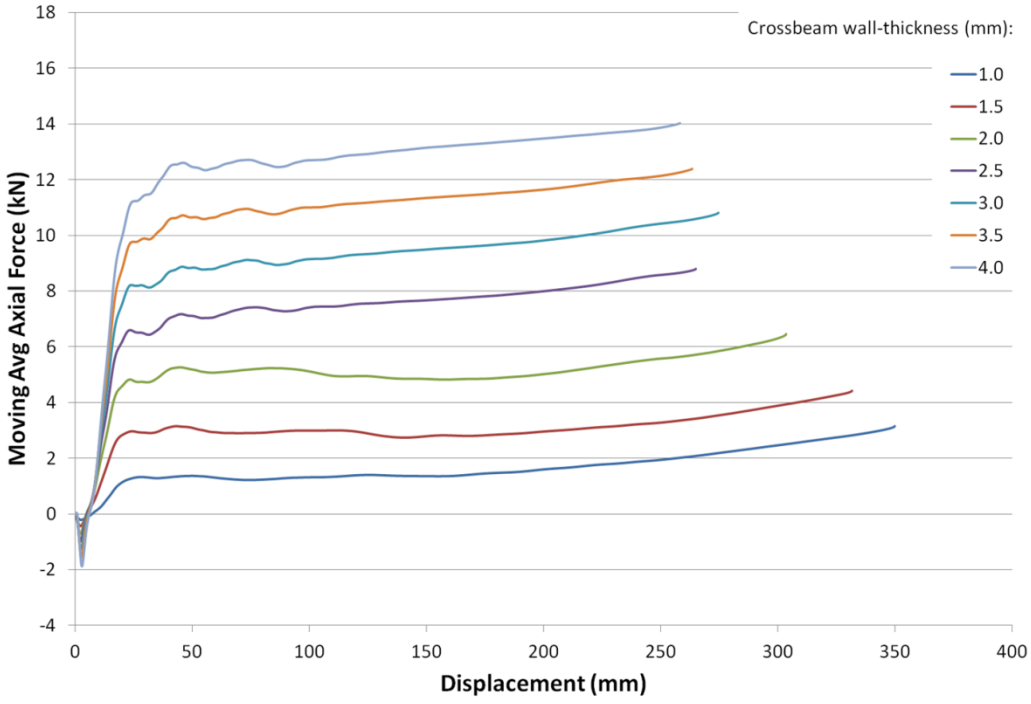

Figure 10.12: Moving average axial force-displacement graph of *CCB-SLM* simulations at non-impacted end

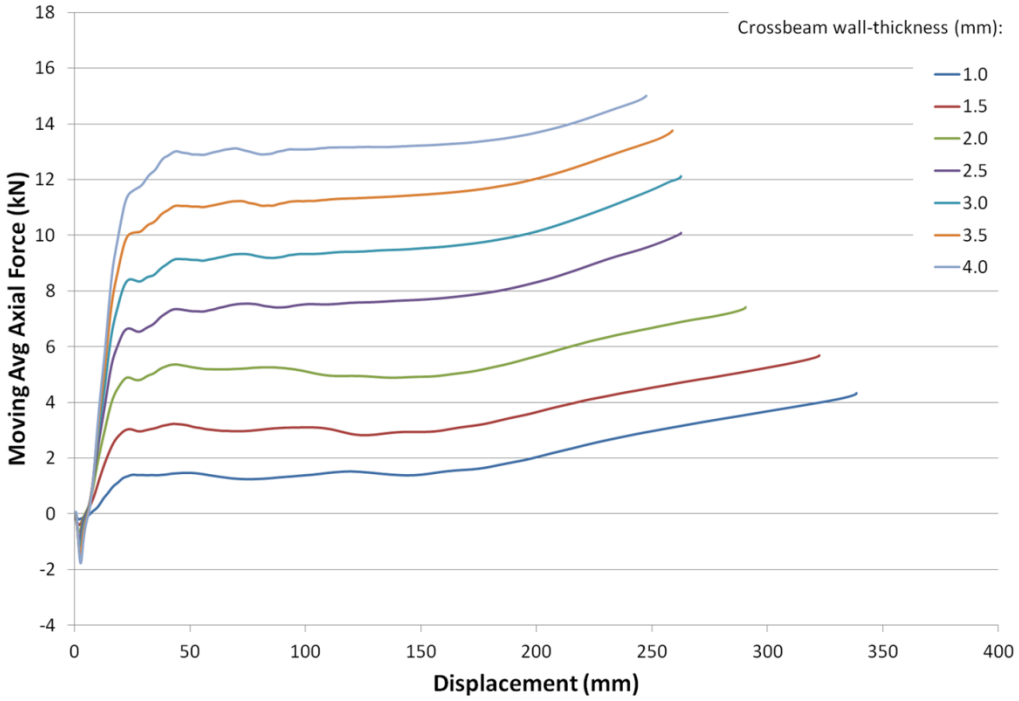

Figure 10.13: Moving average axial force-displacement graph of *CCB-TLM* simulations at non-impacted end